A Thesis Submitted for the Degree of PhD at the University of Warwick

http://go.warwick.ac.uk/wrap/51619

Density functional theory investigations of surface structure and surface stress in adsorbate layers on Cu, Pd and Ir surfaces

by

Matthew Kevin Bradley

Thesis

submitted to the University of Warwick
for the degree of

Doctor of Philosophy

Department of Physics
June 2012

Contents

List of Figures

List of Tables

Acknowledgements

First and foremost my sincerest thanks go to Prof. Phil Woodruff both for accepting my application and for guiding me through my PhD. Your ability and willingness to transmit your extensive knowledge has been incredibly beneficial to my learning and your open door attitude has transformed an intimidating figure into someone that I feel comfortable expressing my own opinions to. I can't envisage a better mentor, thankyou Phil.

I am similarly grateful for the support of Dr. Jim Robinson, not only in setting up and maintaining the group's computational resources but also on a technical level. Having you there to answer the questions I have had (however basic they may have been) has been invaluable, thankyou Jim.

I would also like to thank all of the colleagues I have had during the last three and a half years. Two of whom I would like to give special thanks to are David Duncan and Daniel Sheppard. Although I've had to put up with the incessant bellowing voice of David for three and a half years, it has been a small price to pay for his helpful attitude, our successful collaborations, and the good times we have spent together, many of which involved a cold beverage or three. Sitting opposite to Dan in the office has led to countless enlightening conversations and has meant that I have always had someone there, both to bounce ideas off and provide support.

Thanks must also go to the other people with whom I have collaborated with directly. Although I have only met Dagmar Kriekemeyer Lorenzo a few times, several publications have resulted from our collaborations, so to her I am very grateful. Additionally, a thankyou goes to Dr. Gavin Bell and Prof. Chris McConville who have provided an environment in which additional collaborative publications have resulted. In this respect, I am grateful for the inclusion of my work in a recent publication by Liam Fishwick and also for my collaborations with Chris Burrows, Ian Maskery and Jim Aldous.

Lastly, I have to thank my family, Frank, Alma and Douglas for their continued support throughout my years of education and the girl to whom I am betrothed, Shi Ying, for remaining by my side, in spite of my unorthodox working patterns.

Matthew

Declarations

This thesis is submitted to the University of Warwick in partial fulfillment of the requirements for the degree of Doctor of Philosophy. It contains an account of the work carried out by myself in the Department of Physics at Warwick University, under the supervision of Prof. D. P. Woodruff and Dr. J. Robinson, during the period from October 2008 to June 2012. No part of this thesis has been previously submitted to this or any other institution.

Several articles based on this research have been published or are in preparation:

- M. K. Bradley, J. Robinson, and D. P. Woodruff, 'The structure and bonding of furan on Pd(111)', *Surf. Sci.*, 2010, **604**, 920.
- M. K. Bradley, D. K. Lorenzo, W. Unterberger, D. Duncan, T. Lerotholi, J. Robinson, and D. P. Woodruff, 'Methoxy Species on Cu(110): Understanding the Local Structure of a Key Catalytic Reaction Intermediate', *Phys. Rev. Lett.*, 2010, **105**, 086101.
- D. C. Jackson, D. A. Duncan, W. Unterberger, T. J. Lerotholi, D. K. Lorenzo, M. K. Bradley and D. P. Woodruff, 'Structure of Cytosine on Cu(110): a Scanned-Energy Mode Photoelectron Diffraction Study', *J. Phys. Chem. C*, 2010, **114**, 15454.
- M. K. Bradley, D. A. Duncan, J. Robinson and D. P. Woodruff, 'The structure of furan reaction products on Pd(111)', *Phys. Chem. Chem. Phys.*, 2011, **13**, 7975.
- D. Kreikemeyer Lorenzo, M. K. Bradley, W. Unterberger, D. A. Duncan, T. J. Lerotholi, J. Robinson and D. P. Woodruff, 'The structure of methoxy species on Cu(110): A combined photoelectron diffraction and density functional theory determination', *Surf. Sci.*, 2011, **605**, 193.
- M. K. Bradley, D. P. Woodruff and J. Robinson, 'Surface stress changes in the Ir(001)/H system: Density functional theory study', *Phys. Rev. B*, 2011, **84**, 075438.

Parts of this work have also been presented at four national and international conferences from 2009 to 2011.

Matthew Kevin Bradley

Abstract

An introduction to surface structure and plane wave density functional theory (DFT) is presented along with theoretical studies of seven adsorbate systems.

A new energetically favourable structure of low symmetry is found for furan on Pd(111) that is entirely consistent with previous experimental findings from scanned-energy mode photoelectron diffraction (PhD). In addition, it is found that the C_3H_3 decomposition product of furan on the same surface is likely to be adsorbed in a propargyle conformation ($CH\text{-}C\text{-}CH_2$) although some cooccupation of the molecule in a half benzene conformation (CH-CH-CH) is also possible.

Methoxy is found to adsorb at local short bridge sites only on Cu(110), occupying locations both above the clean surface and above pairs of surface Cu adatoms. Simulated scanning tunneling microscope (STM) images of the (5×2) reconstruction are found to be in qualitative agreement with previous images recorded experimentally. The experimentally determined local structure of cytosine on the same surface is confirmed and models are proposed for the (6×6) reconstruction.

An increased tensile surface stress is found to be associated with the Ir(001)(1×1) → Ir(001)(5×1)-hex phase transition, thus confirming that the reconstruction is not a consequence of the large surface stress of bulk terminated Ir(001). In contrast, H adsorption on Ir(001) (5×1)-hex does lead to a reduction of the surface stress in the range 1.76-2.06 Nm^{-1} for a H coverage range 0.6-0.8 ML in excellent agreement with the experimentally-determined value of 1.7 Nm^{-1}.

The energetically favourable structure for methanethiolate adsorption on Cu(100) is found to be a c(6×2) missing row structure that allows effective relief of surface stress. On Cu(111) several complex overlayer models for methanethiolate adsorption have similar associated surface energy, suggesting that the local structure is dependent on the availability of Cu adatoms. For adsorption on both surfaces, agreement with previous STM images and MEIS results is discussed.

Abbreviations

B3LYP	Becke three-parameter Lee-Yang-Parr functional
BFGS	Broyden-Fletcher-Goldfarb-Shanno geometry optimisation
CASTEP	Cambridge Serial Total Energy Package
CLS	core level shift
DFT	density functional theory
DM	density mixing
DMDS	dimethyl disulphide
EDFT	ensemble density functional theory
fcc	face-centred cubic
GGA	generalised gradient approximation
hcp	hexagonal close-packed
HREELS	high-resolution electron energy loss spectroscopy
LDA	local density approximation
LEED	low energy electron diffraction
LEIS	low energy ion scattering
LITD	laser-induced thermal desorption
MEIS	medium energy ion scattering
ML	monolayer
NEXAFS	near edge X-ray absorption fine structure

NIXSW	normal-incidence X-ray standing waves
PAW	projector augmented wave
PBE	Perdew-Burke-Ernzerhof functional
PhD	scanned-energy mode photoelectron diffraction
PW91	Perdew-Wang 1991 functional
RPBE	revised Perdew-Burke-Ernzerhof functional
SAM	self-assembled monolayer
SCF	self-consistent field
SEXAFS	surface extended X-ray absorption fine structure
STM	scanning tunneling microscopy
SXPS	soft X-ray photoelectron spectroscopy
SXRD	surface X-ray diffraction
TPD	temperature-programmed desorption
UHV	ultra-high vacuum
UPS	ultraviolet photoelectron spectroscopy
XPD	X-ray photoelectron diffraction
XPS	X-ray photoelectron spectroscopy

Chapter 1

Introduction

1.1 Surface structure and the role of density functional theory

The surface of a material is inherently interesting since its physical properties are considerably different to those of the bulk and it is the only part of a material which may interact directly with external matter. Moreover, detailed knowledge of the structure of the surface is of paramount importance in understanding many of its chemical, as well as electronic, properties. Following the advent of quantitative surface specific structural probes around 40 years ago [1], beginning with low energy electron diffraction (LEED), surface structure has therefore grown into a field of research in its own right with a large number of scientists devoting their careers to understanding the nuances of the vast array of attainable stable surfaces.

Low-index single crystal surfaces are the simplest of all conceivable surfaces of a material due to their small periodic surface mesh and high symmetry. It is for this reason that these surfaces are often used as models to understand more complex systems. Even given this apparent simplicity however, introduction of adsorbate species significantly increases the complexity of the structure of the surface in most cases, generally increasing the size of the periodic mesh and in many cases destroying the periodicity of the surface entirely. It is this class of system, involving the interaction of a surface and external species, which is relevant to surface specific processes such as heterogeneous catalysis and is thus of great industrial, as well as scientific, interest.

Nowadays there are many available experimental methods that may be used to determine surface structure [2, 3]. While these methods have been incredibly successful in their own right, often allowing the determination of adsorbate-substrate bondlengths to within hundredths of an Ångstrom, the availability of inexpensive computing resources in recent years has allowed them to be complemented by sophisticated first principles calculations, namely density functional theory (DFT). Such calculations are now routinely carried out and are generally successful in finding the correct, experimentally determined adsorption site as the lowest energy model. Furthermore, DFT calculations provide a method to explore aspects of the surface which are not available, or are difficult to determine, experimentally. One such aspect is that of surface stress (for which there are no experimental methods capable of determining the absolute magnitude) which is known to have implications concerning surface processes such as surface reconstruction and epitaxial growth [4, 5], magnetism [5], adsorption [6] and surface alloying and segregation [7].

1.2 Thesis overview

This thesis provides an account of work conducted in the Department of Physics at the University of Warwick during the period from October 2008 to June 2012 and is arranged as follows. Chapter 2 focuses on physical attributes and processes specific to surfaces with emphasis given to those related to structure, stress and adsorption. Some useful surface specific quantities are also defined and experimental determination methods are highlighted where applicable. Chapter 3 begins with an introduction to the underlying theory of DFT and highlights the approximations made when using the theory. Following this is a discussion of the plane-wave pseudopotential methodology employed by the Cambridge Serial Total Energy Package (CASTEP) code, a common theme throughout this section being the necessity to ensure that calculations are properly converged. Finally, application of plane-wave pseudopotential calculations are discussed in the context of studies of surface structure and surface stress.

Chapters 4-7 comprise the results of several DFT investigations of surface structure and surface stress that have now been published, or are soon to be published, in the open literature. In chapter 4 a new low-energy model is discovered for furan on Pd(111) [8] and structural models are proposed and compared with experimental scanned-energy mode photoelectron diffraction (PhD) data analysis for the C_3H_3 species [9], one of the decomposition products of furan, on the same surface. Chapter 5 follows with the investigation of two long-range adsorbate structures formed on Cu(110); the DFT calculations aid the determination of the (5×2) structure formed by methoxy [10, 11] and allow structural models to be proposed for the (6×6) cytosine reconstruction, in the process providing rationale for the experimentally observed azimuthal rotation of the cytosine species [12]. In chapter 6 there is a thorough examination of both the clean, and H-dosed Ir(001) surfaces with particular attention paid to the role of surface stress in this system [13]. Chapter 7 then proceeds with results and discussion aimed at elucidating the structure of the ordered overlayers formed by the thiolate species on Cu(100) and Cu(111). In this case the results are complemented by experimental data from medium energy ion scattering (MEIS) , and simulated scanning tunneling microscopy (STM) images are compared with those of published experimental studies. Lastly, chapter 8 gives general conclusions and provides a brief look towards the future for DFT in the context of surface science.

Chapter 2

Theory of adsorbate systems and investigative methods

2.1 Physical phenomena at surfaces

Several well defined physical phenomena occur at a substrate - vacuum interface which do not occur in the bulk of a material. In particular, the influence of the vacuum typically leads to surface structural relaxations and the introduction of surface stress or, in some cases, total surface reconstruction. Additionally, the electronic structure is modified leading to the emergence of states that are confined to the surface region, which may impact significantly on the surface properties (e.g. topological insulators). In the presence of foreign species, the surface may accommodate adsorption and reaction processes (heterogeneous catalysis), the details of which are, in general, very sensitive to the composition and structure of the surface. A fundamental knowledge of basic surface phenomena is thus a necessary prerequisite for understanding adsorbate systems and predicting the behavior of the surface in the presence of external species.

2.1.1 Surface free energy

The fact that a crystal is stable is an indication that its total energy is lower than that of the sum of its constituent atoms in isolation. Formally therefore, the surface free energy, γ, defined by Gibbs [14] must be positive for a clean surface, where the reversible work, dw, needed to cleave a new surface of area dA is

$$dw = \gamma dA. \tag{2.1}$$

The surface free energy thus provides a direct measure of the stability of an exposed surface.

In the case of face-centred cubic (fcc) transition metal surfaces, which are the subject of this thesis, it has been shown using a theoretical modified embedded-atom method that the (111) (see Figure 2.1) surface is the most stable in all cases [15]. Furthermore, this study found that the surface energy increases linearly with the angle θ_{hkl} of the surface plane to the (111) plane. It should be noted however that at large angles, $\sim \theta_{hkl} \geq 40\,^{\circ}$, this approximation breaks down such that for some fcc transition metals the surface energy of the (001) surface ($\theta_{001} = 54.7\,^{\circ}$) is lower than the that of the (110) surface ($\theta_{110} = 35.3\,^{\circ}$). Qualitatively, this effect can be attributed to the greater atomic roughness, and corresponding larger surface area, found in the outermost layer of the (110) surface compared to the (001) surface (see Figure 2.1).

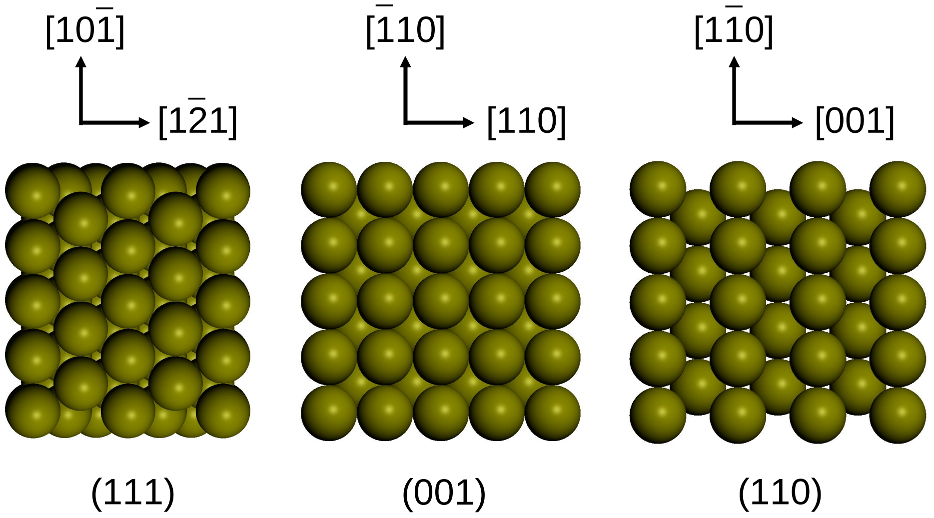

Figure 2.1: Low index surfaces of the fcc lattice. Surface layer atomic density decreases from left to right. Note that two inequivalent hollow sites exist on the (111) surface, the face-centred cubic (directly above third layer substrate atoms - fcc) and hexagonal close-packed (directly above second layer substrate atoms - hcp) site.

Several measurement techniques have been devised to determine the surface energy of liquids, and these have been used successfully to measure the surface energy of liquid metals. Techniques include the sessile drop method [16], the pendant drop method [17], the drop weight method [17] and Lenard's wire frame method [18]. Of course, for most metals these methods require that the measurement is taken far above room temperature. Just below the melting point, where the crystal maintains a constant volume under uniaxial tension, the method of zero creep can be used [19]. In this case, multiple thin wires are loaded with incremented weights and their length change upon heating is measured. The mass, m, which leads to zero strain at high temperature is used to determine the surface energy,

$$\gamma = \frac{mg}{\pi r}, \tag{2.2}$$

where g is the acceleration due to gravity and r is the radius of the wire.

The only measurements of surface energy on solids at low temperature have come from cleavage experiments [20]. In this case a force is applied to a pre split sample and the length of the resulting crack is related to the surface energy by

$$\gamma = \frac{6F^2L^2}{Ew^2t^3} \tag{2.3}$$

where F is the force applied, L is the length of the resulting crack, E is the Young's modulus for the appropriate orientation and the beam width and thickness are given by w and t respectively.

The same quantity is also routinely extracted from DFT calculations for the ground state, even for relatively complex crystals (see section 3.3.2).

2.1.2 Surface relaxation

The potential experienced by atoms in the surface region of a material is different to that experienced by atoms in the bulk due to the different local environment. This will, in general, induce changes in the atomic structure of the surface region which act to reduce the surface free energy (equation 2.1) of the system.

In the case of a simple transition metal surface, spilling of the valence electronic charge into the vacuum typically accompanies an inward relaxation of the outermost atomic layer, towards greater charge density. This inward relaxation is generally larger for the more open-packed surfaces of a metal where the potential energy profile parallel to the surface is more strongly corrugated and Smoluchowski smoothing [21], an effect responsible for charge shift towards interatomic surface layer regions upon cleavage, is greatest. In contrast, lower layers of the surface may experience either inward or outward relaxations depending on the surface in question and the sign of the relaxation is often found to alternate with consecutive layers while gradually being damped out. A typical example is that of Al(110) where LEED measurements have determined surface relaxations of -8.6 %, +5.0 % and -1.6 % for the first three atomic layers [22]. This effect has been linked with oscillations that occur in the electron charge density in the near surface region (Friedel oscillations [23]) [1]. However, theoretical calculations which do not include this effect have been found to reproduce the observed alternating-sign relaxations [24].

While a description based on the spilling of valence charge into the vacuum is appropriate for the surfaces of metals, surface relaxations found in semiconducting materials vary to a greater degree; in general, these surfaces relax in such a way as to reduce the number of dangling bonds arising from surface layer atoms lacking some of the bonding partners of bulk atoms [25]. For instance, one surface layer atom may exhibit an inward relaxation and donate its unpaired electron to another atom which consequently relaxes outwards. Such behavior is typical for the (110) surface of many III-V semiconductors, e.g. GaP [26], where the (1×1) surface periodicity is conserved.

2.1.3 Molecular adsorption

A continuum of adsorption sites exists at a surface and a species may, in principle, be adsorbed at any location. However, many molecules are preferentially adsorbed at or near to high symmetry sites on the surface, and particularly so if the adsorbate has symmetry commensurate with the substrate. It is for this reason, along with its industrial prevalence (particularly in chemical manufacturing [27]), that CO has been the most studied molecular adsorbate and is often used as a model system to trial new techniques, both theoretical and experimental.

The strength of a bound state created by adsorption of a foreign species may be quantified by the adsorption energy, E_a, which is defined as the amount of work per adsorbate that must be done in order to remove the species from the surface to infinity. For simple metals, the strength of adsorption for a given molecule is typically greater on the more open packed surfaces such that the hierarchy of the strength of adsorption on low index fcc transition metals surfaces (see Figure 2.1) is generally (110) > (001) > (111). Even on a particular crystallographic face of a material, however, the most stable adsorption site (with the greatest adsorption energy) may be influenced by many factors including adsorbate coverage and the presence of co-adsorbates, both of which are pressure and temperature dependent. Furthermore, multiple adsorption sites may exist which have similar associated adsorption energies, leading to possible co-occupation of sites, or the potential energy profile may be such that energy barriers from one adsorption site to another are small with respect to the kinetic energy of the adsorbed species, thus allowing them to ‘hop’ rapidly between sites or even move freely over the surface. In either case, experimental determination of the preferred adsorption site(s) using current techniques becomes challenging. If a species does adsorb at well defined locations, long-range well-ordered structural phases may be formed which can be detected by well-established experimental techniques (e.g. LEED). It is these well-ordered phases that have been most extensively studied, in part because many of the available surface structure probes require that the surface has long-range order (see section 2.2).

2.1.4 Surface stress

Unlike the energy-lowering relaxations of atoms in the direction perpendicular to the surface, which allow the perpendicular stress component of a crystal to reduce to zero, the lateral atomic periodicity is constrained by the underlying bulk crystal. Therefore, atoms at a clean unreconstructed metal surface cannot relax towards each other and the surface is necessarily under tensile (positive) stress. Such surface stress is related to the surface free energy by the Shuttleworth equation [28]

$$\sigma_{ij} = \frac{1}{A}\frac{dA\gamma}{d\epsilon_{ij}} = \gamma\delta_{ij} + \frac{\partial\gamma}{\partial\epsilon_{ij}} \tag{2.4}$$

where δ_{ij} is the Kronecker delta, ϵ_{ij} is an elastic strain tensor element and the surface stress component, σ_{ij}, is a second rank tensor element that relates the work associated with the variation in γA, the total excess free energy of the surface, to the applied strain $d\epsilon_{ij}$.

For transition metals, DFT calculations have determined that the hierarchy of surface stress magnitude for the low-index surfaces varies from case to case and is strongly dependent on the surface relaxation [29]; the reduced sp electron density found in the surface layer relative to the bulk is reversed with increasing inward relaxation of the outermost atomic layer such that the surface becomes more bulk-like and surface stress reduces.

Adsorption causes modification of the structure of the underlying substrate, which may penetrate several atomic layers. While such modification is typically rather small and often ignored in experimental structure determination studies, it may significantly influence the surface stress (e.g. adsorption of H on Ir(001)-AR investigated in chapter 6). In simple cases, surface stress changes due to atomic adsorption at low coverage, where the surface stress changes linearly with coverage [30], can usually be qualitatively explained by the relative electronegativity of the adsorbing species and the substrate on which adsorption is taking place; electronegative {electropositive} adsorbates lead to a reduction {increase} of the valence charge in the region between surface layer atoms resulting in a reduction {increase} of the surface stress [31]. In the case of H (electropositive) and O (electronegative) on Pt(111) however, adsorption of either species has been found to reduce the surface stress showing that even atomic adsorbates do not always follow this trend [32]. At higher coverage, inter-adsorbate interactions become significant and surface stress changes are strongly dependent on the exact nature of these interactions.

In contrast to the case of surface relaxations, there is no experimental method currently available that can be used to determine the absolute surface stress of a single-crystal surface. There are some reported measurements of the change in surface stress associated with a surface reconstruction however, particularly for adsorbate-induced reconstructions. These experiments exploit the slight bending of a thin crystal beam that occurs when the surface stresses on the two opposite faces are different. A variety of methods have been used to measure such changes in the crystal curvature associated with adsorption, which must be on one face of the crystal only (e.g. [33]). The limited amount of experimental data of this kind has been supplemented by theoretical calculations, with early examples of results for clean metal surfaces and adsorption upon them being reported by Needs and Mansfield [34] and by Feibelman [35]; a review of most of this earlier work was been provided by Haiss [36].

2.1.5 Surface reconstruction

In addition to surface relaxation, the exposure of a cleaved crystal surface may cause a substantial reconstruction of the surface region to occur if the surface free energy (equation 2.1) can be lowered by the reconstruction. In the majority of cases however, there is an activation barrier to such reconstruction and the reconstruction will, therefore, only occur above a well-defined transition temperature. While such reconstruction is commonplace among semiconducting surfaces, a particularly famous example of which is the complex (7×7) reconstruction of

Si(111) [37], and can usually be explained qualitatively by the tendency to reduce the number of dangling bonds exposed by the cleavage [25], clean surface reconstructions are comparatively rare for transition metals. Notable exceptions occur in the (001) and (110) surfaces of the 5d transition metals of Ir, Pt and Au; the (001) surface reconstructs to form a one-layer quasi-hexagonal overlayer structure incorporating a 20% increase in atomic density of the surface layer [38–40] while the (110) surface reconstructs to form a 'missing row' structure whereby every other row of atoms is removed, thus exposing narrow pseudo (111) faces [41]. The preference of the (001) surfaces of the 5d transition metals to reconstruct was originally thought to be a consequence of the particularly large surface stress of the clean surface which arises as a result of strong relativistic effects. However, recent DFT calculations have reported that the surface stress is actually *increased* by the reconstruction (see chapter 6) [13].

Rather than preferentially coordinating directly to an existing surface, adsorption may instead instigate a surface reconstruction. Examples of structures resulting from this process include the (5×2) overlayer formed by methoxy on Cu(110) (see section 5.1) and the pseudo-square overlayer formed by methanethiolate on Cu(111) (see section 7.4), both of which are discussed in detail in subsequent chapters.

2.2 Structure determination

Although this thesis comprises primarily the results and analysis of theoretical simulations of surfaces, it is of paramount importance that such studies are compared with experiment where possible. Indeed in many cases, and particularly so as ever more complex surface structures are investigated, it is the combined results from experimental and theoretical investigative methods that are used to provide the necessary information to conclusively determine the precise structure of a surface. While DFT has emerged as the preferred theoretical tool for surface structure investigations, a relatively large number of experimental surface structure probes are widely used, but may be classified by two broad categories:

1. Methods that rely on the wave interference of electrons or photons: These include methods that provide useful information only if the surface exhibits long range order, such as LEED (which has yielded the most structural solutions for any technique [42]) and surface X-ray diffraction (SXRD), as well as those such

as scanned-energy mode photoelectron diffraction (PhD) [43, 44] and near edge X-ray absorption fine structure (NEXAFS) [45] which require local order only.

2. Methods based on the scattering of ions: Typically H^+ or He^+ ions are used for the techniques of low (LEIS) or medium (MEIS) energy ion scattering where the deBroglie wavelength of these ions is much smaller than interatomic distances. In this case, multiple scattering simulations based on classical two-body elastic collisions suffices to elucidate surface structure.

While such investigative methods provide direct structural information, the primarily composition-determination tool of X-ray photoelectron spectroscopy (XPS) also deserves attention since comparison of core level shifts (CLS) arising from different local atomic environments can, in some circumstances, provide useful structural information (see section 3.3.4). In addition, imaging tools, and particularly STM, which utilises electrons quantum tunneling from the sample to a conducting tip, provide valuable insight into surface processes and can often aid structure determination. Comprehensive reviews of modern techniques of surface science can be found in the publications by Woodruff and Delchar [3] and Vickerman and Gilmore [2].

It is important to note that most of the available surface structure techniques struggle to allow the collection of meaningful data much above ultra-high vacuum (UHV) pressures ($\sim 10^{-9}$ mbar) such that most surface structure experiments are conducted in the confines of a UHV chamber; at higher pressures the mean free path of the probing particles traversing the path from the surface to the detector becomes prohibitively small. Some X-ray techniques (SXRD and SEXAFS) can be used at higher pressure but require special apparatus in order to provide structural information [46]. In addition, low temperature conditions are often preferable for taking measurements since atomic vibrations, and in many cases adsorbate site hopping, can be greatly reduced. Therefore, in cases where a high temperature reconstruction is to be observed, the system is first heated to the activation temperature of the reconstruction and subsequently cooled so that the structure of the reconstruction is ‘frozen in’ in preparation for measurement.

Chapter 3

Density functional theory: Formal theory and application

3.1 Fundamental theory

In principle the Schrödinger equation, $\hat{H}\Psi = E\Psi$, where $\hat{H}$ is the Hamiltonian operator which acts on the total wavefunction Ψ, and E is the total energy of the system, provides a precise quantum-mechanical description of the physical behavior of the universe. In the case of N electrons interacting with static nuclei, $\Psi = \Psi\left(\mathbf{r}_1, \mathbf{r}_2, ..., \mathbf{r}_N\right)$, following the Born-Oppenheimer approximation [47], the time-independent Hamiltonian neglecting electron spin may be expressed

$$\hat{H} = -\frac{\hbar^2}{2m}\sum_{i=1}^{N}\nabla_i^2 + \sum_{i=1}^{N} V\left(\mathbf{r}_i\right) + \sum_{i=1}^{N}\sum_{j<i} U\left(\mathbf{r}_i, \mathbf{r}_j\right) \tag{3.1}$$

where the three terms define the kinetic energy the electrons, the interaction of the electrons with the nuclei and the electron-electron interactions respectively. Prohibitive computational demand arises, however, when trying to solve the Schrӧdinger Eequation for a multi-electron system since the electron-electron interaction term of the Hamiltonian is inherently 3N-dimensional.

In the light of the difficulties posed in finding solutions to the Schrödinger Equation, DFT provides an alternative, computationally feasible *ab initio* approach to calculating material properties which are, for systems of physical interest in most fields, far too computationally demanding to calculate by directly solving the Schrödinger Equation and are, in many cases, very difficult or impossible to determine experimentally. As a result of the rapid increase of widely available computing resources over the past 30 years, along with a myriad of refinements of, and additions to the implementation of the theory both to reduce computation time and to solve a wider spectrum of problems, DFT has emerged as a prominent tool for calculating properties of interest of collections of atoms. This has resulted in the application of DFT in an ever-expanding range of fields including heterogeneous catalysis, optics, electronics, medical physics and plasma physics and has been used to improve understanding of the physical properties of nanotubes, quantum dots, artificial molecules and superconductors but to name a few.

The importance of DFT in the scientific community has been such that Walter Kohn was awarded, with John Pople, the Nobel Prize in Chemistry in 1998 “for his development of the density-functional theory”. A further demonstration of the widespread influence of DFT can be seen with the impact of the seminal journal articles by Walter Kohn and Lu Jeu Sham [48] and by Pierre Hohenberg and Walter Kohn [49] which, as of 2003, were comfortably the two Physical Review publications with the most internal citations in the journal’s 110 year history [50].

3.1.1 Hohenberg-Kohn Theorem

The underlying theory of DFT was published in 1964 by Pierre Hohenberg and Walter Kohn [49] and comprises two simple postulates:

1. *The ground-state energy, E_0, from Schrödinger’s equation is a unique functional of the electron density.*

2. *The electron density that minimises the energy of the overall functional is the true electron density corresponding to the full solution of the Schrödinger equation: $E_0\left[n\right] \leq E[n]$.*

While the exact form of this electron density functional is not known, by using an approximation to it, the Hohenberg-Kohn postulates nevertheless provide a method to recast the 3N-dimensional Schrödinger equation to a much simpler equation which depends on just 3 spatial variables and may therefore be used to reliably calculate ground state material properties that would otherwise be unobtainable.

In addition to being used to accurately calculate a wide range of ground state properties, DFT methods have also been extended to predict excited state properties. This extension is not on the same rigorous footing, however, and calculation of such properties is therefore less reliable [51].

3.1.2 Kohn-Sham approximations

The total energy density functional $E\left[n\right]$ introduced in section 3.1.1 may be split into a summation of terms analogously to Schrödinger's equation:

$$E\left[n\right] = T\left[n\right] + V_{ext}\left[n\right] + V_{ee}\left[n\right] \tag{3.2}$$

where $T\left[n\right]$ is the kinetic energy of the electrons, $V_{ext}\left[n\right]$ is the interaction with the external potential and $V_{ee}\left[n\right]$ is the electron-electron interaction. For a system of interacting atoms, $V_{ext}\left[n\right]$ is simply the Coulomb interaction between the atomic nuclei and the electrons:

$$V_{ext}\left[n\left(\mathbf{r}\right)\right] = \int \left\{\sum_{i=1}^{N} v\left(\mathbf{r}_i\right)\right\} n\left(\mathbf{r}\right) d\mathbf{r} \tag{3.3}$$

with the external potential

$$v\left(\mathbf{r}_i\right) = \sum_{\alpha} \frac{Z_\alpha}{\left|\mathbf{r}_i - \mathbf{R}_\alpha\right|} \tag{3.4}$$

where the summation runs over all ion cores, α, and Z_α is the charge on the ion core at $\mathbf{R}_\alpha$.

A classical approximation to $V_{ee}\left[n\right]$ can be obtained from the Hartree energy of the system:

$$V_H\left[n\left(\mathbf{r}\right)\right] = \frac{1}{2}\int \frac{n\left(\mathbf{r}\right) n\left(\mathbf{r}'\right)}{\left|\mathbf{r} - \mathbf{r}'\right|} d\mathbf{r} d\mathbf{r}'. \tag{3.5}$$

Furthermore, an approximation for $T\left[n\right]$ can be found by considering the kinetic energy of a non-interacting system of electrons which reproduce the true ground state density. The N electrons are then described by a single determinant wavefunction in N orbitals [49],

$$\Psi = \frac{1}{\sqrt{N!}} \det\left[\psi_1 \psi_2 ... \psi_N\right] \tag{3.6}$$

with density

$$n\left(\mathbf{r}\right) = \sum_{i=1}^{N} \left|\psi_i\left(\mathbf{r}\right)\right|^2 \tag{3.7}$$

where ψ_i are the N lowest energy eigenstates of the one-electron Hamiltonian

$\hat{h}$:

$$\hat{h}\psi_i = \left[-\frac{1}{2}\nabla^2 + v_{eff}\left(\mathbf{r}\right)\right]\psi_i = \epsilon_i\psi_i \tag{3.8}$$

and the Kohn-Sham effective potential $v_{eff}\left(\mathbf{r}\right)$ is given by

$$v_{eff}\left(\mathbf{r}\right) = \frac{\delta E\left[n\right]}{\delta n\left(\mathbf{r}\right)}. \tag{3.9}$$

This simplified system has the kinetic energy

$$T_s\left[\left(\psi_i\right)\right] = -\frac{1}{2}\sum_{i=1}^{N}\int \psi_i^*\nabla^2\psi_i d\mathbf{r}. \tag{3.10}$$

Hence, an approximation to the kinetic energy may be computed using a manageable finite number of terms N and the total energy density functional (equation 3.2) can be re-written

$$E\left[n\right] = T_s\left[\left(\psi_i\right)\right] + V_{ext}\left[n\left(\mathbf{r}\right)\right] + V_H\left[n\left(\mathbf{r}\right)\right] + E_{xc}\left[n\right] \tag{3.11}$$

where the exchange-correlation energy $E_{xc}\left[n\right]$ is defined as the difference between the true energy functional and the energy functional of the known components. This essentially comprises the energy contributions arising from the effects of electron exchange and correlation, which must be approximated (see section 3.1.4). Inserting equation 3.11 into equation 3.9 and differentiating gives

$$v_{eff}\left(\mathbf{r}\right) = -\sum_{\alpha}\frac{Z_\alpha}{\left|\mathbf{r}_i - \mathbf{R}_\alpha\right|} + \int \frac{n\left(\mathbf{r}'\right)}{\left|\mathbf{r}_i - \mathbf{r}'_\alpha\right|}d\mathbf{r} + \frac{\delta E_{xc}\left[n\right]}{\delta n\left(\mathbf{r}\right)} \tag{3.12}$$

where all terms are exact apart from the unknown functional E_{xc}.

3.1.3 Solving the Kohn-Sham equations

Since the effective potential v_{eff} used to construct the single-electron Hamiltonian $\hat{h}$ depends on the electron density $n(\mathbf{r})$ (see equation 3.12), which in turn depends on the eigenfunctions of the Kohn-Sham equations ψ_i (see equation 3.7), the Kohn-Sham equations (equation 3.8) must be solved self-consistently using an iterative 'self-consistent field' (SCF) procedure.

During each SCF cycle, for each point in k-space it is possible to construct and directly diagonalise a square Hamiltonian matrix in order to find the full set of Kohn-Sham eigenstates and eigenvalues, and thus calculate the ground state energy for a given Hamiltonian. However, diagonalisation scales with the cube of the matrix size and the number of elements in such a matrix is equal to the square of the number of basis functions used to describe the wavefunctions. Since calculations quickly become prohibitively expensive and, for a converged basis set consisting of 10000-100000 functions such as is typical for a plane wave basis-set (see section 3.2.2) fewer than 1% of the eigenvalues are typically occupied, it is preferable to resort to iterative optimisation methods, in which it is only the occupied eigenstates that need be included in the calculations. These calculations rely on carefully choosing search directions using algorithms such as steepest descent and conjugate gradients, and scale quadratically with the number of bands. A comprehensive review of iterative methods for *ab initio* calculations can be found in the publication by Payne, Teter, Allan, Arias and Joannopoulos [52].

There are two commonly employed classes of algorithm used to solve the Kohn-Sham equations:

1. Ensemble DFT (EDFT) [53]: The density is updated whenever the wavefunctions or occupancies are changed and the change is only accepted if the total energy is lowered by it. Thus the method is fully variational and hence very robust, although it is also rather slow since each density reconstruction requires a Fourier transform into real space.

2. Density mixing (DM) [54]: The density is reconstructed only once per SCF cycle and is thus non-variational. Under this regime, SCF cycles using the exact density found in the previous iteration, using equation 3.7, tend to overshoot the true minimum energy location causing an effect known as ‘charge sloshing’. Thus, the new density must be mixed with the density found in previous SCF cycles. Such mixing is typically performed using the algorithms of Pulay [55] or Broyden [56] which may be tuned for efficiency and are substantially more robust than linearly mixing with the density found in the previous iteration.

In most cases, a carefully selected DM algorithm is chosen in order to converge to the ground state as efficiently as possible. However, for large unit cells charge sloshing can become more problematic. Furthermore, metallic systems raise additional issues since it is not easy to identify the lowest energy eigenstates; it is possible that, upon replacing occupation of a band with that of a lower energy band near the Fermi level, the density will be altered in such a way as to restore the original ordering, and hence occupation, of the bands. Therefore, when using

DM for metallic systems, it is necessary to apply a density smearing scheme (e.g. Gaussian, Fermi-Dirac, Methfessel-Paxton [57]) to the Fermi surface such that it is smeared over a finite energy width; such treatment provides a smooth continuous transition between occupation of an orbital when its energy is changed relative to other orbitals. This can be equated to introducing a finite temperature in the system (exactly in the case of Fermi-Dirac smearing) and the total energy is increased accordingly, leading to non-zero occupation of several bands lying above the Fermi energy, thus necessitating the inclusion of more electronic bands in the calculation. At the same time however, introducing a finite smearing to the Fermi surface means that the solutions of the Kohn-Sham equations are no longer the ground state. Indeed, to first order, the value of the free energy, $E - TS$, where T is temperature and S is entropy, is reduced by the same amount. Thus the ground state energy may be recovered:

$$E_0 = E - 0.5TS. \tag{3.13}$$

Since this calculation of the entropical contribution is not exact, however, there is a trade off between the simpler convergence of using a large degree of density smearing and the possible source of error this introduces in the calculated total energy.

Independent of the algorithms used to determine the ground state, the iterative process is ceased when either the total energy change or maximum ionic force change found for consecutive iterations drops below a specified tolerance. Ionic forces are found for each structural parameter x_j of the entire structure, $\mathbf{x}$, using the Hellmann-Feynman theorem [58, 59]:

$$F_{x_j} = \frac{\partial E}{\partial x_j} = \int \psi^* \left(\mathbf{x}\right) \frac{\partial \hat{H}_{\mathbf{x}}}{\partial x_j} \psi \left(\mathbf{x}\right) d\mathbf{r} \tag{3.14}$$

where $j = 1, 2, ..., n$. These may then be atomically resolved to find the total force, F, acting on each ion.

3.1.4 Exchange-correlation functionals

A large number of approximations to the exchange-correlation energy functional have been devised with the aim of accurately representing the true functional. The first and simplest class of these is the local density approximation (LDA), $E_{xc}^{LDA} = E_{xc}^{LDA}\left[n\right]$, which allows for a formulation based upon that found for a homogeneous electron gas (jellium). The exchange contribution to the energy is known exactly for jellium [60]:

$$E_x^{LDA}[n] = \int n(\mathbf{r})\,\epsilon_x^{LDA}(\mathbf{r})\,d\mathbf{r} = -\frac{3}{4}\left(\frac{3}{\pi}\right)^{\frac{1}{3}}\int n(\mathbf{r})^{\frac{4}{3}}d\mathbf{r} \tag{3.15}$$

where the exchange-correlation energy functional has been decomposed into exchange and correlation components such that $E_{xc} = E_x + E_c$ and ϵ_x is the exchange energy density. The true analytical expression for the correlation energy functional is only known for the high [61] and low [62] density limits of jellium. However, quantum Monte Carlo simulations have provided accurate values for the correlation energy for a range of intermediate densities [63]. Thus, a number of parameterisations of E_c^{LDA} have been devised which interpolate from these values while maintaining the correct asymptotic behavior (e.g. Vosko-Wilk-Nusair [64] and Perdew-Zunger [65]).

Although any real system involving atomic nuclei clearly has a very different electron density profile to that of jellium, LDA calculations often yield remarkably good agreement with experiment for many observable parameters, and particularly for those relating to simple metals and well-behaved covalent systems [66]. It has long been understood, however, that such calculations systematically overestimate molecular bond energies and the cohesive energy of solids [67].

A higher level approximation to $E_{xc}[n]$ can be made by also considering the local gradient of the electron density. Functionals that adopt this approach are classified as generalised gradient approximation (GGA) functionals: $E_{xc}^{GGA} = E_{xc}^{GGA}\left[n, \vec{\nabla}n\right]$. Since there are many ways in which the gradient of the electron density may be incorporated into a formulation of $E_{xc}^{GGA}\left[n, \vec{\nabla}n\right]$, a large number of functionals have been devised, some of which are fully *ab initio* while others are highly parameterised using large data sets. Ultimately however, the usefulness of a particular functional is gauged by the accuracy of results obtained using it and its transferability to a wide range of problems. In this respect, two of the most commonly used GGA functionals are the Perdew-Wang 1991 (PW91) [68] and Perdew-Burke-Ernzerhof (PBE) [69] functionals, the articles introducing both are to be found in the top 10 cited physics publications since 1898 according to the online journal citation database, Institute of Scientific Information (ISI) Web of Knowledge [70].

These particular GGA functionals have the form

$$E_x^{GGA}[n] = \int n(\mathbf{r})\,\epsilon_x^{LDA}(n(\mathbf{r}))F_x(s(\mathbf{r}))\,d\mathbf{r} \tag{3.16}$$

and differ only in the choice of local exchange enhancement factor F_x. The PBE exchange functional enhancement factor has a much simpler form than that of the PW91 functional and can be expressed

$$F_x^{PBE}(s) = 1 + \kappa - \frac{\kappa}{1 + \mu s^2/\kappa} \tag{3.17}$$

where $s(\mathbf{r})$ is the reduced density gradient,

$$s(\mathbf{r}) = \frac{|\nabla n(\mathbf{r})|}{2\left(3\pi^2\right)^{\frac{1}{3}} n(\mathbf{r})^{\frac{4}{3}}}, \tag{3.18}$$

μ and κ are constants and $\kappa = 0.804$ is chosen such that the Lieb-Oxford bound [71]

$$E_x(n) \geq E_{xc}(n) \geq -1.679 \int n(\mathbf{r})^{\frac{4}{3}}\, d\mathbf{r}, \tag{3.19}$$

a universal property of the Coulomb interaction, is automatically satisfied.

In addition to these, revised versions of the PBE functional have become popular more recently since authors claim that they provide a systematic improvement to atomisation energies and chemisorption energies. These include E_{xc}^{revPBE} [72], which is identical to the PBE functional apart from a change to $\kappa = 1.245$ and E_{xc}^{RPBE} [73] which incorporates the improved features of the revPBE functional in a modified PBE functional where

$$F_x^{RPBE}(s) = 1 + \kappa\left(1 - e^{1-\mu s^2/\kappa}\right) \tag{3.20}$$

with $\kappa = 0.804$, thus still satisfying the Lieb-Oxford bound.

Further refinement to the functional may be made by incorporating terms which include second derivatives of the electron density gradient or by using the exact exchange energy, the non-local nature of which increases computational requirements substantially, and particularly so for calculations involving non-local basis sets such as those used in the plane-wave pseudopotential method [51] (see section 3.2). Functionals following such prescriptions are known as meta-GGA and hyper-GGA functionals respectively. Much research continues in this area, particularly in developing screened hyper-GGA functionals in which the exact exchange is only incorporated in a short-range component of the exchange interaction [51].

Other methods include LDA+U [74], in which a term is added to the LDA functional to account for the absence of the orbital dependency of the Coulomb and exchange interaction, and DFT-D [75] which includes an empirical correction for the lack of a description of van der Waals forces within standard DFT methods.

Selecting a functional for a particular study is a difficult task since there are so many available. However, for chemisorption of atoms and molecules on transition metal substrates, the revised Perdew-Burke-Ernzerhof (RPBE) functional has proved to be particularly successful at obtaining accurate energetics [73], albeit with bondlengths typically overestimated by ∼1-2 % [76]. This exchange-correlation functional has thus been the preferred choice for the majority of the work presented in this thesis and is the one which has been used for all calculations in subsequent chapters unless stated otherwise.

Table 3.1 shows the resulting chemisorption bondlengths, using a variety of exchange-correlation functionals, for a deprotonated glycine molecule (glycinate - NH_2CH_2COO) adsorbed on Cu(111) in a stable tridentate conformation with the N and both O atoms coordinated to the surface. As is typically the case, the variation in reaction energy, E_a^*, (defined in the table) and bondlengths clearly illustrate the overbinding tendency of the LDA relative to the GGA functionals, with E^{RPBE} being the least strongly binding. In fact, the negative number reported for E_a^* using the RPBE functional indicates that there is an energetic preference for glycine to be dissociated from the surface rather than being adsorbed as deprotonated glycine in this adsorption site with gaseous H_2. In this case, the inclusion of DFT-D to the PW91 calculation increases the reaction energy but has little effect on the bondlengths. While this increased reaction energy is to be expected for DFT-D calculations, the sensitivity of the structure to this inclusion is highly system dependent. Table 3.2, which shows calculated lattice parameters of the bulk fcc transition metals relevant to the DFT investigations presented in this thesis, demonstrates the similar functional dependence of the bulk lattice parameter, RPBE being the most weakly, and LDA the most strongly, binding. In any case, a surface structure found using a DFT calculation may be, and often is in practice, scaled to the experimental bulk lattice parameter prior to comparing with the results of an experimental surface structure determination.

Regardless of the choice of functional, there is no reliable method of quantifying errors within DFT and only through experience and careful analysis of the trends of results obtained using the various functionals has it been possible to gain insight into how closely one expects a calculated parameter to be to that measured in experiment. In this regard however, a relatively new method which utilises Bayesian statistics [79] is claimed to be capable of producing realistic error estimates from an ensemble of results obtained using a variety of exchange-

Table 3.1: Chemisorption bondlengths of deprotonated glycine on Cu(111) adsorbed in a stable tridentate conformation with the N atom adsorbed in an atop location and the two O atoms atop (O_a) and off-atop (O_{oa}) respectively. The reaction energy, E_a^*, is defined as the energy difference between the sum of the energy of the surface with adsorbed deprotonated glycine with half of a gas phase H_2 molecule and the sum of the energy of the clean surface with a gas phase glycine molecule. A greater value for E_{reac} indicates a more stable adsorption structure.

E_{xc}	E_{reac} (meV)	O_a-Cu (Å)	O_{oa}-Cu (Å)	N-Cu (Å)
LDA	838	2.11	2.05	2.10
PW91	267	2.19	2.10	2.19
PW91+DFT-D	914	2.19	2.13	2.17
RPBE	-205	2.23	2.14	2.28

Table 3.2: A selection of DFT calculated bulk lattice parameters for the three fcc metals relevant to the investigations discussed in later chapters, using a variety of common functionals.

Material	LDA (Å)	PW91 (Å)	PBE (Å)	RPBE (Å)	Experiment (Å)
Pd	3.842	3.909	-	3.922	3.8822 ± 0.0010 (77 K) [77]
Cu	3.519	3.630	3.626	3.654	3.6146 (298 K) [78]
Ir	-	-	-	3.906	3.8392 (298 K) [78]

correlation functionals. So far though, the method has not been widely adopted by the scientific community.

3.2 Plane-wave pseudopotential method

The plane-wave pseudopotential method is particularly well suited to studies of surface structure; expansion of wave functions in terms of plane waves (section 3.2.2) lends itself nicely to the periodic nature of a surface and the use of pseudopotentials (section 3.2.4) allows a radical reduction of the computational burden of calculations while still maintaining good energetic and structural accuracy. The method is therefore a common choice for surface investigations and is implemented in many DFT codes.

3.2.1 Introduction to CASTEP

The Cambridge Serial Total Energy Package (CASTEP) [80], written in FORTRAN90, is a DFT package created by Prof M. C. Payne, a member of the Theory of Condensed Matter (TCM) group at the Cavendish Laboratory, Cambridge which has subsequently been developed by members of the TCM group and others around the UK. The code is capable of performing parallelised DFT calculations using the plane-wave pseudopotential method that scale with the cube of the number of atoms in the asyptotic limit. The code also contains several modules designed to allow calculation of a wide range of properties of collections of atoms. As a result, CASTEP has been used successfully for a large number of studies, involving a myriad of systems in an ever-expanding range of scientific disciplines.

The CASTEP calculations that have provided the results presented in this thesis have been conducted on several high-performance computing clusters at the University of Warwick in both the Surface, Interface and Thin Film Group and the Centre for Scientific Computing. Many of the results have been analysed using either Accelrys Materials Studio [81] or X-window Crystalline Structures and Densities (Xcrysden) [82], both of which provide a wide range of visualisation and, in the case of Materials Studio, analysis tools.

3.2.2 Basis sets

As alluded to in section 3.1.3, in order to solve the Kohn-Sham equations the single-electron wavefunctions must be expressed numerically using a convenient basis set. In this respect, two classes of functions can be used. Functions which are localised in space, e.g. Bessel functions, can accurately represent electronic wavefunctions using a relatively small basis set. As such, many DFT codes incorporate these, and particularly those which are primarily concerned with calculations involving free molecules, where the total wavefunction is itself localised. In contrast, for the study of periodic systems one can utilise Bloch's theorem:

$$\phi_{\mathbf{k}}\left(\mathbf{r}\right) = e^{i\mathbf{k}\cdot\mathbf{r}} u_{\mathbf{k}}\left(\mathbf{r}\right) \tag{3.21}$$

which provides the form of solutions to Schrödinger's equation for a periodic structure. The periodic function $u_{\mathbf{k}}\left(\mathbf{r}\right)$ may then be conveniently expanded in terms of plane waves of varying frequency:

$$u_{\mathbf{k}}\left(\mathbf{r}\right) = \sum_{\mathbf{G}} c_{\mathbf{G}} e^{i\mathbf{G}\cdot\mathbf{r}} \tag{3.22}$$

where the sum is taken over all $\mathbf{G}{=}m_1\mathbf{b}_1{+}m_2\mathbf{b}_2{+}m_3\mathbf{b}_3$ for integer values of m_i, where $\mathbf{b}_i$ are the reciprocal lattice vectors of the unit cell and $\mathrm{c}_{\mathbf{G}}$ are the expansion coefficients.

Combining equations 3.21 and 3.22 gives

$$\phi_{\mathbf{k}}\left(\mathbf{r}\right) = \sum_{\mathbf{G}} c_{\mathbf{k}+\mathbf{G}} e^{i(\mathbf{k}+\mathbf{G})\mathbf{r}} \tag{3.23}$$

which are solutions to Schrödinger's equation with kinetic energy

$$E = \frac{\hbar^2}{2m}\left|\mathbf{k}+\mathbf{G}\right|^2. \tag{3.24}$$

Since it is the lower energy plane waves which are the most physically important, the summed series in equation 3.23 is truncated at a value G_{cut} which is defined by the kinetic energy cutoff:

$$E_{cut} = \frac{\hbar^2}{2m} G_{cut}^2. \tag{3.25}$$

Thus the infinite series (equation 3.23) is reduced to

$$\phi_{\mathbf{k}}\left(\mathbf{r}\right) = \sum_{|\mathbf{k}+\mathbf{G}|<G_{cut}} c_{\mathbf{k}+\mathbf{G}} e^{i(\mathbf{k}+\mathbf{G})\mathbf{r}}. \tag{3.26}$$

Since calculations scale linearly with the number of plane waves, and hence with $E_{cut}^{\frac{3}{2}}$, it is desirable to use as small a cutoff as possible. Careful convergence testing must be used though to ensure that E_{cut} is large enough to allow the accurate calculation of parameters of interest. The total energy is a particularly useful measure of convergence of E_{cut} because the gradient dE/dE_{cut} is always less than or equal to zero and has a relatively smooth convergence to the value found at $E_{cut} \to \infty$ (see upper panel of Figure 3.1).

One important caveat of DFT calculations is that, largely owing to the use of pseudopotentials (see section 3.2.4), absolute total energies are meaningless from a physical perspective and it is only *relative* energies of different structures which are of general interest and may be compared with experiment. Since errors in relative energies are typically an order of magnitude smaller than those of absolute energies when converging with respect to E_{cut}, it is therefore not necessary to achieve good absolute convergence of the total energy. This more rapid convergence of relative energy is, however, dependent on the similarity of the local environment of the atoms in the models to be compared, particularly for those with the hardest valence electronic potentials.

An example of such convergence is demonstrated in Figure 3.1. The upper panel shows the energy convergence with respect to E_{cut} for two polymorphs of MnSb (zincblende and NiAs) while the lower panel shows the difference in these

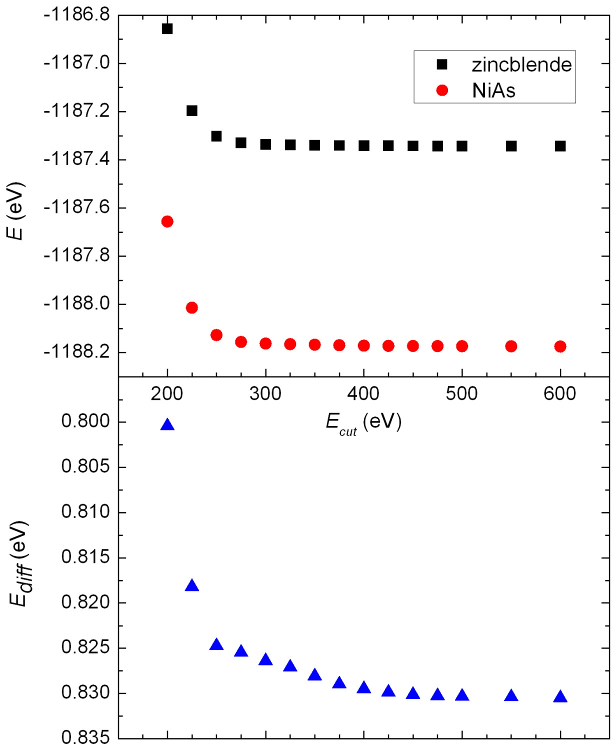

Figure 3.1: Upper panel: Energy convergence with respect to kinetic energy cut-off, E_{cut}, for two polymorphs of bulk MnSb using the PW91 exchange-correlation functional [68] and ultrasoft pseudopotentials (see section 3.2.4). Lower panel: Convergence of the relative energy of the polymorphs $E_{diff} = E_{\text{zincblende}} - E_{\text{NiAs}}$ with respect to E_{cut}.

energies. In this case the energy difference of the polymorphs is converged to within 5 meV at $E_{cut} = 250$ eV whereas, at the same value of E_{cut}, the absolute energy is only converged to $\sim$ 50 meV. For the majority of DFT investigations, a good balance between accuracy and expediency is achieved when convergence of relative energies is $\sim$ 1-2 meV.

3.2.3 Supercell approximation

Since the plane wave basis set used by CASTEP is periodic, all simulations must be performed on a periodic model. Therefore, in order to study a surface, which is aperiodic in the normal direction, a vacuum gap must be introduced in the direction perpendicular to the surface (see figure 3.2), large enough to ensure that consecutive surface slabs do not interact significantly with each other. The required size of such a vacuum gap is system dependent and should be determined prior to the calculation of any surface properties. Once determined, all supercell dimensions are fixed for the duration of subsequent calculations, with lateral parameters constrained to be commensurate with the bulk lattice parameter(s).

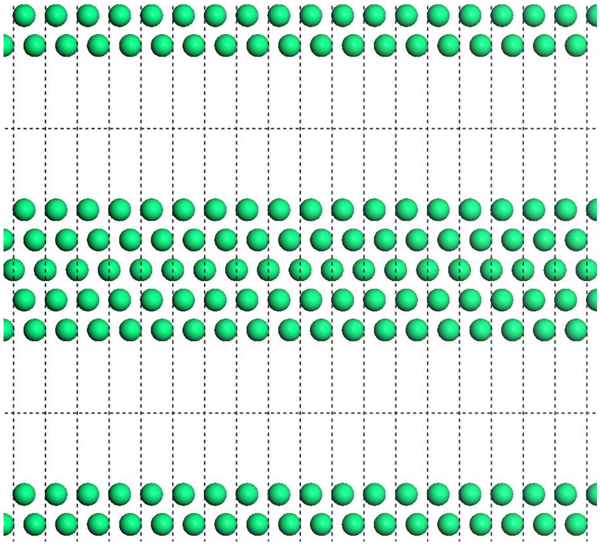

Figure 3.2: Supercell construction for a clean fcc(111) surface. Each surface slab comprises 5 atomic layers and is separated from adjacent slabs by a vacuum spacer. The dotted lines indicate the boundary of the supercells.

The number of atomic layers required in each slab to accurately simulate a surface is also system dependent, but typically 3-7 layers are adequate. In addition, the bottom 1-3 layers are constrained to the bulk atomic spacing to achieve a more bulk-like structure towards the bottom of the slab where it would otherwise be affected by surface relaxation mechanisms (see section 2.1.2), which in this case would be entirely unrealistic.

In order to simulate a single adsorbed molecule on a surface, the vacuum gap perpendicular to the surface is accompanied by clean surface gaps which must be introduced in crystallographic directions parallel to the surface such that the adsorbate species is spatially separated from its periodic images in neighboring supercells, and does not interact significantly with them, either directly or through substrate-mediated effects. For small molecular adsorbates consisting of $<\sim 10$ atoms, it is usually the case that a (3×2) or (3×3) surface mesh is adequate to satisfy this criterion.

Finally, in order to simulate an isolated species (i.e. in the gas phase), which is necessary if one wishes to determine the adsorption energy (see section 3.3.2), a supercell must be used which is large in all 3 spacial dimensions, thus minimising all external interaction.

3.2.4 Pseudopotentials

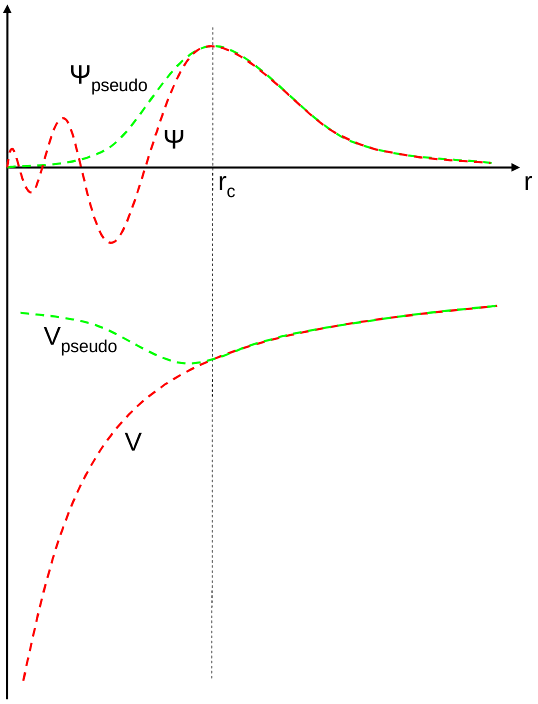

Figure 3.3: Schematic representation of a pseudopotential. The pseudopotential, V_{pseudo}, and pseudo wavefunction, Ψ_{pseudo}, are identical to that of an all-electron calculation beyond the cutoff radius, r_c.

Since it is only the valence electrons of an atom that are involved in molecular bonding, it is not necessary to optimise the core electron wavefunctions. Instead, in the interest of efficiency, the 'frozen core' approximation is used, thus rendering all of these non-bonding core electrons inaccessible. The pseudopotential construction then allows the remaining 'valence' electrons to be smoothed within a specified core region, $r < r_c$, where the wavefunction is strongly varying (see Figure 3.2.4). Beyond this region however, the wavefunction is, by construction, identical to that determined by an all-electron calculation, which is used as a reference state. r_c is carefully chosen such that, at reasonable bonding distances, the core region of pseudopotentials of adjacent atoms will not overlap significantly.

Such an approximation still allows good accuracy in calculations involving interatomic bonding while significantly reducing the necessary kinetic energy cutoff (see equation 3.25).

Several schemes have been devised to generate atomic pseudopotentials but they can be classified into two major groups. Pseudopotentials which maintain the original total charge within the core region are known as 'norm-conserving' pseudopotentials and, while being much softer than the true electronic wavefunction, are still considered to be relatively hard. A further reduction in the necessary kinetic energy cutoff can be made by relaxing this norm-conservation constraint. Pseudopotentials constructed without this constraint are known as ultrasoft pseudopotentials and can be generated in such a way as to be accurate using, in most cases, a much smaller kinetic energy cutoff. Such treatment allows for computationally feasible studies of larger systems than would otherwise be possible and has thus been the preferred choice in many structural investigations involving, in some cases, several hundred atoms. Included with the CASTEP distribution (see section 3.2.1) are several sets of pseudopotentials, to be used in conjunction with most of the commonly used exchange-correlation functionals (see section 3.1.4), which have been well tested for accuracy and transferability across an array of physically plausible local environments.

3.2.5 Brouillion zone integration

Since the band structure of a periodic collection of atoms is dispersive, it is necessary to integrate the Kohn-Sham eigenvalues across the whole Brillouin Zone in order to calculate the electron density:

$$n\left(\mathbf{r},\mathbf{r}'\right) = \int_{BZ} Q_{\mathbf{r},\mathbf{r}'}\left(\mathbf{k}\right) d\mathbf{k} \tag{3.27}$$

where

$$Q_{\mathbf{r},\mathbf{r}'}\left(\mathbf{k}\right) = \sum_{v} \psi_v^*\left(\mathbf{k},\mathbf{r}'\right) \psi_v\left(\mathbf{k},\mathbf{r}\right). \tag{3.28}$$

However, the electronic bands are slowly-varying continuous functions, so these integrals can be replaced by summation over a limited number of discrete points in reciprocal space. The number of such k-points required to accurately determine the total energy is dependent on several factors:

- The size of the supercell; a larger supercell requires fewer k-points since the reciprocal lattice is smaller leading to flatter bands. Moreover, for a surface supercell, which has a large lattice parameter in the direction perpendicular to the surface, a plane of k-points (i.e. only a single k_z value) is usually sufficient.

• The material in question; a metallic system generally requires a factor of 10 more k-points than an insulating or semiconducting one to avoid incorrect bands being occupied near the Fermi level.

• The similarity of structures to be compared; in cases where the relative value of a parameter is to be calculated, a reduction of the number of k-points may be possible if the structures to be compared are similar. This is particularly so for cases where the models being compared are contained within supercells of identical dimensions.

• The choice of k-points; a poor choice of k-points, such as only high symmetry points, will not provide a representative sampling.

• Symmetry of the system; only a single k-point needs to be included in the calculation for a set of symmetrically equivalent k-points within the Brillouin Zone.

For each of the DFT calculations reported within this thesis, a Monkhorst-Pack k-point mesh, $\mathbf{k}_p^{(n)}$, [83] has been chosen to minimise the necessary number of k-points required in the calculations:

$$\mathbf{k}_p^{(n)} = \sum_{i=1}^{3} u_{p_i}^{(n)} \mathbf{b}_i \tag{3.29}$$

where $\mathbf{b}_i$ are reciprocal lattice vectors and

$$u_{p_i}^{(n)} = \frac{2p_i - q_i - 1}{2q_i} \tag{3.30}$$

where $p_i = 1, 2, ..., q_i$, q_i is the number of k-points in direction i of the mesh and $n = \prod_{i}^{i=3} q_i$ is the total number of k-points in the mesh.

Contrary to the case of the basis set, convergence of the total energy with respect to k-points is not systematically smooth and the Brillouin Zone sampling should therefore be sufficient to provide good absolute convergence of energy. Such convergence is illustrated in Figure 3.4 for bulk fcc Cu. In this case, both the total energy and optimal atomic spacing show damped oscillations with increasing

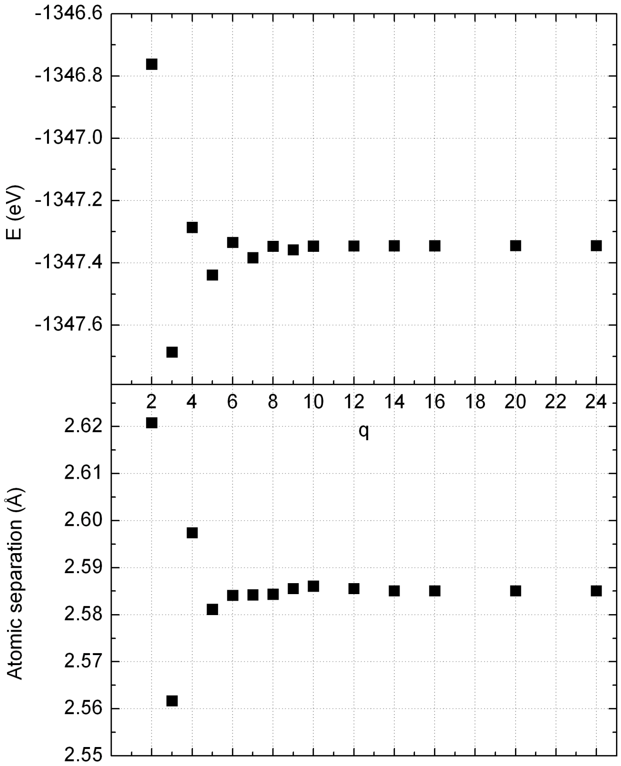

Figure 3.4: Convergence of the total energy and bulk atomic spacing with respect to the size of a uniform Monkhorst-Pack k-point mesh ($q_i = q$) for a primitive unit cell of bulk fcc Cu optimised using the RPBE functional.

uniform Monkhorst-Pack k-point mesh $q_i = q$. In most cases an even value for q_i is preferred over an odd one because additional symmetry within the Brillouin Zone can often be exploited, thus making the calculations cheaper for a similar or improved level of convergence [51].

3.3 Application to surface structure investigations

3.3.1 Geometry optimisation

In order to determine the precise local minimum energy structure for a collection of atoms, a geometry optimisation must be performed. The most robust optimisation routine employed by CASTEP is that credited to Broyden, Fletcher, Goldfarb and Shanno (BFGS) [84] which has proved to provide rapid and reliable convergence to stationary points within a multi-variable hyper space.

Following this scheme, the Hessian matrix

$$H_i(E(\mathbf{x} = x_1, x_2, ..., x_n)) = \begin{pmatrix} \frac{\partial^2 E}{\partial x_1^2} & \frac{\partial^2 E}{\partial x_1 \partial x_2} & \cdots & \frac{\partial^2 E}{\partial x_1 \partial x_n} \\ \frac{\partial^2 E}{\partial x_2 \partial x_1} & \frac{\partial^2 E}{\partial x_2^2} & \cdots & \frac{\partial^2 E}{\partial x_2 \partial x_n} \\ \vdots & \vdots & \ddots & \vdots \\ \frac{\partial^2 E}{\partial x_n \partial x_1} & \frac{\partial^2 E}{\partial x_n \partial x_2} & \cdots & \frac{\partial^2 E}{\partial x_n^2} \end{pmatrix}$$

is first approximated for an initial guess geometry $\mathbf{x}_0$ which comprises n structural parameters. Then, for each successive iteration i, a search direction $\mathbf{p}_i$ is determined by solving

$$H_i \mathbf{p}_i = -\nabla E(\mathbf{x}_i). \tag{3.31}$$

Following this, a line search is conducted to determine the optimal step size α_i in the direction $\mathbf{p}_i$. The geometry may then be updated

$$\mathbf{x}_{i+1} = \mathbf{x}_i + \alpha_i \mathbf{p}_i \tag{3.32}$$

as well as the Hessian

$$H_{i+1} = H_i + \frac{\mathbf{y}_i \mathbf{y}_i^T}{\mathbf{y}_i^T \mathbf{s}_i} - \frac{H_i \mathbf{s}_i \mathbf{s}_i^T H_i}{\mathbf{s}_i^T H_i \mathbf{s}_i} \tag{3.33}$$

where $\mathbf{s}_i = \alpha_i \mathbf{p}_i$, $\mathbf{y}_i = \nabla \mathrm{E}(\mathbf{x}_{i+1})$ - $\nabla \mathrm{E}(\mathbf{x}_i)$.

In cases where linear constraints are to be applied to the atoms, e.g. constraining deep layer substrate atoms to bulk locations during surface optimisations (see section 3.2.3), the BFGS algorithm may be used to optimise the other structural parameters only.

A good measure of the convergence of structural parameters is usually found by calculating the Hellmann-Feynman forces (equation 3.14) attributed to individual atoms following an update to $\mathbf{x}$. The calculation is terminated when the maximum force acting on an atom, F_{max}, drops below a specified tolerance. In this respect, an important advantage of using a plane-wave basis set is that the derivative of each basis state with respect to the ionic positions is zero. Hence erroneous Pulay forces [85], which arise if the basis set quality is dependent on the locations of the ions, are automatically nullified.

For bulk optimisations the unit cell must be optimised as well as any internal structure. When the cell size is changed however, the size of the Brillouin zone is also changed, thus impacting the quality of the basis set according to equation 3.26. If the basis set is not absolutely converged, which is typically the case for well-optimised calculations (see section 3.2.2), this will cause a systematic error to appear in the calculation of the total energy and stress (Pulay stress). Therefore, a finite basis set correction is applied, the necessary size of which has been determined by Vanderbilt [86]:

$$E_{corr} = \frac{2N}{3\Omega}\frac{\partial E}{\partial \ln E_{cut}}. \tag{3.34}$$

where N is the number of atoms in the unit cell and Ω is the total volume of the supercell. In order to find $\frac{\partial E}{\partial \ln E_{cut}}$, an initial series of total energy calculations are performed on the starting structure at a range of kinetic energy cutoffs in the proximity of that to be used for the cell optimisation, which subsequently may commence. The cell optimisation terminates when the maximum stress component (see section 3.3.3) drops below a specified tolerance, assuming that any internal geometry optimisation tolerances imposed are also satisfied.

3.3.2 Adsorption energy and surface free energy

Within the DFT framework, the adsorption energy (defined in section 2.1.3) for an adsorbed species on a surface is determined by performing a minimum of four DFT calculations. Firstly, the bulk lattice parameter of the substrate is determined using a variable cell calculation. A surface supercell may then be constructed (see section 3.2.3) in which the lateral periodicity is fixed to that of the bulk. A geometry optimisation is then performed to determine the total energy of the clean surface. This energy along with the total energy of the geometry-optimised free adsorbate and the total energy of the adsorbate-substrate system in a minimum energy geometry of interest allows the calculation of adsorption energy per adsorbate using:

$$E_a = \frac{E_{cr+ads} - (E_{cr} + N_{ads}E_{ads})}{N_{ads}} \tag{3.35}$$

where E_{cr+ads} and E_{cr} are the total energies of a crystal with and without the adsorbed species present, N_{ads} is the number of adsorbed species and E_{ads} is the total energy of the species to be adsorbed, in its stable isolated conformation.

Such calculations are usually performed in an attempt to find the most energetically favourable structure. Therefore, several adsorbate-substrate starting models are geometry-optimised with the hope of discovering the global minimum energy structure, which corresponds to the largest adsorption energy.

For a crystal comprising N_{cr} atoms, the total work that must be done on the crystal in order to cleave it from the bulk is simply the difference between the total energy of the entire crystal, E_{cr}, and that associated with N_{cr} bulk atoms. Hence, in accordance with equation 2.1, the surface free energy of a clean crystal may be expressed

$$\gamma = \frac{E_{cr} - N_{cr}E_b}{A} \tag{3.36}$$

where E_b is the total energy associated with a single atom in the bulk and A is the total surface area of the crystal.

In addition, adsorption at a stable site necessarily reduces the surface free energy. The surface free energy can thus be used as a measure of the relative stability of surface structures involving any number of adsorbing species. For such cases, it is necessary to consider the details of the surface reaction in order to choose an appropriate state for the calculation of the energy of the dissociated species. In the simple case of intact molecular adsorption the obvious choice of this adsorbate 'reservoir' is the adsorbing species in the gas phase. In systems where the adsorbate species is unstable in the gas phase however, or has taken part in a reaction on the surface, a different choice of adsorbate reservoir may be appropriate. An additional term can then be included in the normal definition of surface free energy (equation 3.36) for each adsorbate species such that the surface energy is

$$\gamma = \frac{E_{cr+ads} - \left(N_{cr}E_b + \sum_i N^i_{ads}E^i_r\right)}{A} \tag{3.37}$$

where E^i_r is the energy of the ith adsorbate species calculated in the chosen reservoir and the summation is over all inequivalent adsorbate species i. As an example, for the dissociative adsorption of azobenzene, resulting in two adsorbed phenyl imide molecules - $C_{12}H_{10}N_2(g) \longrightarrow 2\ C_6H_5N(a)$, the appropriate adsorbate reservoir is gas phase azobenzene, and not the gas phase phenyl imide radical, such that E^i_r is calculated as half the energy of gas phase azobenzene.

3.3.3 Surface stress

The surface stress tensor defined by equation 2.4 can be readily calculated once solutions to the Kohn-Sham equations have been found. However, in order to accurately determine the absolute surface stress, it is necessary to perform the calculation using a double-sided surface slab with identical structure on both sides; such treatment removes the need to compensate for the unphysical termination of a single-sided slab which would, in reality, be a continuation of the bulk crystal.

Following a successful determination of the ground state, stress tensor components are calculated using

$$\sigma_{ij} = \frac{1}{\Omega}\frac{\partial E}{\partial \epsilon_{ij}} \tag{3.38}$$

and output by CASTEP is in the form

$$\sigma = \begin{pmatrix} \sigma_{xx} & \sigma_{xy} & \sigma_{xz} \\ \sigma_{yx} & \sigma_{yy} & \sigma_{yz} \\ \sigma_{zx} & \sigma_{zy} & \sigma_{zz} \end{pmatrix}.$$

where the diagonal matrix elements, σ_{ii}, are stress components along the crystallographic cell axes while the off-diagonal elements, σ_{ij}, are shear stress components.

In the case of a periodic surface, it is always possible to choose the direction z to be normal to the surface and the x and y directions to be in the surface plane so that all z components of the stress tensor become zero:

$$\sigma = \begin{pmatrix} \sigma_{xx} & \sigma_{xy} & 0 \\ \sigma_{yx} & \sigma_{yy} & 0 \\ 0 & 0 & 0 \end{pmatrix}.$$

Furthermore, if the surface has 3-fold or greater rotational symmetry, as is the case for the fcc(001) and fcc(111) surfaces, the remaining shear stress components are also zero, thereby reducing the stress tensor to a two-component vector of principal stress components:

$$\sigma = \begin{pmatrix} \sigma_{x} \\ \sigma_{y} \end{pmatrix}$$

where $\sigma_i \equiv \sigma_{ii}$. In the case of the fcc(110) surface however, which displays just 2-fold rotational symmetry, the shear stress components, $\sigma_{xy} = \sigma_{yx}$, may be non-zero but are always equal due to the fact that there is no couple rotating the crystal. Hence a transformation may be made onto the principal axes using the Mohr circle construction [87]:

$$\sigma_x = \sigma_{xx} cos^2\theta + \sigma_{yy} sin^2\theta - 2\sigma_{xy} cos\theta sin\theta \tag{3.39}$$

$$\sigma_y = \sigma_{yy} cos^2\theta + \sigma_{xx} sin^2\theta + 2\sigma_{xy} cos\theta sin\theta \tag{3.40}$$

The surface stress along the principal axes x and y is then

$$\tau_x = \frac{a_z \sigma_x}{2}, \tau_y = \frac{a_z \sigma_y}{2} \tag{3.41}$$

where a_z is the height of the supercell (aligned normal to the surface) and the factor one half is included because the double-sided slab contains two instances of the surface.

3.3.4 Core level shifts

An area in which experiment and theory may be used in conjunction is that of core level shifts. Experimentally, the photoelectron binding energy of core level electrons may be determined by XPS measurements using the equation

$$E_{binding} = E_{photon} - (E_{kinetic} + \Phi) \tag{3.42}$$

where E_{photon} is the energy of a photon from a monochromated source, $E_{kinetic}$ is the recorded energy of an electron ejected from the target and Φ is the work function of the spectrometer [3]. Variations in this photoelectron binding energy (core level shifts - CLS) for atoms of the same element in chemically distinct environments arise from a combination of initial and final state effects that are not seperable experimentally. They nevertheless provide a valuable spectral 'fingerprint' of the chemical state.

For theoretical comparison, CLSs for a core electron of an atom may be found within the pseudopotential formalism by replacing an atomic pseudopotential of interest with one which has been constructed with a core level electron omitted. Such construction is achieved using a projector augmented wave (PAW) method to correct for errors caused by the pseudopotential [88]. Following this procedure, the difference in total energy between geometry-optimised models and the same models using this 'excited state' pseudopotential can be compared to determine the CLS for various atomic environments. Such calculations include final state effects from both valence electron and core electron relaxation and have been shown to produce results of comparable accuracy to those calculated using more sophisticated computationally-intensive all-electron methods [89].

In some cases, where the same atomic species is present on a surface in multiple local environments, direct experiment-theory comparison of the CLS can provide a basis to reject implausible structural models. Such treatment allowed the propynyl C_3H_3 species, investigated as a possible decomposition product of furan (see section 4.5), to be discounted.

3.3.5 Tersoff-Hamann approximation

In order to improve understanding of images produced using STM (one of the experimental methods mentioned in section 2.2), Tersoff and Hamann determined that, for a model probe tip, the tunneling current is proportional to the local density of states of the surface, at the position of the tip [90]. Applying this approximation to a DFT geometry-optimised surface structure, the construction of a local density of states isosurface parallel to the surface at a specified distance from the Fermi level (the bias voltage used between the tip and sample in STM) allows for qualitative comparison with real STM images. Such treatment may therefore provide validation of a determined structure. This method has been exploited in the study of methoxy on Cu(110) (see section 5.1) and methane thiolate on Cu(111) and Cu(100) (see chapter 7), the details of which are to be discussed in subsequent chapters.

Chapter 4

Furan adsorption and decomposition on Pd(111)

4.1 Introduction

Furan, C_4H_4O, is the simplest oxygen-containing aromatic hydrocarbon, and is sometimes used as a model in hydrodeoxygenation studies of such compounds that need to be removed from crude petroleum and liquids derived from coal and biomass [91]. It therefore provides a convenient model for detailed surface science investigations of this process on well-characterised single crystal surfaces, yet rather few such studies have been conducted. On the clean coinage metal surfaces, Cu(100) [92] and Ag(110) [93], the molecule has been found to adsorb and desorb intact. On Pd(111) furan adsorbs intact at low temperatures, but around room temperature deoxygenation occurs, believed to lead to the presence of coadsorbed CO, atomic H and a C_3H_3 species on the surface [94–97] (see Figure 4.1):

$$C_4H_4O \rightarrow CO + C_3H_3 + H. \tag{4.1}$$

In this chapter a structural DFT investigation of this system is presented. A new low-energy adsorption geometry is found for furan on Pd(111) and discussed in the context of previous work [8]. The major unresolved aspect of this reaction, the nature of the C_3H_3 species, is also discussed in the light of new DFT calculations and the subsequent re-analysis of PhD data [9].

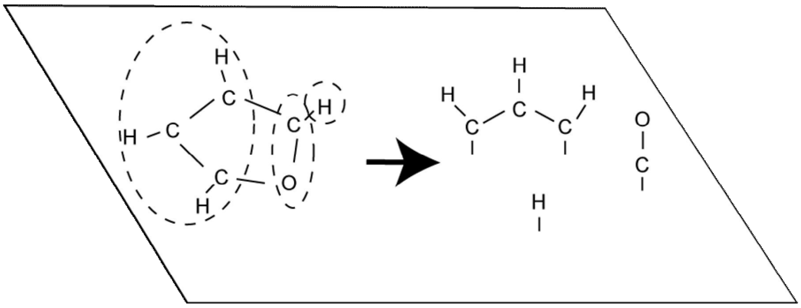

Figure 4.1: Schematic diagram of the furan dissociation reaction on Pd(111), showing the C_3H_3 fragment in the half-benzene conformer.

4.2 Previous work

For intact furan adsorbed on Pd(111) (Pd(111)-furan), there is already some experimental structural information. By the application of dipole selection rules in high-resolution electron energy loss spectroscopy (HREELS), Ormerod et al. [94] have proposed that, at least at high coverage, the intact furan molecule neither lies flat on the surface nor with its molecular plane perpendicular to the surface, but a quantitative value of the molecular tilt angle cannot be obtained from this technique. STM studies of this adsorption system have been shown to yield images consistent with an essentially flat-lying geometry [98, 99], at least at low coverages. Most recently, a combined NEXAFS and PhD investigation [100] concluded that the molecule does lie flat on the surface to relatively high coverages, and has also identified some preferred adsorption sites.

There is clear spectroscopic evidence for the dissociation of the furan, adsorbed at low temperature, to create surface CO together with a second C-containing species when heated to ∼230–270 K, from XPS, ultraviolet photoelectron spectroscopy (UPS) and HREELS [94]. Temperature-programmed desorption (TPD) shows CO desorption occurs only at a higher temperature of ∼500 K. Also seen in TPD is H_2 desorption at a peak temperature of 350–360 K [94, 95]; this temperature is similar to that of associative desorption of molecular hydrogen from Pd(111) following adsorption of atomic H, so this H_2 TPD peak is believed to be desorption-, rather than dissociation-, limited. The implication is thus that atomic H is lost from the furan in the deoxygenation reaction at the lower temperature of ∼270 K, at which there is spectroscopic evidence of dissociation. Therefore, if there is a single C_3H_x hydrocarbon fragment resulting from the reaction, it seems that $x < 4$. The strongest evidence to suggest that the hydrocarbon fragment resulting from this deoxygenation is C_3H_3 comes from laser-induced thermal desorption (LITD), which shows small amounts of benzene desorption in the surface temperature range ∼330–430 K [96]. Surface C_6H_6 is believed to arise from a C_3H_3 coupling reaction, but its presence is not detected in conventional TPD, because benzene dissociates on Pd(111) at low coverage before it desorbs in a heating cycle. STM studies of the surface at ∼200 K (a temperature too high to image the mobile CO species at low coverage), following this heat treatment, have identified a molecular species on the surface that was attributed to C_3H_3 [101].

More recently, a PhD study of the furan dissociation products on Pd(111) using soft XPS (SXPS) was conducted after slowly heating a furan dosed surface to 340 K [102]. On the basis of the previously-published TPD data, the surface studied is expected to have retained the CO and C_3H_3 coadsorbates, but most of the atomic H produced in the initial dissociation reaction is likely to have been desorbed. Two C 1s components, previously observed in XPS [94], were clearly resolved. The higher binding energy state, previously identified with adsorbed CO, yielded PhD data corresponding to occupation by the associated C atom of three-fold coordinated fcc hollow sites (directly above third-layer Pd atoms); this is one of the two hollow adsorption sites known to be occupied by CO on this surface in the absence of coadsorbates. The lower binding energy component was assigned to the C_3H_3 species but it was not possible to resolve the C 1s component further. Weak PhD modulations resulted and, in order to render the structural search viable, the C_3H_3 species was assumed to adopt a 'half-benzene' (CH–CH–CH) configuration (as had been previously suggested schematically [96], and as reproduced in Figure 4.1), with the outer two C atoms in symmetrically equivalent locations with respect to the outermost Pd atomic layer, such that the molecule shares the mirror planes of this substrate layer. While a generally good fit to the PhD data was achieved for two alternative but closely similar model structures of this type (see Figure 4.2), the surprising conclusion was that the molecular plane was found to lie almost parallel to the surface. By contrast, in an analogue organometallic carbonyl cluster compound, in which a fully methylated C_3R_3 species (i.e. $(CCH_3)_3$ rather than (C_3H_3)) is bonded to a triangular group of three Ru atoms [103], the C_3 plane is tilted by ∼63° out of the Ru_3 plane (see Figure 4.2).

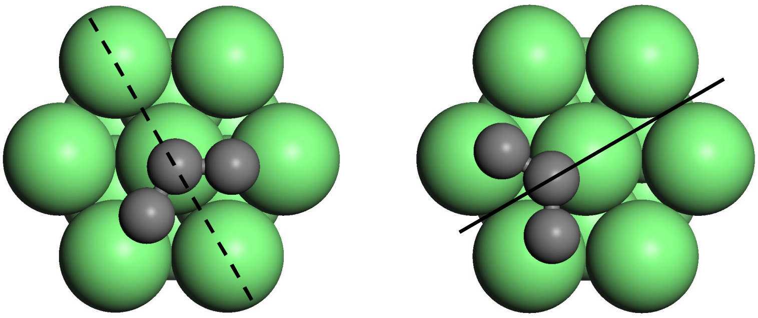

‘bridge’ ‘hollow’

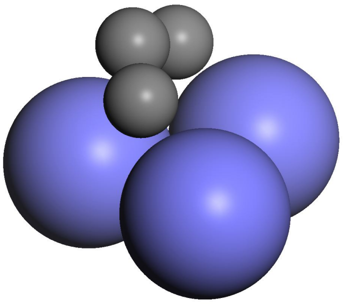

Ru$_3$(CCH$_3$)$_3$ carbonyl core

Figure 4.2: The upper part of the figure shows top views of the two alternative adsorption geometries of the half-benzene conformer of C_3H_3 on Pd(111) derived from the earlier experimental PhD investigation [102]. Only the C atoms are shown, as the PhD technique is unable to determine the location of H atoms. The full line shows a mirror plane of the substrate, the dashed line a mirror plane of the outermost Pd atom layer alone. In the lower part of the figure is shown the relative locations of the three Ru atoms (large blue spheres) and the three C atoms of the CCH_3 ligands in the organometallic complex (μ-H)Ru$_3$(μ_3-η^3-CMeCMeCMe)(CO)$_9$ [103].

4.3 Computational details

The RPBE exchange–correlation functional [73] was used throughout this investigation. However, additional calculations using PW91 [68] were also performed on the Pd(111)-furan system for comparison. Vanderbilt ultrasoft pseudopotentials from the CASTEP pseudopotential library were employed for Pd(111)-furan while CASTEP-generated ‘on the fly’ pseudopotentials were used for all calculations involving Pd(111)-C_3H_3, in order to be consistent with the core-ionised potentials used in CLS calculations (see section 3.3.4). All other calculational parameters were converged according to considerations discussed in chapter 3.

Reference calculations for the clean surface slab yielded an outward relaxation of the outermost layer of 0.010 Å. This very small value is consistent with the general trend of almost bulk-like terminations of fcc (111) surfaces and such a small value challenges the precision of any of the available experimental methods; a detailed LEED investigation yielded a value for this parameter of 0.03 ± 0.03 Å [104].

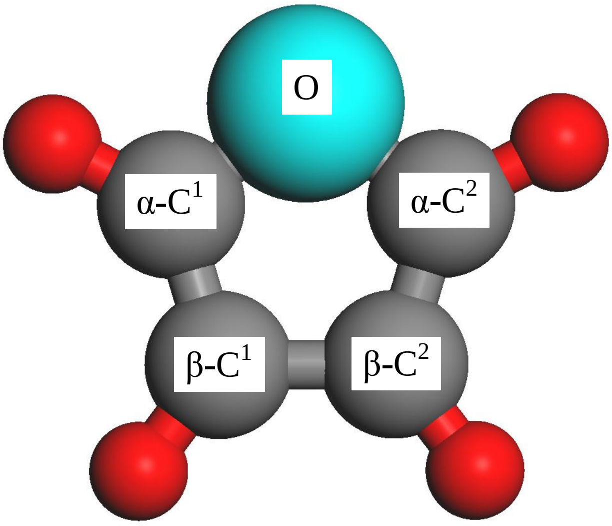

Figure 4.3: Schematic diagram of the furan molecule showing the labelling convention for the constituent atoms used in the text.

In order to determine the adsorption energies associated with the optimised structural models, calculations were first performed on isolated furan and C_3H_3 molecules in a large cell using the supercell approximation (see section 3.2.3). However, as no experimental adsorption study is possible starting from a C_3H_3 species, in this case absolute values have no real meaning, so in section 4.5 the focus is entirely on the relative adsorption energies for different molecular conformation and adsorption sites, using the most strongly bonded configuration as a somewhat arbitrary reference.

As shown in Table 4.1, the resulting molecular conformation for gas-phase furan is in excellent agreement with experimental determinations [105, 106] and with the results of two earlier DFT studies [101, 107]. The labelling convention for the atoms in the furan ring, used for defining the bondlengths and bond angles in this table, is shown in Figure 4.3, and follows the labelling used in the previous experimental structure determination for the molecule adsorbed on Pd(111) [100].

Table 4.1: Comparison of the interatomic bond lengths, d, and bond angles, θ, of gas phase furan obtained from experimental results by Bak et al. [105] and by Liecheski and Rankin [106] with the results of the RPBE calculations performed here, and of two earlier DFT calculations. The naming convention for the atoms in the furan ring used here is shown in Figure 4.3.

Parameter	Bak et al. [105]	Liecheski and Rankin [106]	This work, RPBE [8]	Loui, LDA [101]	Kwiatkowski et al., B3LYP [107]
$d(\mathrm{O}{:}\alpha\text{-}\mathrm{C})$ (Å)	1.362	1.364	1.361	1.354	1.364
$d(\alpha\text{-}\mathrm{C}^1{:}\beta\text{-}\mathrm{C}^1)$ (Å)	1.361	1.364	1.350	1.353	1.360
$d(\beta\text{-}\mathrm{C}^1{:}\beta\text{-}\mathrm{C}^2)$ (Å)	1.431	1.430	1.419	1.418	1.436
$d(\mathrm{H}{:}\alpha\text{-}\mathrm{C})$ (Å)	1.075	1.086	1.076	1.079	1.079
$d(\mathrm{H}{:}\beta\text{-}\mathrm{C})$ (Å)	1.077	1.086	1.076	1.081	1.080
$\theta(\alpha\text{-}\mathrm{C}^1{:}\mathrm{O}{:}\alpha\text{-}\mathrm{C}^2)$ (°)	106.6	106.7	106.6	107.1	106.8
$\theta(\mathrm{O}{:}\alpha\text{-}\mathrm{C}^1{:}\beta\text{-}\mathrm{C}^1)$ (°)	110.7	110.5	110.3	110.2	110.5
$\theta(\alpha\text{-}\mathrm{C}^1{:}\beta\text{-}\mathrm{C}^1{:}\beta\text{-}\mathrm{C}^2)$ (°)	106.1	106.1	106.4	106.3	105.6
$\theta(\beta\text{-}\mathrm{C}^1{:}\beta\text{-}\mathrm{C}^2{:}\mathrm{H})$ (°)	127.9	127.9	127.1	127.2	127.9
$\theta(\mathrm{O}{:}\alpha\text{-}\mathrm{C}^1{:}\mathrm{H})$ (°)	115.9	117.3	116.0	116.0	115.8

All bondlengths from these new calculations agree with both of the experimental values within better than 0.02 Å, while the largest discrepancy in bond angles is 1.3°. For the three DFT calculations, the agreement is even better with the range being smaller than these values. Moreover, the results of the PW91 (not shown) and RPBE calculations agree in the molecular geometrical parameters to within 0.002 Å and 0.1°.

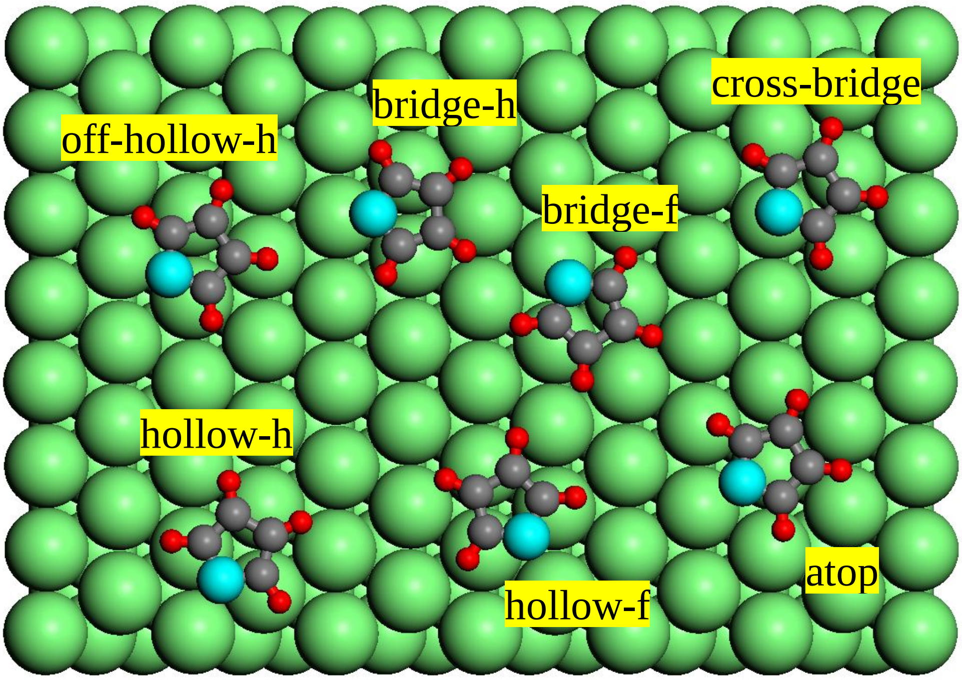

Figure 4.4: Starting models used in exploring the optimal structure of furan on Pd(111).

Optimisation of the adsorption structures for furan and C_3H_3 on Pd(111) was undertaken without the imposition of symmetry constraints, starting from a range of geometries and, in the case of C_3H_3, molecular configurations. For the Pd(111)-furan system, structural optimisation was generally less dramatic since a good guess at intra-molecular bond angles could be made from the optimised isolated furan molecule. Hence, for the stable adsorption sites, the starting geometries shown in Figure 4.4 closely resemble the optimised ones in most cases and are essentially equivalent to the structures explored in the experimental PhD investigation [100]. Note that these models all assume the molecular plane is approximately parallel to the Pd(111) surface, consistent with the experimental NEXAFS and PhD results, but the DFT optimisation procedure clearly allows the molecules to tilt if this proves to be energetically advantageous. Subsequently, further calculations were undertaken to explore the role of intermolecular interactions following furan decomposition. These calculations involved coadsorbed C_3H_3, CO and atomic H, using not only (3×2), but also (3×3) and (4×2) unit meshes, to explore the coverage dependency. Additional calculations of benzene adsorption were performed using a (3×3) unit mesh.

4.4 Furan adsorption structure

In order to distinguish the alternative bonding structures of the Pd(111)-furan system and remove their associated ambiguity, and to understand the nature of the molecule–substrate bonding, reported here and in reference [8] are the results of a DFT study of this adsorption system. In fact one previous DFT investigation of this system has been undertaken [101], but unfortunately this earlier work is only reported in a doctoral thesis. While many aspects of the results of this earlier study are closely similar to this one, there are some important differences. In particular, a new lowest-energy structure is revealed, of reduced symmetry, that was not investigated in the earlier work. Moreover, these calculations provide additional structural parameter values, not presented previously, that can provide a more complete basis for comparison with the experimental results.

4.4.1 Preferred adsorption sites

Table 4.2 summarises the adsorption energies (equation 3.35) for the different optimised structural models, including a comparison with comparable values for the models tested in the earlier LDA calculations of Loui [101]. The numerical labels (2a, 2b etc.) assigned to the starting models in the experimental PhD study are also included in Table 4.2 to simplify comparison, but more descriptive names for these structures have been preferred for the present discussion, shown in Figure 4.4. Note that no stable adsorption structure was obtained for either the atop or the cross-bridge model using the RPBE functional; in both cases successive iterations in the DFT calculations displaced the molecule further and further from the surface, and led to it adopting the free-molecule conformation. There are four lowest-energy structures with almost identical adsorption energies, all of which correspond to adsorption at, or close to, the two ‘hollow’ sites with the molecule approximately centred over either the hcp hollow (directly above a second-layer Pd atom - hollow-h and off-hollow-h) or the fcc hollow (directly above a third-

Table 4.2: Comparison of the adsorption energies for furan in the optimised versions of the structural models illustrated in Figure 4.4. The bracketed labels of the structural models (1a, 2b etc.) are the nomenclature used in the earlier PhD experimental study [100].

Model	E_a {this work, RPBE} (eV)	E_a {this work, PW91} (eV)	E_a {Loui [101], LDA} (eV)
atop (1a)	Not bonding	Moves to cross-bridge site	-
cross-bridge (1b)	Not bonding	0.775	-
bridge–h (2a)	0.204	0.855	1.969
bridge-f (3a)	0.203	0.857	1.976
hollow-h (3b)	0.446	1.103	2.184
hollow-f (2b)	0.448	1.104	2.144
off-hollow-h (4a)	0.446	1.101	-
off-hollow-f (4b)	0.443	1.108	-

layer Pd atom - hollow-f and off-hollow-f). The adsorption energies are essentially identical when located equivalently relative to either the fcc or hcp hollow. Notice that the two 'bridge' geometries form a similar pair, having essentially the same adsorption energy and the same geometry with respect to the outermost Pd atoms layer, the difference only being related to their juxtaposition to the second and third Pd layers. This insensitivity to the distinction between hcp and fcc hollow sites is not surprising. Even for atomic adsorbates, that can typically bond closer to the surface in hollow sites, the energetic distinction between fcc and hcp hollow sites on fcc(111) surfaces is small, although in most (but not all) such cases the fcc sites prove to be energetically preferred (as judged by experimental structure determinations - e.g. O and S on Pt(111) [108, 109]). However, even for simple molecules that bond to the surface through a single atom in hollow sites this is no longer the case. For example, CO adsorption (bonding through the C atoms with the molecular axis perpendicular to the surface) on Ni(111) leads to equal occupation of the two inequivalent hollow sites. For molecules that bond to such a surface through two or more atoms, typically in a 'lying-down' orientation, the energetic difference between hcp-related and fcc-related sites appears to be even smaller, as interaction with second-layer atoms is now negligible. Table 4.2 shows that the relative adsorption energies of the different optimised structures are almost identical using the RPBE and PW91 functionals, although the absolute energies differ considerably.

The energetic preference for the hollow, rather than bridge, geometries is ∼0.24 eV and is also reproduced by the earlier calculations of Loui (who did not consider the off-hollow geometries), although the absolute magnitude of the adsorption energies in the these calculations is much larger, differing from the present calculations by more than 1.7 eV. Qualitatively, at least, this difference may be assigned to the established tendency for LDA calculations to over-bind, and GGA calculations to under-bind (see section 3.1.4), although the size of the difference is surprising. An experimental estimate of the furan desorption energy at a coverage of 0.17 ML obtained using laser-induced thermal desorption is 1.03 ± 0.26 eV, approximately a factor of two greater than the RPBE calculated value and a factor of two less than that given by Loui's LDA calculations. As a further check, LDA calculations have been run for all of the structures of Table 4.2 and even larger adsorption energies (by ∼0.25 eV) were found than those reported by Loui. The difference between these new calculations and those of Loui may, perhaps, be due to the use of different ultrasoft pseudopotentials or LDA parameterisation as he reports a slightly different value (3.859 Å) for the bulk lattice parameter to the one calculated here (3.842 Å). The key conclusion, however, is that LDA is strongly overbinding, while the RPBE calculations lead to strong underbinding. This result, and the fact that PW91 gets the adsorption energy approximately correct, is consistent with the results of a recent detailed study of thiophene bonding on Cu(110), in which the choice of appropriate functionals and associated approximations is discussed in detail [110]. This paper also considers the role of dispersion forces that are not accounted for in standard DFT calculations and concludes that, in effect, pure PW91 calculations get about the right adsorption energy for the wrong reasons; a more correct description comes from RPBE plus the non-local dispersion forces. Recent calculations exploring ways of accounting for these effects have been undertaken not only for the adsorption of thiophene, but also for other cyclic aromatic molecules, namely benzene, pyridine and pyrazine on Cu(110) [111]. In all of these cases adding the effects of van der Waals interactions increases the adsorption energy (by up to ∼0.5 eV) although the consequences for the minimum energy structures differs. For pyridine and pyrazine large (∼0.4 Å) changes in adsorbate–substrate bondlengths accompany the inclusion of the dispersion forces, but for benzene and thiophene (the species most similar to furan) this is not the case. As shown in section 4.4.3, the results of the present calculations yield adsorbate–substrate bondlengths in excellent agreement with experiment, reinforcing the view that furan appears to behave more like thiophene. Specifically, while pure RPBE calculations may seriously underestimate the adsorption energy, the resulting structure, the property of interest here, is correct.

4.4.2 Bonding nature

Figure 4.5 and Figure 4.6 show the exact geometry of the adsorbed furan in the hollow and off-hollow sites, respectively. For each structure a top view shows the lateral position of the molecule while a side view shows the tilt and out-of-plane distortion of the molecule induced by the adsorption. In each case a perspective view is also shown that identifies the Pd–C local bonds. It is these perspective views that show most clearly the distinction between the hollow and off-hollow geometries. In both structures, one of the three nearest-neighbour Pd atoms lies at a bonding distance from two adjacent C atoms in the furan, while the remaining two Pd neighbours are located at bonding distances from the other two C atoms. In the more-symmetric hollow sites it is the two β-C atoms that appear to bond to a single Pd atom, but in the off-hollow structures it is, instead, one β-C atom and the adjacent α-C atom that are at a bonding distance from a single Pd neighbour. The implication is that in all of these structures each carbon is bonded to four other atoms, namely one Pd atom, one H atom and either two C atoms or one C atom and one O atom. Moreover, a consequence of the adsorption is that both the H and O atoms buckle out of the molecular plane. The result is that the C atoms all achieve near-tetrahedral bonding angles, consistent with essentially sp^3 bonding character. On the basis of the optimal geometries, therefore, it appears that this is driven by the change in C bonding character.

4.4.3 Compatibility with PhD results

A primary objective in conducting these calculations was to supplement or test the information obtained from the experimental PhD structure determination of this system [100]. This study identified four possible adsorption geometries, but two of these were distinguished from the other two only by their location relative to fcc and hcp hollows. Evidently, this failure to distinguish the structures that differed only in their location relative to the subsurface layers (fcc or hcp) is also a feature of the DFT calculations; the DFT results show the energies to be so similar that one must expect co-occupation of such sites to occur with equal probability. In fact the four structures identified in the PhD investigation correspond to the fcc and hcp versions of the hollow and bridge geometries of Table 4.2. The calculations reported here are therefore qualitatively consistent with the experiments in that both identify the hollow sites as possible solutions, but the DFT results indicate that, in reality, it is only the hollow sites, and not hollow-f

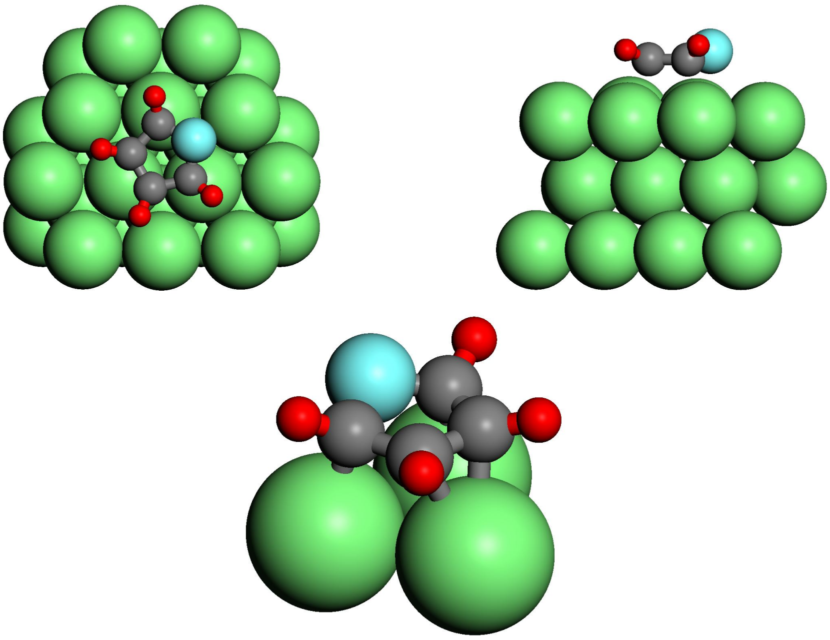

hollow-h

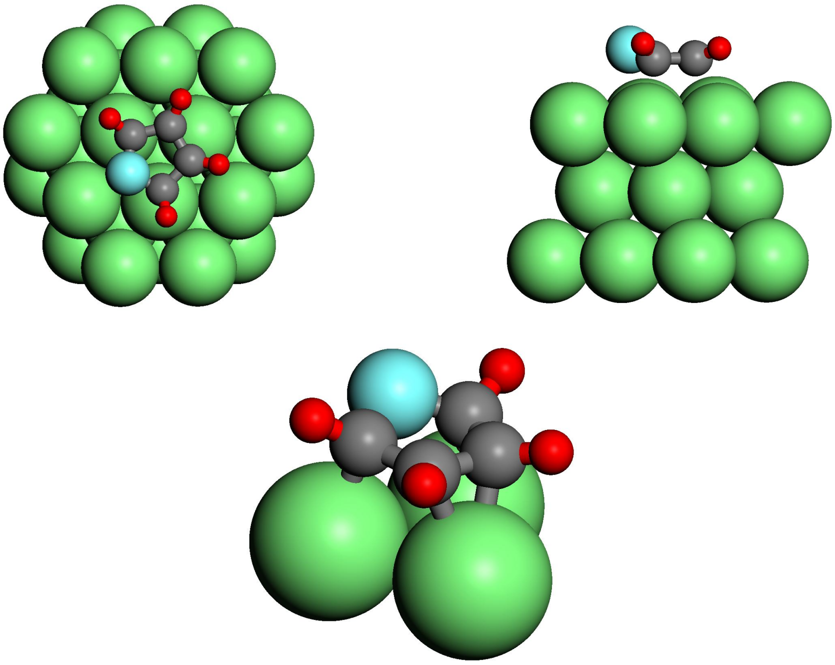

Figure 4.5: Schematic diagrams of the two optimised hollow-site models. For each structure a top and side view is shown, together with a perspective view showing the local C–Pd bonds to three nearest-neighbour Pd atoms. Note that one Pd atom is bonded to both β–C atoms.

off-hollow-f

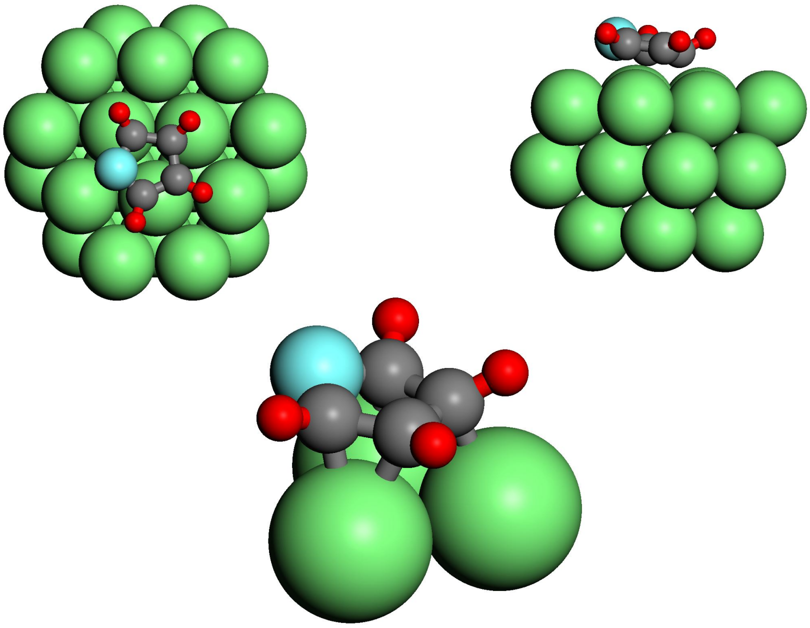

off-hollow-h

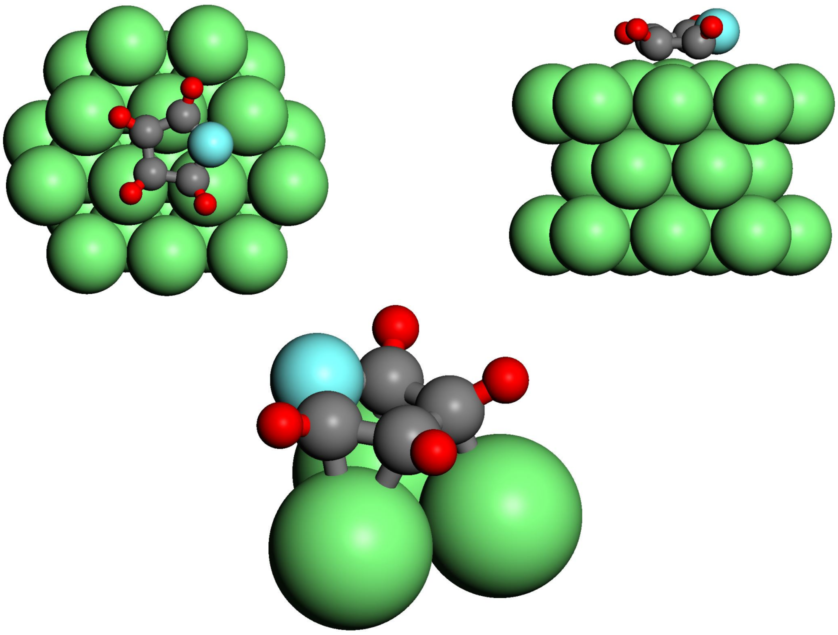

Figure 4.6: Schematic diagrams of the two optimised off-hollow-site models. For each structure a top and side view is shown, together with a perspective view showing the local C–Pd bonds to three nearest-neighbour Pd atoms. Note that one Pd atom is bonded to one β-C atom and one α-C atom.

the bridge sites, that are occupied. The fact that the DFT calculations also indicate that co-occupation of the off-hollow site must occur does not, as shown below, conflict with the information obtained from the PhD experiments.

A more quantitative comparison of the new theoretical results and those of the PhD experiments is also possible, and this is shown in Table 4.3. Structural parameters for the optimised geometries are given only for the RPBE calculations, but the results for the PW91 calculations differ, at most, by 0.02 Å and 0.2°. In making this comparison it is important to take account of exactly what was determined, and what was inferred, in the experimental results. In particular, in the experiments it proved possible to analyse only PhD data from the α-C component of the C 1 s photoemission [100]. The PhD modulations from the β-C component proved too weak to be reliably distinguished from noise, while no O 1 s PhD could be used due to the overlap of the O 1 s and Pd $3p_{3/2}$ photoemission signals. In effect, therefore, the experiments were only able to determine the location of the α-C atoms relative to the Pd(111) substrate. The influence of intramolecular scattering in the α-C PhD also provided information of limited precision on the molecular tilt relative to the surface plane, though inferred locations of the β-C and O atoms (shown in parentheses in Table 4.3) were based on the assumption that the C and O atoms all remained coplanar. As the DFT results clearly indicate that the O atom is significantly displaced out of the plane defined by the four C atoms, even for the symmetric hollow sites, it is clear that one may expect a large systematic error in the O atomic position determined by the PhD study, and for this reason these values are placed in double parentheses in Table 4.3. Additionally, in an attempt to narrow the range of possible adsorption structures, the experimental data analysis was conducted on the assumption that the adsorbed molecule and the outermost Pd layer retained a common mirror plane. As such, the off-hollow geometry of Table 4.2 was not considered in the final optimisation of the experimentally-determined structure. In view of the sparse experimental data set, and doubled number of local structural parameters associated with the inequivalent locations of the two α-C atoms in the off-hollow geometry, it is clear that relaxing the constraints of the experimental data analysis would be most unlikely to lead to a unique and reliable distinction of the hollow and off-hollow geometries, or of any significant refinement of the best-fit structure.

Bearing in mind these constraints, the most meaningful comparison of experiment and theory in Table 4.3 are those relating to the location of the α-C atoms relative to the Pd(111) substrate, namely the nearest-neighbour α-C-to-

Table 4.3: Optimised adsorbate–substrate structural parameter values for the hollow-h and off-hollow-h structural models of furan on Pd(111) obtained in this study from the RPBE calculations compared with results of the experimental PhD investigation [100] and of the LDA calculations of Loui [101] for the hollow-h structure. The hollow-f and off-hollow-f geometries have essentially identical parameter values to those of the –h structures. Note that the PhD study only determined directly the location of the α-C atoms on the surface; the values for $d_{\mathrm{Pd}-\beta-\mathrm{C}}$ (bracketed) and $d_{\mathrm{Pd-O}}$ were obtained from the combination of the site of the α-C atoms and the optimised value of the molecular tilt, assuming that the complete furan ring is planar. For the O atom, in particular, the DFT calculations clearly indicate that this assumption is not valid, leading to a large systematic error in the experimental value of $d_{\mathrm{Pd-O}}$ which is therefore shown in double-brackets. The 'oop' (out-of-plane) angles are relative to the plane defined by the four C atoms for the symmetric hollow sites, and defined relative to the nearest C atoms for the distorted off-hollow geometry. α is the tilt angle of the molecular plane defined by the C atom plane away from the surface; for the off-hollow site this plane is distorted so a representative range of values is given. Also included in the table are a few intramolecular structural parameter values taken from Table 4.1 to allow comparison with the values following adsorption.

Parameter	Free molecule {this study}	Experiment [100] {hollow-h}	This study hollow-h	This study off-hollow-h	Loui [101] hollow-h
$d_{\mathrm{Pd}-\alpha-\mathrm{C}}$ (Å)	-	2.13 ± 0.03	2.11	2.10, 2.21	2.07
$d_{\mathrm{Pd}-\beta-\mathrm{C}}$ (Å)	-	(2.34 ± 0.14)	2.23	2.13, 2.25	2.21
$d_{\mathrm{Pd-O}}$ (Å)	-	((2.42 ± 0.08))	2.81	2.80, 2.96	2.77
α-C off-atop (Å)	-	0.59 ± 0.06	0.44	0.50, 0.57	-
β-C off-atop (Å)	-	0.91 ± 0.06	0.97	1.03, 0.83	-
O off-atop (Å)	-	1.41 ± 0.02	1.52	1.45	-
O oop angle (°)	0	0 assumed	21.1	14.7, 16.0	-
H{α-C} oop angle (°)	0	-	54.4	28.5, 58.1	-
H{β-C} oop angle (°)	0	-	21.6	18.7, 37.4	-
d{O:α-C} (Å)	1.36	-	1.40	1.37, 1.41	1.39
d{α-C^n:β-C^n} (Å)	1.35	-	1.44	1.40, 1.46	1.45
d{β-C^1:β-C^2} (Å)	1.42	-	1.41	1.44	1.43
α (°)	-	4 ± 7	0.3	5.4-7.3	-

Pd distance, $d_{\mathrm{Pd}-\alpha-\mathrm{C}}$, and the offset (parallel to the surface) of the α-C atoms relative to this nearest-neighbour Pd atoms, shown in Table 4.3 as 'α-C off-atop'. For these parameters the agreement between the theoretical result for the hollow site and experiment is generally good; particularly good is the agreement in the Pd–C bondlength, the parameter to which the experiment is most sensitive. For the off-hollow geometry, however, the DFT results lead to two different values of $d_{\mathrm{Pd}-\alpha-\mathrm{C}}$: the shorter one (2.10 Å) corresponds to the α-C that bonds to a Pd atom that bonds only to this C atom, whereas the longer bondlength of 2.21 Å corresponds to the α-C that bonds to a Pd neighbour that also bonds to the adjacent β-C atom. Notice, though, that the shorter of these bonds in the DFT calculation is slightly shorter than the experimental value, and the average of these two bondlengths (2.15 Å) is within the estimated precision of the experimental value. Moreover, if one assumes, as indicated by the calculated adsorption energies, that the hollow and off-hollow geometries are co-occupied with equal probability, there are, in total, three short α-C–Pd bonds and just one longer one. The weighted mean of the DFT bondlengths (the quantity measured in the PhD technique in such a situation) is then 2.13 Å, exactly the value obtained in the experiments. The agreement is somewhat less good between experiment and theory for the off-atop displacement, but for this parameter, too, the co-occupation of the off-hollow site is consistent with the experimental results, the off-atop displacement for this geometry being closer to that measured in the experiment.

4.4.4 Comparison to thiophene adsorption

It is interesting to compare the situation for adsorbed furan with the bonding of the closely-related thiophene molecule, C_4H_4S, on transition metal surfaces. Although there appear to be no published DFT (or experimental structure determination) studies of thiophene adsorption on Pd(111), an investigation has been published on Pd(100), also covering Ni(100) and Cu(100) [112]. On Pd(100), at least, a stable molecular chemisorbed state of thiophene exists with the molecular plane essentially parallel to the surface, and the calculations indicate a similar out-of plane displacement of the H atoms. However, the upward shift of the S atom is small and the S–Pd nearest-neighbour distance is small enough (2.32 Å) that one may infer local bond formation. Consistent with this formation of a S–Pd bond is a lengthening of the S–C bonds from 1.71 Å in the gas phase to 1.80 Å on the Pd(100) surface. By comparison, thiophene adsorbs only weakly on Cu(100) and desorbs intact at 150–240 K [92], and the calculations show the

S–C bondlength to be only marginally longer than in the gas phase. On Ni(100) the bonding is even stronger than on Pd(100), and dissociation occurs around 90–100 K [113], but below this temperature range a stable chemisorbed species is found with an even shorter metal–S bond and a longer S–C bond than is found on Pd(100) [112, 114]. These theoretically-computed bondlengths are generally in good agreement with experimental measurements [114–116]. Of course, S is a significantly larger atom than O, so the difference in terms of the interaction of S and O with the underlying substrate may be, at least partially, steric in origin. The rehybridisation of the C bonding in furan pushes the O atom sufficiently far from the surface that the O–Pd interaction must be very small. A similar distortion in thiophene fails to achieve the same large separation of the S atom and the underlying substrate, and the resultant S–metal interaction therefore has an impact on the molecular conformation. The rather modest increase in the O–C nearest-neighbour distance in furan on adsorption of ∼0.04 Å (Table 4.3) is also consistent with the absence of O–metal interaction; this small increase is probably attributable mainly to the influence of the formation of the α-C–Pd bond. As may be expected the increase in the bondlength between the α-C and β-C atoms (∼0.09 Å) is significantly larger.

4.5 Decomposition products

The symmetry constraints of the original Pd(111)-C_3H_3 PhD analysis [102], discussed in section 4.2, were applied in the interests of expediency, to allow a preferred structural model to be identified, rather than because there was prior evidence that such symmetry was a necessary requirement for C_3H_3 adsorption. It is therefore clearly of interest to explore a wider range of possible structures using a method that can distinguish them more effectively. Total energy calculations using DFT offers a means to achieve this, and reported here are the results of such a study. The initial objective was to determine the minimum energy configuration and adsorption site of an isolated C_3H_3 species on Pd(111). However, armed with this model, additional experimental evidence has been confronted. Specifically, the variation in photoelectron binding energy (the core-level shifts - CLS) of the C 1s state in the different C atoms on the surface, comprising coadsorbed C_3H_3 and CO. In the light of the DFT findings, the challenging analysis of the C 1s PhD modulation spectra measured in the earlier study [102] was resumed with new simulations being performed by David A. Duncan at the University of

Warwick in order to establish whether the lowest-energy structures are consistent with the published PhD data [9]. In the context of these results, the possible role of kinetic constraints, and other surface species, in determining the structure of the dissociation products on the surface is discussed.

4.5.1 C_3H_3 structural search

The DFT calculations first focussed on identifying the energetically-preferred molecular conformations and adsorption sites of the C_3H_3 species on the Pd(111) surface at a coverage (1/6 ML corresponding to one molecule per (3×2) unit mesh) that ensured there was very little intermolecular interaction. Five distinct conformers were considered, namely C-CH-CH_2, propargyl (CH-C-CH_2), half-benzene (CH-CH-CH), 1-propynyl (C-C-CH_3), and 'triangle' (a three-membered ring form of CH-CH-CH). In all cases energy-minimisation calculations were started from a range of different starting orientations and lateral registry sites on the Pd(111) surface. As such, several different adsorption sites were found to correspond to local minima in adsorption energy for each molecular conformation. Figure 4.7 illustrates the different conformers and their lowest energy adsorption geometries, together with some less-favoured structures corresponding to local minima for some conformers. The lowest energy (most strongly bound) structure found was the C-CH-CH_2 species with the first C atom located in a fcc hollow site directly above a third layer Pd atom. Relative to a gas-phase C_3H_3 species (the lowest-energy propargyl structure as determined in these gas-phase calculations) the adsorption energy of this species was 2.72 eV. The adsorption energies (per molecule) of all of the structures, relative to this lowest-energy adsorption structure, are also shown in Figure 4.7; positive values indicate the amount by which these molecules were more weakly bound. A general feature of adsorption on fcc (111) surfaces is that there are usually rather small energy differences between adsorption geometries that are equivalent with respect to the outermost substrate layer, but differ with respect to the second (and deeper) layer (as was found for furan on Pd(111) discussed in section 4.4). This geometrical difference is determined by their location relative to the nearest 3-fold coordinated hollow site that is either 'hcp' or 'fcc'. In the case of the C-CH-CH_2 species however, in which the first C atom occupies such a hollow site, the energy difference (as shown in Figure 4.7) has a relatively large value of 69 meV. By contrast, the two lowest-energy propargyl structures which correspond to the CH carbon atoms being closest to fcc and hcp hollows, differ in energy by only 9 meV; for these

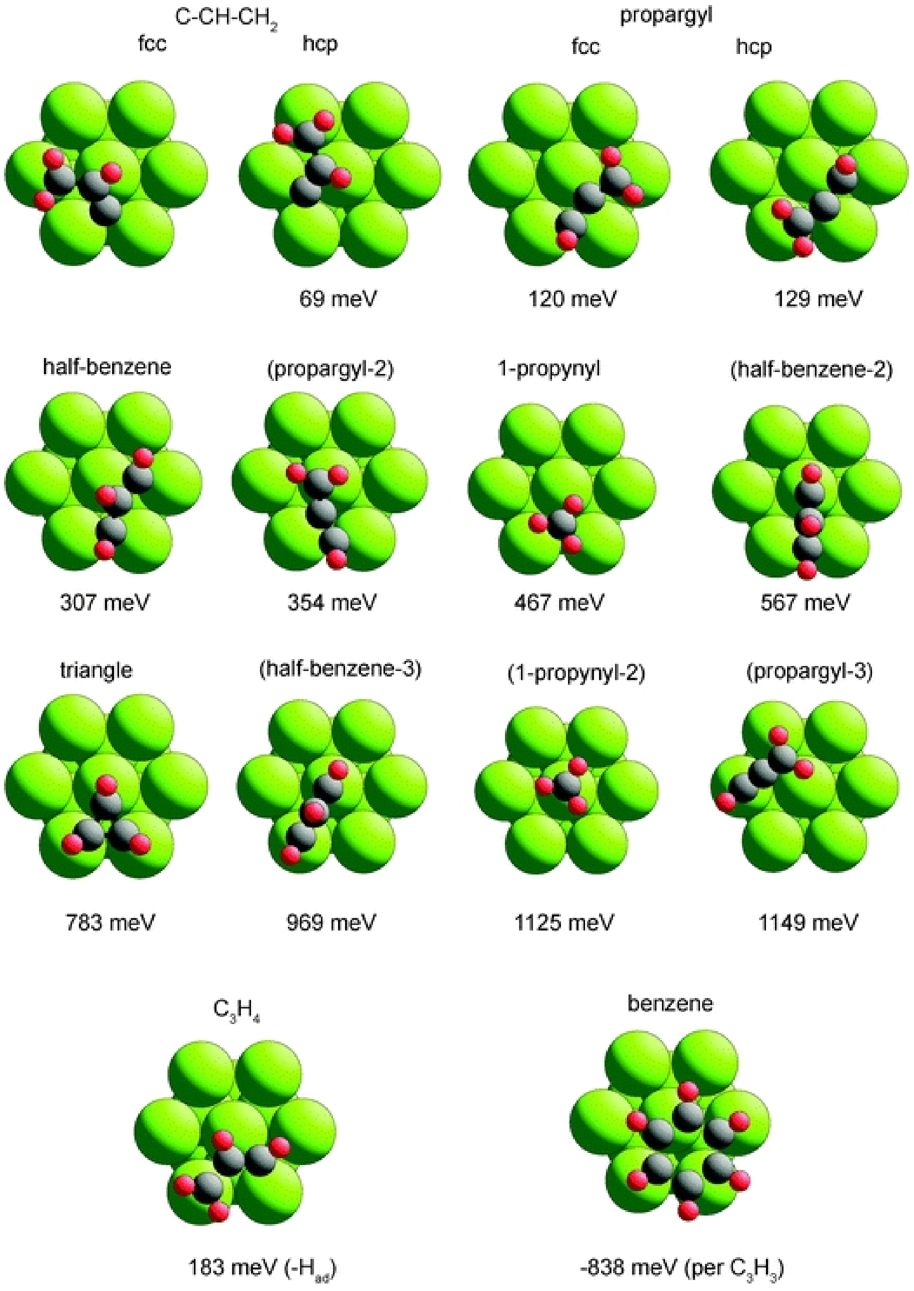

Figure 4.7: Plan view of the Pd(111) surface showing the different optimised molecular configurations and adsorption geometries found in the DFT calculations for C_3H_3, together with those of a C_3H_4 species, and of benzene. In addition to the lowest energy structures for each C_3H_3 conformer, some less-favoured structures corresponding to local energy minima are shown, with their names bracketed.

structures no C atom actually occupies a hollow site with 3-fold coordination. For the less energetically favourable conformers, the fcc/hcp combinations are not included in Figure 4.7, but the associated energy differences are small relative to their energetic disadvantage.

One striking feature of all the lowest energy structures of each conformer (with the exception of 1-propynyl) is that they correspond to all C atoms having four nearest-neighbour bonding atoms, as may be expected for sp^3 bonding character; the same effect was found in the DFT study of intact furan adsorbed on Pd(111), as reported in section 4.4.2. In those structures in which this is not the case, such as the propargyl-3 structure, in which the C atom of the CH species bonds only to one C atom and one Pd atom in addition to the one H atom, there is a huge energy disadvantage of $\sim$1 eV relative to the lowest-energy propargyl structure in which the C atom bridges two Pd atoms in an off-hollow site. Of course, for a propargyl radical, CH≡C-CH$_2$, sp^3 bonding implies substantial rehybridisation.

Also shown in Figure 4.7 are the lowest energy structures for an adsorbed C_3H_4 species (CH-CH-CH$_2$) and for adsorbed molecular benzene, investigated to allow considerations of alternative interpretations of the surface reactions, as discussed later in this chapter. In order to compare the adsorption energy of the C_3H_4 species with that of the C_3H_3 species, the total energy is compared with that of a C_3H_3 species plus an adsorbed H atom. In the case of adsorbed benzene, the total energy per molecule is divided by 2 to compare with the C_3H_3 species. The large negative energy obtained in this way shows clearly that a C_3H_3 coupling reaction of the surface is highly favoured energetically.

4.5.2 Influence of coadsorption

All of the calculations presented in the previous section are for adsorbed C_3H_3 species at sufficiently low coverage that they are effectively isolated on the surface. As such, they take no account of the fact that the molecule is coadsorbed with CO and, perhaps, coadsorbed atomic H. The extent to which these coadsorbates may influence the preferred adsorption geometry of C_3H_3 depends on their spatial distribution and coverage. If the different molecular species separate into distinct homo-molecular domains, there should be no effect from coadsorption. However, if the species are intermixed, the intermolecular distances, and thus the coverage, are an important issue. In the absence of any information regarding the presence or absence of intermixing, the possible consequences of such intermixing needs to be considered. To address this question, initial calculations were conducted of coadsorbed C_3H_3, CO and H (one of each species per unit mesh), and also of coadsorbed C_3H_3 and CO only, in the same (3×2) unit mesh. For each C_3H_3 conformer different relative sites of the three coadsorbates were explored, to identify the lowest energy structures; in all cases the lowest energies were found when CO and H occupied hollow sites, and the C_3H_3 species retained the same local site as that found in the absence of coadsorbates. The effect of the coadsorbates on the local structure of the C_3H_3 species was found to be minimal, with the shortest C-Pd bond lengths changing by no more than ∼0.01-0.02 Å. Changes in the relative C_3H_3 adsorption energies were found to be more significant, however. In particular, the presence of the near-neighbour coadsorbates causes a significant weakening of the adsorption energy. Perhaps unsurprisingly, the effect is largest for the C_3H_3 conformers with the largest 'footprint' on the surface, as these lead to more sites for CO and H adsorption being in close proximity to parts of the C_3H_3 species. This effect disfavours the propargyl species, particularly relative to the 1-propynyl species with an especially small footprint, by more than 300 meV. However, this weakening of the chemisorption bonding is largely removed if the unit mesh size, in which the coadsorbates are located, is increased to (4×2). The implication of this result is that the surface coverage under which the experiments were conducted may be very important in determining the relative adsorption energies of the different C_3H_3 conformers. In this regard it is notable that the PhD data, that provide the only experimental information on the structure of the adsorbed species in this system, were conducted at an estimated coverage of less than 0.1 ML [100]. This is less than the 0.125 ML corresponding to the (4×2) unit mesh used in the lower-coverage coadsorption calculations, strongly suggesting that even if coadsorbed CO and H are intermixed with the adsorbed C_3H_3, their effect on both the adsorption geometry and relative adsorption energy of these species is minimal.

4.5.3 C 1s CLS: theory and experiment

One feature of the photoelectron spectra from the coadsorbed molecular fragments on Pd(111), resulting from furan dissociation, is the presence in the C 1s region of two clearly-resolved components with a relative CLS of approximately 1.7 eV [102]. The peak having the higher binding energy is attributable to emission from CO, that having the lower binding energy is associated with the C_3H_3 species. Measurement of the spectral widths of these two peaks has shown, however, that the peak associated with the hydrocarbon species is significantly wider than that arising from the CO; at a kinetic energy of ∼60 eV the FWHM widths of the hydrocarbon and CO peaks were found to be 1.02 eV and 0.58 eV, respectively [102]. The most probable reason for this is that the C 1s peak from the

Table 4.4: Comparison of the experimental and theoretically-computed values of the C 1s photoelectron binding energy CLS values for the C atoms in the C_3H_3 (or C_3H_4) species adsorbed on Pd(111), relative to that from coadsorbed CO, in the most energetically favoured structures of the various conformers (Figure 4.7)

Structure	CLS values relative to CO (eV)	Mean CLS relative to CO (eV)	CLS range (eV)
C-CH-CH_2 (fcc)	1.45, 1.48, 1.82	1.58	0.37
propargyl2	1.72, 1.38, 1.68	1.59	0.34
half-benzene	1.86, 1.51, 1.86	1.74	0.35
propargyl	1.59, 1.24, 1.48	1.44	0.35
1-propynyl	1.92, 2.86, -0.39	1.46	3.25
triangle	1.66, 1.66, 1.66	1.66	0.00
C_3H_4	1.94, 1.55, 2.05	1.85	0.50
Experiment	-	1.7	~0.5

hydrocarbon species actually comprises two or more components with slightly different, unresolved, CLS values. The different structural solutions of Figure 4.7 show that this is to be expected; with the exception of the triangle conformation, all of the C_3H_3 structures contain C atoms in either two or three inequivalent locations (either within the molecule, or relative to the surface, or both) and so should give rise to two or more different C 1s CLS values.

Calculations of the expected CLS values have therefore been performed using DFT (according to the method outlined in section 3.3.4) to determine whether the difference between calculated CO and C_3H_3 CLS values is consistent with the experimentally-observed splitting, and whether the range of CLS values associated with the inequivalent C atoms in the C_3H_3 species is consistent with the experimental spectral width of this component.

The results of these calculations are summarised in Table 4.4 and compared with the experimental results. Clearly, within the expected precision of such calculations (~0.2 eV), the mean energy separation predicted between the CO and hydrocarbon fragments is consistent with experiment for all the structural models. However, the very large predicted range of energies from the 1-propynyl conformer is not consistent with experiment, so this model can be rejected. In addition it is noted that the triangle model predicts that all the (equivalent) C atoms of the C_3H_3 should have the same CLS, leading to no broadening of the associated spectral line. On this basis alone, however, it is not possible to exclude this model, because the observed broadening in the experiment could also be due to a reduced core-hole lifetime in this species relative to that in the adsorbed CO.

4.5.4 Compatibility with PhD data

As discussed in section 4.2, an extensive C 1s PhD dataset was collected by Knight et. al. [102] from the furan dissociation products on Pd(111) and formed the basis of an initial structure determination of this system. However, the fact that the C_3H_3 contains up to three inequivalent C emitter sites leads to very weak PhD modulations, and also means that the structural parameter space defined by the location of these different constituent atoms is huge. To try to render the structural search more tractable, a set of plausible constraints were therefore applied to the possible solutions in the original PhD analysis. Specifically, C_3H_3 was assumed to have the half-benzene conformation, with the molecule sharing one of the mirror symmetry planes of the outermost Pd(111) layer, forcing the two outer C atoms to occupy sites that are identical relative to this outermost Pd layer. Applying these constraints provided two slightly different structural solutions (see Figure 4.2) that led to rather good agreement between simulated and experimental PhD data, but both solutions corresponded to structures in which the molecular plane was almost parallel to the surface. This orientation is clearly inconsistent with the results of the DFT calculations presented here. DFT structural optimisations using these 'lying-down' configurations as the starting structures led to strong tilting of the molecule, as well as lateral displacements to locations that lack the previously imposed mirror symmetry, with a substantial reduction in the total energy. The lowest-energy half-benzene configuration found in the DFT study (half-benzene - see Figure 4.4) has the molecular plane tilted only 32° from the surface normal, or 58° out of the surface plane. This tilt angle is close to that in the analogue organometallic carbonyl cluster compound [103] referred to in section 4.2 and also shown in Figure 4.2.

Armed with a series of lowest-energy structures obtained by DFT calculations for the different C_3H_3 conformers, however, a new opportunity presented itself to utilise the experimental PhD data. Specifically, one may ask if PhD simulations based on any of the DFT-derived structures provide a good description of the experimental data, and whether the conformer found to have the lowest energy is the one that provides the best description of the PhD data. It is important to consider however that, particularly for molecular adsorbates, experimentally determined adsorption bond lengths, mainly obtained using the PhD technique, can differ by up to ∼0.1 Å from the values obtained in DFT calculations (e.g. the difference in theoretical and experimentally determined bondlengths for alanine on Cu(110) [117]) and a bond length change of this magnitude can have a very significant effect on simulated PhD spectra. It is therefore essential to allow some structural optimisation in the PhD simulations, aimed at improving the agreement between experiment and simulations. A thorough re-analysis of this PhD data was therefore carried out by David A. Duncan at the University of Warwick, the details of which are described in [9]. The numerical results of these PhD simulations are summarised in Table 4.5 for DFT structures that correspond to the lowest-energy solution for each of the conformers investigated. The table shows the R-factor values obtained, and provides a comparison of the C-Pd nearest neighbour bonding distances in the original DFT solution and a modified structure (optimised under constraints) found to give improved agreement with the PhD data. The R-factor is defined such that a value of 0 corresponds to perfect agreement, but for a complex structure, and weak PhD modulations, involving multiple emitter atom geometries, such as the case under investigation here, it sometimes proves difficult to achieve R-factor values less than ~0.4 [118].

Bearing this in mind, it is noted that there are two of the C_3H_3 conformer structures that yield potentially acceptable R-factor values, namely propargyl and half-benzene. The C-CH-CH_2 conformer, that corresponds to the lowest energy structure in the DFT calculations, yields a significantly higher R-factor value of 0.52, strongly suggesting that this is not the structure that occurs in practice. In assessing the compatibility of the DFT and PhD results, it is also important to compare the C-Pd bond lengths, because the PhD optimisation conducted allows these to change significantly from the DFT values, and large changes could mean that the comparison is not of the same conformers. In this context it is noted that PhD is insensitive to the location of the very weakly-scattering H atoms, so while PhD identifies the preferred position of the C atoms, it does not distinguish C atoms in C, CH, CH_2, and CH_3 species. In fact Table 4.5 indicates that the C-Pd bond lengths of the DFT and PhD structures for each conformer are very similar. Perhaps most notable is the C-Pd nearest-neighbour distance of the middle C atom in the half-benzene conformer, with DFT and PhD values of 2.32 Å, and 2.13 Å, respectively. This results in rather different tilt angles of the C-C-C plane relative to the surface normal, namely 32° and 41°, respectively.

Note that the values of the R-factors for the re-optimised DFT C_3H_3 structures listed in Table 4.5 are all significantly larger than the value of 0.23 found in the original PhD analysis for the 'lying-down' half-benzene structures shown in Figure 4.2. The results of the DFT calculations, however, indicate that these structures do not correspond to stable molecule-surface bonding states, despite having reasonable values of the C-C and C-Pd bond lengths. This highlights

Table 4.5: Summary of the results of the simulations of the PhD modulation spectra for the minimum-energy structures identified in the DFT calculations (Figure 4.7). For each structure the table shows the C-Pd nearest-neighbour distances in the exact DFT structure, and in re-optimised structures obtained from the PhD simulations, including the value of the R-factor that provides a measure of the level of agreement between the PhD experimental data and these simulations.

Structure	DFT C-Pd nn distances (Å)	PhD C-Pd nn distances (Å)	PhD R-factor
C-CH-CH_2	2.14 (CH2); 2.27, 2.95 (CH); 1.96, 1.97, 2.05 (C)	2.13; 2.19, 2.98; 1.97, 1.98, 2.02	0.52
propargyl	2.13 (CH2); 2.02, 2.26 (C); 2.04, 2.15 (CH)	2.14; 1.94, 2.29; 2.04, 2.16	0.32
half-benzene	2.01, 2.14; 2.32, 2.89, 3.09; 2.00, 2.12	2.03, 2.10; 2.13, 2.82, 3.05; 1.95, 1.96	0.43
1-propynyl	2.10	2.10	0.76
triangle	2.05	2.12	0.59
C_3H_4	2.11 (CH2); 2.36, 2.76 (CH); 2.01, 2.12, 2.71 (CH)	2.12; 2.43, 2.68; 2.08, 2.08, 2.66	0.23
benzene	2.23, 2.23; 2.20	2.14, 2.11; 2.15	0.47

the fact that, particularly for a complex problem with multiple emitter sites, such as in the present case, it is possible to find structural solutions that give a good description of the PhD data, but do not correspond to physically reasonable solutions. Nevertheless, through a series of calculations involving more reasonable constraints, one plausible structural model was identified that did not correspond to any of the DFT solutions. Consideration of the coordination of the three C atoms to the surface Pd atoms led to the conclusion that this model could be rationalised in terms of a C_3H_4 conformer. DFT calculations for such a species confirmed this conclusion, and yielded a structure quite similar to the model first identified though the PhD structure search. The results for this structure are included in Table 4.5, together with the outcome of a similar procedure for the lowest-energy configuration of the benzene molecule on Pd(111) obtained from additional DFT calculations. Clearly, this C_3H_4 model does yield an R-factor that is lower than any of the C_3H_3 conformers; whether it is reasonable to believe that the hydrocarbon fragment resulting from the furan dissociation could be C_3H_4, rather than C_3H_3, is discussed in section 4.5.6.

4.5.5 Discussion

The objective in undertaking this study (and the objective of the earlier PhD study) was to try to identify the structure of the C_3H_3 species formed on the Pd(111) surface as a result of the partial dissociation of furan. The original studies that characterised the associated surface chemistry led to the suggestion that C_3H_3 may retain the CH-CH-CH half-benzene conformation that arises if one simply removes O-CH from the furan ring. Figure 4.1 shows this simple idea schematically, although it is noted that even this simple scheme requires three bonds within the furan molecule to be broken (as illustrated by the dashed ellipses). Such a process is likely to involve transient intermediates, rather than a single concerted action, but whatever the detailed pathway, the energy released as a result of the fragmentation could allow rearrangement of the C_3H_3 fragments. The fact that there is evidence for some (but probably only a small amount of) benzene formation on the surface, in the temperature range ~330-430 K [96], does suggest that a stable half-benzene conformer may result from the dissociation, because coupling of this conformer to produce benzene seems likely to be more easily effected than for any of the alternative C_3H_3 conformers. On the other hand, the DFT calculations show that there are significant energetic advantages associated with the adsorbed species being in the C-CH-CH_2 or CH-C-CH_2

(propargyl) conformations. Of course, these calculations provide no information on the energy barriers associated with the required relocation of the H atoms, although a shift of one H atom from the central C atom to one end seems less challenging than a shift of a H atom from one end to the other. However, if the H atom is transiently adsorbed on the surface, both mechanisms seem plausible.

The results of the new PhD simulations discussed in the previous section provide rather strong evidence that the lowest-energy structure for a C_3H_3 species adsorbed on Pd(111), as determined by the DFT calculations, namely C-CH-CH_2, is not present in significant amounts on the surface following dissociation. Much the most likely reason for this is that, when the C_3H_3 fragment is created by the partial dissociation of furan, there is too large an energy barrier for the fragment to reconfigure to form this C-CH-CH_2 conformer. Based on a combination of the DFT energies, and R-factors found in the PhD simulations, the most likely surface species is the propargyl conformer, although at least some fractional coverage of the half-benzene configuration cannot be excluded.

4.5.6 Plausibility of other species

While this discussion has focussed on the possible conformations and bonding sites of a surface C_3H_3 species, there are two alternative surface species that may be considered, namely C_3H_4 and benzene. Removing CO from furan leaves 3 C atoms and 4 H atoms, so from the point of view of stoichiometry a C_3H_4 species is clearly reasonable. The local structure of the C_3H_4 species found in the DFT calculations evidently leads to a particularly favourable set of PhD modulation spectra, and the adsorption energy is only slightly larger than that of the propargyl C_3H_3 species coadsorbed with atomic H. The alternative possibility of benzene on the surface due to coupling of two C_3H_3 species is, on the basis of the equilibrium total energy alone, strongly favoured. On the other hand, the energy barrier to its formation by C_3H_3 coupling is not known, and the quality of agreement of the PhD simulations for this structure with the experimental data is rather marginal.

Key data relevant to the plausibility of the hydrocarbon intermediate in furan dissociation being C_3H_4, rather than C_3H_3, are the previously-published thermal desorption spectra. Molecular hydrogen is desorbed from the surface in a TPD experiment at a peak temperature of 350-360 K, so above this temperature it is clear that the average stoichiometry of the residual C_3H_x fragment after CO extraction from furan must have a value of $x < 4$. This does not exclude the possibility that some partial coverage of C_3H_4 is present on the surface even above this temperature range, but if only a single hydrocarbon fragment remains it must have $x \leq 3$. The PhD experiments were performed on samples that had been heated to 340 K, but as the time at, or close to, this temperature would have been several minutes, one may expect that essentially all the available hydrogen would be desorbed. Some error in the exact sample temperature cannot be excluded, so it is possible that the PhD data were taken under conditions that did not lead to hydrogen desorption. However, the fact the that hydrogen desorption temperature is the same as, or very close to, that seen for hydrogen desorption from a Pd(111) surface that has only adsorbed atomic hydrogen, has been taken to imply that the rate limiting step in hydrogen desorption following furan decomposition is associative desorption of adsorbed atomic hydrogen, and not molecular dissociation. If this is the case, the initial furan dissociation at the lower temperature of ~230-270 K (as seen in spectroscopic data) must lead to coadsorption of atomic H and a C_3H_x fragment with a value of $x < 4$. On the other hand, if the close similarity of the H_2 desorption temperature of the hydrogen-dosed and furan-dosed samples is regarded as coincidence, it is then possible that its origin in the case of furan decomposition is loss of hydrogen from a C_3H_4 species to C_3H_x with $x \leq 3$. However, in view of the need for both a fortuitous coincidence in these temperatures, and a significant mis-calibration of the thermocouple in the PhD study, it seems rather unlikely that the surface species studied was C_3H_4.

Rather different arguments lead to the conclusion that it also unlikely that the surface species investigated in the PhD study was benzene. The one piece of evidence that surface benzene may result from furan decomposition on Pd(111) is the LITD experiments, which showed small amounts of benzene desorption from the surface during heating in the temperature range ~330-430 K. The desorbed yield of benzene in these experiments was very low, suggesting that surface benzene that is formed in this temperature range is a minority species, although the report of this work does suggest that the LITD cross-section for benzene desorption may be low. It is notable, though, that ultra-violet photoemission spectra recorded in this temperature range [94] do not show peaks at the characteristic energies of the molecular orbitals of adsorbed benzene (e.g. ref. [119]). Also absent in this temperature range are the γCH vibrational bands of the benzene ring in HREELS around 800 cm-1 [94], that are dominant in spectra recorded from benzene adsorbed on Pd(111) [120]. This seems to be a clear basis for excluding adsorbed benzene as a major surface species in the PhD experiments.

4.6 Conclusions

In summary, the results of the DFT calculations presented in section 4.4 show a rather clear picture of the local bonding and geometry of furan on Pd(111). The preference for hollow-site occupation is consistent with the results of the earlier theoretical calculations of Loui, but the identification of two slightly different hollow and off-hollow geometries that differ in terms of which pair of adjacent C atoms bond to a single Pd surface atom is new. The almost identical adsorption energy of these two structures is slightly surprising, but the nature of the bonding is so similar that one would certainly expect their energetic difference to be small. These minimum energy structures resolve the ambiguity of the experimental PhD investigation regarding the structure, and are clearly consistent with the key findings of these experiments.

For the C_3H_3 decomposition product of furan on Pd(111) the situation is less clear. On the basis of the DFT energies and the PhD R-factors, the most probable structural outcome of this reaction is coadsorbed CO (in hollow sites, as previously established by PhD [102]) atomic H (also found by the present DFT calculations to occupy hollow sites) and C_3H_3 in the propargyl conformation, straddling a bridging site as shown in Figure 4.7. On the same basis, the next most probable form of C_3H_3 is the half-benzene conformer, with the two end C atoms in local bridging sites (Figure 4.7) with the molecular plane tilted by $\sim 35°$ from the surface normal. The fact that this conformer leads to significantly poorer agreement between theory and experiment for the PhD data, as well as being energetically disfavoured by ~ 180 meV per molecule, does suggest that this is not the sole or dominant conformer on the surface, but partial co-occupation of this species could help to account for the partial production of surface benzene indicated by the LITD data.

Further experiments and theoretical studies could provide a more complete resolution of this problem. Experimentally, new higher-resolution vibrational spectroscopy could provide a clearer spectroscopic fingerprint of the adsorbed species, though the clearest such information would come from single-molecule vibrational spectroscopy using an STM tip [121]. Theoretically, a better understanding could be achieved through calculations of the pathways and energy barriers to the formation of the different C_3H_3 conformers on the Pd(111) surface following furan decomposition.

Chapter 5

Long-range ordered adsorbate structures on Cu(110)

Presented in this chapter are the results of two DFT studies of overlayers formed by organic molecules on Cu(110), namely methoxy and cytosine. In both cases the theoretical calculations have been conducted to complement the analysis of experimental data from PhD.

5.1 (5x2) methoxy reconstruction

5.1.1 Introduction

A key objective of many modern surface-science studies of well-characterised surfaces in ultra-high vacuum has been to gain an understanding of the fundamental processes in heterogeneous catalysis. In this regard, one of the most-studied systems is the oxidation of methanol to formaldehyde over Cu(110). Initial (and later) characterisation of the reaction was performed by temperature-programmed reaction spectroscopy [122–126] and direct measurements of the reaction turnover [127], while a range of electronic [123, 127–129], and vibrational spectroscopies [128–130] provided direct identification of the surface reaction intermediates. A general consensus in this work is that the key molecular surface intermediate in this reaction is the deprotonated methanol or methoxy species (CH_3O-), the deprotonation being effected by surface oxygen, while further reaction produces formaldehyde (CH_2O) and hydrogen. The generally accepted scheme is:

$$\begin{aligned}
CH_3OH(a) + O(a) &\rightarrow CH_3O(a) + OH(a) \\
CH_3OH(a) + OH(a) &\rightarrow CH_3O(a) + H_2O(g) \\
CH_3O(a) &\rightarrow CH_2O(g) + H(a) \\
2H(a) &\rightarrow H_2(g)
\end{aligned}$$

The alternative combustion reaction (producing CO_2 and H_2O) occurs via the formate (HCOO) surface intermediate which can be created from interaction of the methoxy species with excess surface oxygen.

A series of STM investigations have cast light on the local character of the interaction of methanol with adsorbed O atoms in the O-Cu-O added rows associated with the initial local (2×1)-O 'added row' structure on this surface, despite some controversies in image interpretation [131–140]. Notice that the reaction scheme outlined above implies that each O atom on the surface can, through exposure to methanol, lead to two surface methoxy species. An XPS study of the surface reaction at room temperature, however, led to the conclusion that although this stoichiometry is observed on Cu(111), on the (110) surface the stoichiometry is only 1:1, rather than 2:1 [129]. Specifically, although the O 1s emission peak observed from the surface shifts in energy with increasing methanol exposure (the atomic oxygen being consumed and surface methoxy species being created), the area of this peak remained unchanged. It was suggested that this may be due to loss of half of the surface methoxy as it is created, perhaps through formaldehyde desorption, despite the temperature being lower than that at which the steady-state catalytic reaction can proceed.

5.1.2 Previous structural work

Somewhat surprisingly, in view of the many experimental investigations of this system, together with a number of theoretical studies seeking to elucidate the detailed reaction mechanism [141–143], there had been no experimental determination of the adsorption site of the important methoxy species on Cu(110) prior to this work. The only previous attempt to obtain some quantitative structural information was an early investigation of the tilt of the intramolecular O-C axis using high-energy forward-scattering XPD [144, 145]. This led to results indicating two distinct species, one tilted by 18 ± 3° in the $[1\bar{1}0]$ azimuth, the other tilted by 40 ± 5° in the [001] azimuth. This was suggested to imply that two distinct adsorption sites are co-occupied, possibly with low symmetry (specifically off-long-bridge and three-fold-coordinated hollows - see Figure 5.1) to account for the two tilt angles. In addition, some important experimental structural information comes from a STM study, complemented by recording qualitative LEED patterns; both techniques identified a (5×2) ordered structural phase of methoxy, while the LEED pattern showed systematic beam absences characteristic of pg or pmg space groups [131]. A later STM study presented line-scan data that led to the conclusion that no mirror symmetry was present, and thus the space group could only be pg [137]. Additional evidence comes from STM results [132] which indicate that most of the adatoms are incorporated into the (5×2)pg structure from the original (2×1)-O surface reconstruction; Cu adatoms do not diffuse to surface steps. Based on the XPD results, and the identification of the surface periodicity and space group, together with an estimation of the number of Cu adatoms incorporated into the structure from the original (2×1)-O surface reconstruction, a number of structural models of the ordered phase were proposed [132]; each of these included co-occupation of several different local methoxy adsorption sites. These complex models of the (5×2) structure have also been investigated using DFT calculations [142], leading to the identification of a lowest-energy structure with methoxy species occupying long-bridge sites and two different lower-symmetry sites.

In contrast to the implication of these experimental studies that the structure of methoxy on Cu(110) is complex, with co-occupation of multiple sites, a number of theoretical (DFT) studies [141–143], aimed at understanding the surface reaction mechanisms, conclude that the reaction involves only methoxy species adsorbed at short bridge sites on an unreconstructed surface. While several such studies all identify this adsorption geometry as the energetically-favoured one, such calculations generally fail to consider the possible role of Cu adatoms present in the (2 ×1)-O surface with which the methanol reacts.

Complementing the present work, a PhD investigation of the local methoxy site has been conducted by Dagmar Kreikemeyer Lorenzo at the Fritz-Haber-Institut der Max-Planck-Gesellschaft, Berlin [11]. Five locally-symmetric adsorption sites on an unreconstructed Cu(110) surface were trialled against the data, namely short bridge, long bridge (midway between nearest-neighbour Cu atoms in the [001] azimuth), atop, the most-symmetric (so-called '4-fold') hollow (atop a second layer Cu atom) and the 3-fold coordinated hollow in the side of the atomic 'troughs' (see Figure 5.1). In PhD investigations, the quality of the fit of a model to experimental data is typically provided by an R-factor (R) which is defined such that R = 0 is perfect agreement and R = 1 implies no correlation. After allowing both the O atom and outermost layer Cu atoms to relax perpendicularly to the surface, it was concluded that the short bridge site gave much the best

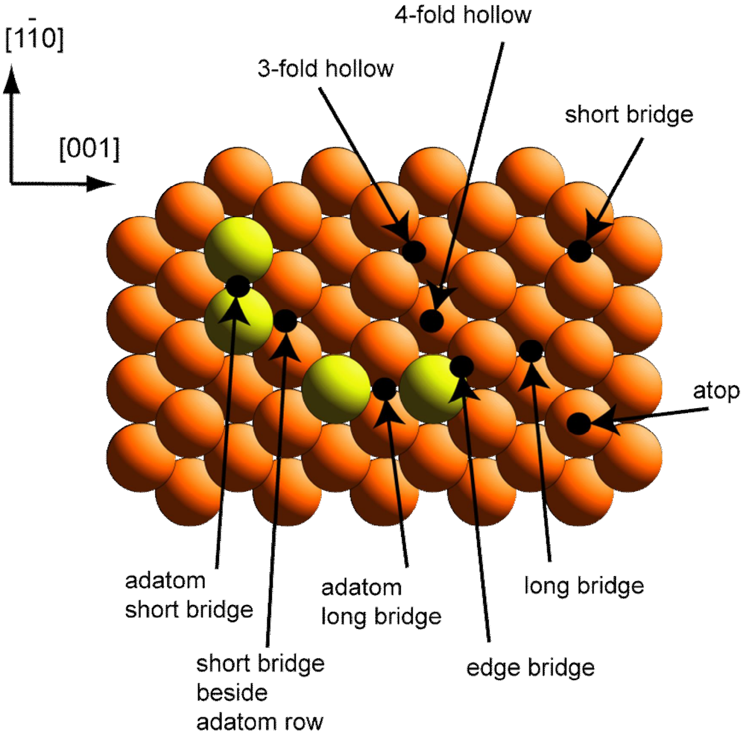

Figure 5.1: Plan view of a Cu(110) surface showing the two principal azimuths and the location of the principal adsorption sites. Four Cu adatoms are shown in a different (yellow) shading for clarity. Note that the '4-fold hollow' is a very open site such that it would only involve 4-fold coordination for an adsorbate with a large Cu-adsorbate bondlength. Adsorbates with shorter adsorption bondlengths in this site would actually be singly-coordinated to the second-layer Cu atom below.

fit to the data with R = 0.24. A further conclusion of this study was that the 3-fold hollow site, which has been favoured in some earlier discussion of possible adsorption geometries for this adsorption system, cannot be the single occupied site and is most unlikely to have significant fractional occupation in any possible multi-site solution. It was discovered, however, that an improved fit (R = 0.15) could be found for a model based on co-occupation of two slightly different short-bridge sites, on and beside an extended Cu adatom row, with slightly different heights of the O atoms above the short-bridging Cu atoms of 1.47 Å and 1.49 Å, respectively, albeit with an unreasonably short Cu-O distance.

5.1.3 Computational details and clean surface reconstructions

In order to gain a better understanding of the structure of methoxy on Cu(110) the information acquired using the PhD technique has been complemented by the new DFT calculations reported here. The RPBE exchange-correlation functional [73] was used throughout, with ultrasoft pseudopotentials (see section 3.2.4). Initial calculations of the different local adsorption sites used five-layer slabs to represent the Cu(110) substrate, with the positions of Cu atoms in the top three substrate layers, as well as in any Cu adatom layers, being allowed to relax. In later refinements of the optimum structures the calculations used seven-layer slabs to represent the substrate, with the outermost five layers allowed to relax. However, these calculations using the larger supercell led to molecular and atomic adsorption energies that were almost identical; for consistency therefore the discussion in the text considers the values obtained from the five-layer slab calculations only, but a comparison of the values from the two sets of calculations is provided in tabular form. All other computational parameters were determined according to considerations of chapter 3.

The initial tests focussed on establishing the relative adsorption energies in different single adsorption sites in the absence of any significant intermolecular interactions; for this purpose a (2×2) unit mesh, containing one methoxy species (thus corresponding to a coverage of 0.25 ML), was used. For an unreconstructed surface the five-layer supercell in these calculations contained a total of 25 atoms (20 Cu, 1 O, 1 C, 3 H). Calculations were also performed on (2×2) models including 2 Cu adatoms (0.5 ML coverage), either as [001] or $[1\bar{1}0]$ added rows, or in a c(2×2) 'chequer-board' arrangement (occupying alternate bulk-continuation sites); in each case this increased the number of atoms per supercell to 27. (In the seven-layer slabs the supercells without, and with, Cu adatoms contained 33 and 35 atoms, respectively). The same (2×2) supercell was also used to explore the effect of a higher (0.5 ML) adsorbate coverage by incorporating two adsorbed methoxy radicals onto an unreconstructed surface. All calculations were performed without symmetry constraints, allowing the O-C axis of the methoxy species to tilt relative to the surface normal, with different azimuthal orientations of the methyl species (and thus of the C-H bonds) being explored to identify the lowest energy structures.

In order to compare the relative energies of structures with and without adatom reconstructions, it is necessary to take account of the different number of

Cu atoms within the supercell for reconstructed and non-reconstructed surfaces. For this purpose, in preference to reporting surface energies (equation 3.37), a second adsorption energy, $E_a{}'$ is introduced which can more easily be compared to E_a (equation 3.35). As an example, one may consider the case of adsorption in a (2×2) supercell containing a single added row of Cu atoms (i.e. 2 Cu adatoms). In this case, $E_a{}' = E_a + E$(Cu(110)non-recon) - (E(Cu(110) + added row) - $2E_b$(Cu)) where the choice of Cu adatom reservoir is bulk crystalline Cu. This takes account of the fact that, in general, the energy associated with an adatom is greater than the energy associated with the same atom in the bulk, so $E_{\mathrm{a}}{}'$ is expected to be smaller than E_{a}. Of course, there is little chemical significance in an absolute adsorption energy defined relative to a gas-phase methoxy radical, but the relative values do provide an appropriate basis for comparing the relative stability of the different possible adsorption structures.

For the clean (2×2) surface calculations, the magnitude of the corrections associated with the Cu adatom structures proves quite revealing. For the [$1\bar{1}0$] added-row model, the energy cost is only 100 meV per (2×2) unit mesh (and thus 50 meV per Cu adatom). By contrast, for the [001] added-row model this energy cost is 600 meV per (2×2) unit mesh, while for the c(2×2) chequer board adatom model the equivalent value is 710 meV. The implication that the energies of an unreconstructed Cu(110) surface, and of a (1×2) added row reconstruction of this surface, are closely similar, is not unreasonable; such a reconstruction does occur on some clean fcc metal (110) surfaces (including Au(110) [146]), and indeed Cu(110) itself does reconstruct in this way in the presence of adsorbed alkali metals (e.g. [147]). One other conclusion that might be drawn from this result is that adatom structures that involve atoms in local [$1\bar{1}0$] rows are likely to be energetically favoured over those involving different arrangements of the adatoms.

5.1.4 Single-site calculations

Table 5.1 shows the adsorption energy per methoxy species for adsorbed methoxy in a range of geometry-optimised adsorption sites, and also lists the O-Cu nearest-neighbour bondlengths and interlayer spacings. On the unreconstructed surface the short-bridge site is clearly energetically favoured at coverages of both 0.25 ML and 0.50 ML, with slightly stronger bonding (by 50 meV per methoxy species) at the higher coverage. The favoured geometry at both coverages has the O-C bond tilted by ∼35° in the [001] azimuth. The energetic preference for the short-bridge site on the unreconstructed surface, the small advantage at the higher coverage, and the tilt angle, are all consistent with the results of previous DFT studies of this system [141–143].

Of the other adsorption sites on the unreconstructed surface, it is notable that the long-bridge site is not only less favourable by almost 0.5 eV, but also that the optimal geometry places the O atom 1.22 Å above the outermost layer. By contrast, the long-bridge site that gave a modest fit to the PhD data [11] corresponded to a much smaller spacing (0.2 Å) above the outermost layer; this structure can evidently be discounted on energetic grounds, consistent with the earlier assertion that this leads to a Cu-O distance that is unreasonably short. Indeed, the only way one might have rationalised this low-lying long-bridge geometry would be to assume that the near-neighbour long-bridge atoms move further apart with the insertion of the methoxy O atom. However, the DFT calculations reveal that for adsorption in the long-bridge site, these nearest-neighbour Cu atoms actually move closer together, causing the methoxy to move higher above the surface for any specific value of the Cu-O bondlength.

On the chequer-board and [001]-added row adatom-reconstructed surfaces, the adsorption energies in all sites, even before taking account of the relative large energy cost of these reconstructions, are very substantially smaller than that of the short-bridge site on the unreconstructed surface. The particularly weak adsorption energies found on the chequer-board reconstruction reinforces the idea that structural models involving isolated adatoms are strongly disfavoured. Occupation of the short-bridge site on added $[1\bar{1}0]$ rows, by contrast, is very favourable. The adsorption energy of the methoxy species on such a surface is actually 80 meV higher (i.e. more strongly bonded) than on the unreconstructed surface, even after taking account of the energy cost of the reconstruction. This is thus the lowest energy structure of all the models explored and reported in Table 5.1.

Evidently the main conclusion of these calculations is that methoxy adsorption at short-bridge sites is strongly favoured, both on the unreconstructed surface, and on the $[1\bar{1}0]$ adatom rows of a (1×2) added-row structure (see Figure 5.2). This result is entirely consistent with the primary conclusion of the experimental PhD study [11].

Table 5.1: Summary of the results for the optimised structures found in DFT calculations for different adsorption sites (see Figure 5.1) and reconstruction models of methoxy adsorbed on Cu(110) in a (2×2) unit mesh using five-layer slabs to represent the substrate. E_a is the calculated adsorption energy per methoxy species, relative to the energy of a gas-phase methoxy species and the energy of the bare metal surface including any relevant reconstruction. $E_a{}'$ is the adsorption energy taking account of the energy cost of the Cu adatom surface reconstruction, where relevant. $z_{\text{O-Cu}}$ and $d_{\text{O-Cu}}$ are the O-Cu nearest-neighbour interlayer spacing and interatomic distance. For adsorption in the 3-fold coordinated hollow sites, and in the edge bridge site on the chequer-board-reconstructed surface, separate values are given for distances to the outermost- and second-layer Cu atoms.

Model	Coverage (ML)	E_a (eV)	$E_a{}'$ (eV)	$z_{\text{O-Cu}}$ (Å)	$d_{\text{O-Cu}}$ (Å)
Short-bridge	0.25	2.08	2.08	1.47	1.97
Long-bridge	0.25	1.69	1.69	1.22	2.05
[1$\bar{1}$0] added-row short-bridge	0.25	2.26	2.16	1.45	1.97
[1$\bar{1}$0] added-row 3-fold hollow	0.25	1.74	1.64	0.51/1.69 1st/2nd	2.04/2.14 1st/2nd
[001] added-row long-bridge	0.25	1.74	1.13	1.13	2.03
Chequer-board off-atop adatom	0.25	1.88	1.17	1.48	1.83
Chequer-board 3-fold hollow	0.25	1.96	1.25	0.67/1.77 1st/2nd	1.93/2.21 1st/2nd
Chequer-board edge-bridge	0.25	1.98	1.27	1.04/1.99 1st/2nd	1.92/2.13 1st/2nd
Short-bridge	0.5	2.13	2.13	1.47	1.97

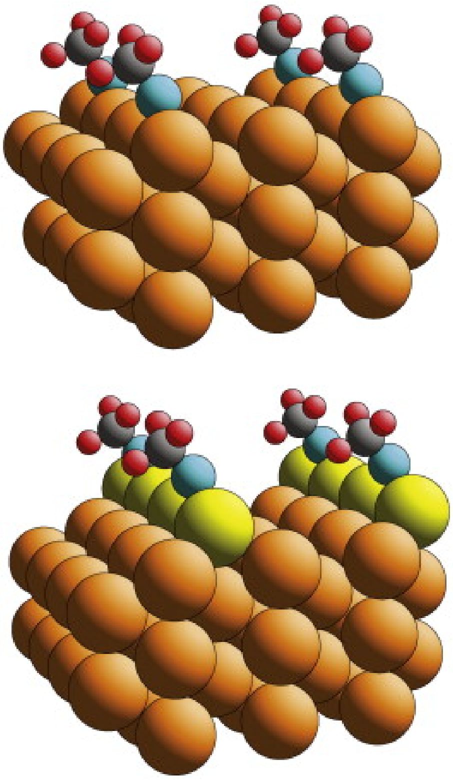

Figure 5.2: The two lowest-energy optimised (2×2) 0.25 ML structures of methoxy on Cu(110) obtained in the DFT calculations. The upper schematic diagram shows methoxy in the short bridge sites on an unreconstructed surface, whereas in the lower diagram adsorption is in similar sites on $[1\bar{1}0]$-added-rows of Cu adatoms.

5.1.5 The Cu(110) (5×2)pg-methoxy structure

So far, the possibility of coadsorption of two different sites, as suggested in several previous experimental studies, has not been addressed, nor the related issue of the structure of the ordered (5×2) phase that has been reported in LEED and STM experiments [132]. Notice that although the long-range order of the surface investigated experimentally by PhD [11] was not known, it is known that methoxy can form this ordered (5×2) phase on Cu(110), and even if the surface was not well-ordered, the main local structural ingredients were likely to be closely similar to those of the ordered phase.

5.1.5.1 Long range structural information

The reported LEED pattern of the (5×2) phase showed certain diffracted beams to be missing at normal incidence [131], characteristic of the presence of glide

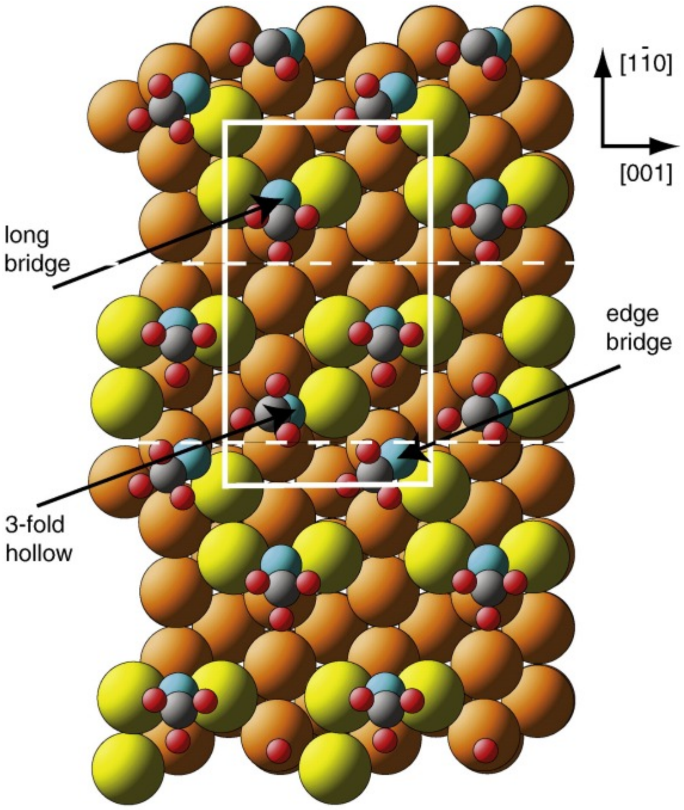

Figure 5.3: Plan view of the structure of the Cu(110) (5×2)-methoxy adsorption structure proposed on the basis of earlier DFT calculations [142]. The white rectangle shows the (5×2) unit mesh. The Cu adatoms and substrate in this structure, but not all atoms in the methoxy adsorbates, show the glide symmetry of the pg space group; the white dashed lines show the locations of these glide symmetry lines.

symmetry lines in the [001] direction [148]; this implies that the space group of this ordered phase is either pg or 2 mg, and a later STM study narrowed this down to pg [137]. One further important result obtained from STM [131] is that islands of (2×1)-O, surrounded by the ordered (5×2)-methoxy phase, could be eroded and converted into the (5×2)-methoxy phase by further exposure to methanol, without the creation of large defect regions or of adatom islands. This strongly suggests that most or all of the 0.5 ML of Cu adatoms in the (2×1)-O phase are retained in the (5×2)-methoxy structure. Indeed, through the use of experiments to monitor by STM step movements resulting from desorption or dissociation of methoxy from the surface, Leibsle et al. [132] estimated the Cu adatom coverage in the (5×2)-methoxy phase to be not less than 0.4 ML. A coverage of 0.5 ML of adatoms would imply 5 such Cu atoms per (5×2) unit mesh, but an odd number is incompatible with the glide symmetry. As a result, Leibsle et al. [132] proposed several possible structures that incorporated either 6 or 4 Cu adatoms in each unit mesh. All these models assume 4 methoxy species per unit mesh (symmetry similarly dictates that there must be an even number). More recently, Sakong and Gross [142] have investigated these proposed structures, involving several different local methoxy adsorption sites, using DFT calculations; they concluded that the lowest-energy structure is that shown in Figure 5.3. This is a slight modification of one of the structures originally proposed by Leibsle et al. in which the methoxy species occupy long-bridge sites on pairs of adatoms, and three-fold hollow sites in which bonding is to both one Cu adatom and two Cu atoms in the underlying surface. The DFT-optimised structure shown in Figure 5.3 differs from this initial proposal in that half of the methoxy species that originally occupied 3-fold hollow sites have moved to two-fold coordinated edge-bridge sites. Notice that the shift of some molecules from the 3-fold hollow to edge bridge sites formally breaks the glide-line symmetry, as does the tilting of some of the molecules. However, it is certainly possible that the associated LEED pattern would still show very weak intensities in the otherwise symmetry-forbidden diffracted beams, because the arrangement of the more strongly-scattering Cu adatoms does retain the required symmetry. Sakong and Gross reported that the average adsorption energy per methoxy species in this structure was only 40 meV lower than in the short-bridge site on a non-reconstructed Cu(110) surface.

5.1.5.2 DFT results

A PhD simulation based on the (5×2) structure proposed by Sakong and Gross [142] failed to achieve a R-factor value lower than 0.97 [11], even after searching for minor changes to minimise this value. Nevertheless, as a starting point to the DFT investigation of the (5×2) phase, a geometric optimisation of this structure was conducted. Figure 5.3 shows the exact geometry obtained from these calculations. The average adsorption energy per methoxy species calculated for this structure, including the energy cost of the Cu adatom structure, is 1.69 eV (see also Table 5.2), a value that is 0.39 eV smaller than for methoxy adsorbed in short-bridge sites on the non-reconstructed Cu(110) surface. This contrasts with an energy difference quoted by Sakong and Gross for the same two structures of only 40 meV. It seems likely, however, that these authors did not include the

Table 5.2: Comparison of the results for the optimised structures found in DFT calculations for different adsorption sites and reconstruction models of methoxy adsorbed on Cu(110) in the (2×2) and (5×2) unit meshes using both five-layer and seven-layer slabs to represent the substrate. E_a and E_a' are as defined in section 5.1.3 and in the caption to Table 5.1.

	5-layer substrate slab		7-layer substrate slab	
Model	E_a (eV)	E_a' (eV)	E_a (eV)	E_a' (eV)
Short bridge (0.25 ML - (2×2))	2.08	2.08	2.11	2.11
Short bridge (0.50 ML - c(2×2))	2.13	2.13	2.15	2.15
[1$\bar{1}$0] added-row short bridge	2.26	2.16	2.25	2.16
(5×2) - mixed sites	2.02	1.69	2.02	1.69
(5×2) - new model (Figure 5.4a)	2.15	1.98	2.16	1.99

energy cost of the Cu adatom structure; without this correction, the average adsorption energy in the present calculations is 2.02 eV, a value that is only 60 meV per methoxy species less than that of the unreconstructed short-bridge geometry. Nevertheless, the key conclusion is that the energy cost of the Cu adatom distribution in this structure is such that this (5×2) structure is clearly energetically unfavourable.

In view of both the incompatibility of this model of the (5×2) phase with the experimental PhD results [11], and the energetic considerations, alternative models have been explored that are based on occupation of short-bridge sites only, but involve half of the methoxy species occupying sites above sections of [1$\bar{1}$0] adatoms rows. As in the originally-proposed models of Leibsle et al., a coverage of 4 methoxy species per unit mesh has been assumed, and either 4 or 6 Cu adatoms. The geometrically-optimised versions of the two proposed structures of this type that have been considered are shown in Figure 5.4. Both structures are fully consistent with the pg space group, and are energetically very significantly more favourable than the structure of Figure 5.3. For the model incorporating 4 Cu adatoms per unit mesh (see Figure 5.4(a)), the average adsorption energy of the methoxy species on the reconstructed surface is 2.15 eV, a value that falls to 1.98 eV after taking account of the energy cost of the Cu adatom distribution. For the model incorporating 6 Cu adatoms per unit mesh (see Figure 5.4(b)), the reconstruction-adjusted average adsorption energy, E_a', is 110 meV lower; the focus of the remainder of the discussion is therefore on the former model.

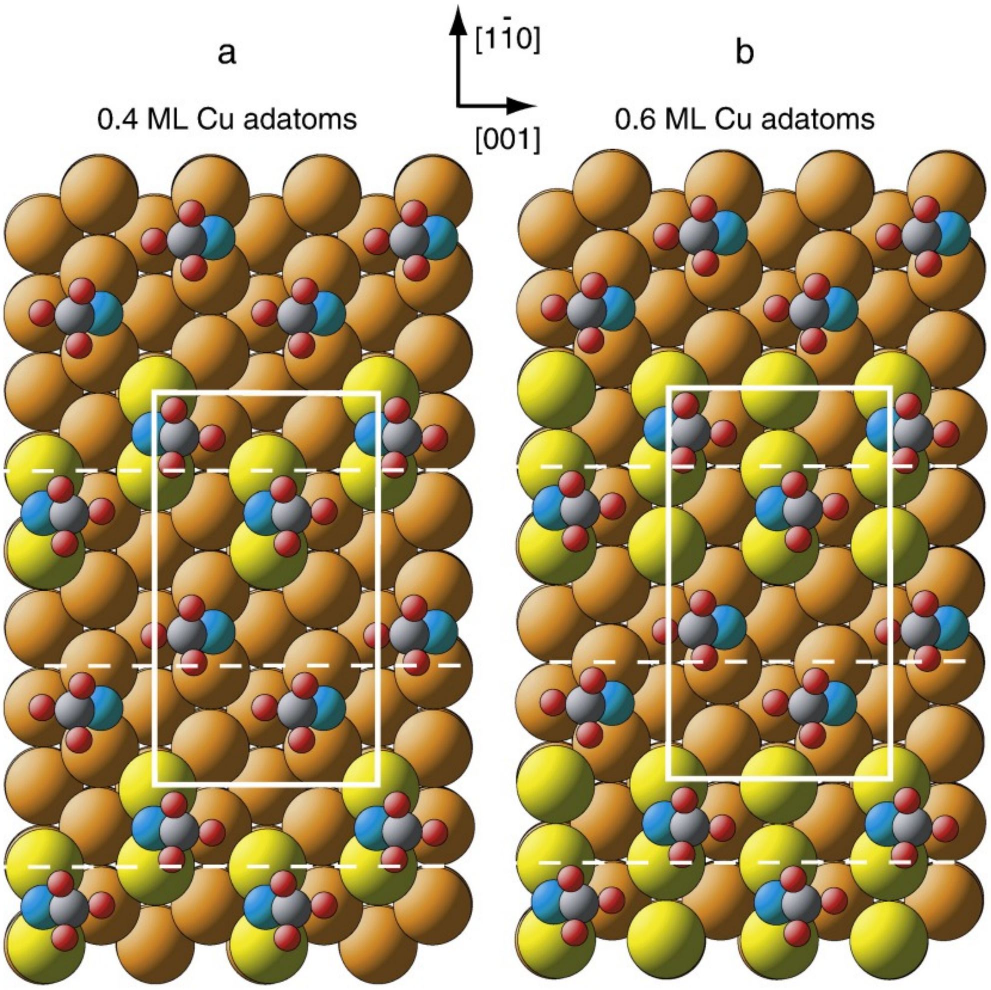

Figure 5.4: Plan view of the two mixed-short-bridge models of the Cu(110) (5×2)-methoxy adsorption structure proposed here on the basis of the new DFT calculations. The white rectangle shows the (5×2) unit mesh. The dashed white lines show the glide symmetry lines of the pg space group.

5.1.6 Compatibility with experimental data

The results presented demonstrate a clear consistency of the main findings of the PhD and DFT investigations in that both sets of results clearly favour occupation of the methoxy species only in local short-bridge sites. Moreover, a specific energetically-favoured adatom model has been proposed of the ordered (5×2) phase based on substrate and adatom short-bridge sites, which has the pg space group consistent with previously-reported LEED beam extinctions. One may therefore ask if this proposed structure is consistent with the recent PhD investigation as well as the previously-published experimental results that provide explicit structural information, namely from X-ray photoelectron diffraction (XPD) and STM.

5.1.6.1 STM images

Figure 5.5 shows a comparison of a simulated STM image of the (5×2) phase, obtained from the preferred DFT structure and based on the Tersoff-Hamann description of STM (see section 3.3.5), with an experimentally-obtained image [149]. Clearly the simulation reproduces the key features of the experimental images, notably the ‘zig-zag’ row of bright protrusions (arising from the methoxy species on the Cu adatoms) and the intervening zig-zag row of weaker protrusions. Another piece of information that can sometimes be extracted from STM images is the registry of the imaged adsorbate-related protrusions with the underlying substrate. This is possible if STM images can be obtained that contain both regions of the unknown structure and other regions of a known structure and imaging properties (ideally, regions of clean surface). In the case of the STM studies of methoxy on Cu(110), many of the images obtained show coexisting regions of the (2×1)-O phase, a rather well-known structure, although it is known that different tip conditions can lead to the protrusions seen in STM corresponding either to the adsorbed O atoms or to the intermediate Cu atoms in the [001] Cu-O-Cu-O added rows. However, there is evidence [132] that in the published images the tip condition is such as to favour imaging of the Cu adatoms in these rows.

Figure 5.6 shows a larger-area schematic of the short-bridge adatom (5×2) structure derived from the current DFT calculations (see Figure 5.4(a)), one area of which shows the (2×1)-O added-row structure instead of the (5×2)-methoxy phase. Lines superimposed on the image in both the [1$\bar{1}$0] and [001] directions pass through the centres of the methyl groups of the methoxy species that correspond to the protrusions in the simulated STM image of Figure 5.5. In the [001] direction

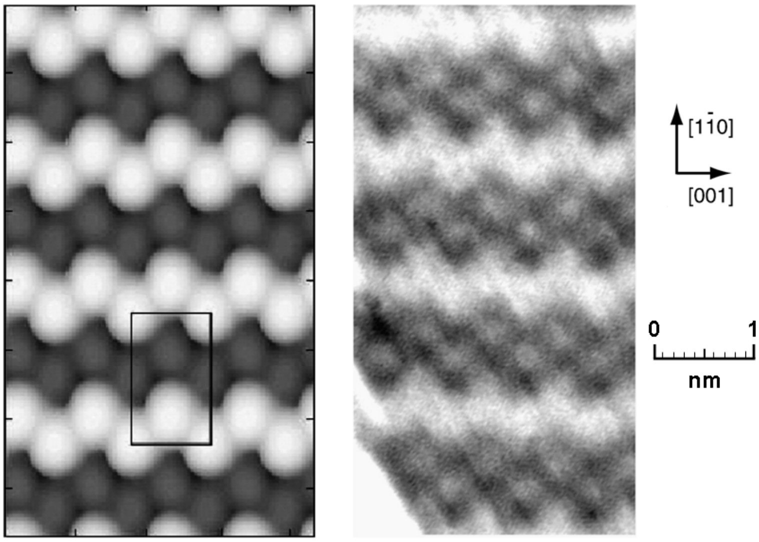

Figure 5.5: Comparison of a simulated STM image (left), taken at 8 Å from the surface, of the Cu(110) (5×2) methoxy surface obtained from the DFT calculations based on the model of Figure 5.4(a), with an experimental image (right - courtesy, M. Bowker). The experimental image was recorded at approximately room temperature, using a bias of 3.0 V and constant current of 1.0 nA, subsequent to dosing 10 L methanol on a surface pre-dosed with 5 L O. The rectangle superimposed on the simulated image shows a single (5×2) unit mesh.

the methoxy species bonded to the underlying surface bridge site are aligned along Cu-O-added rows of the (2×1)-O phase, while the methoxy species bonded to Cu adatoms form two lines that straddle the intermediate Cu-O-added row. In the [1$\bar{1}$0] direction, all the methoxy methyl radicals form lines that lie halfway between the Cu and O atoms of the Cu-O-added rows. Figure 5.7 shows a corresponding STM image [131], again with superimposed lines passing through the protrusions of the (5×2)-methoxy region that surrounds a (2×1)-O island. In the centre of the image where most of the width is taken up by the (2×1)-O island the horizontal ([001]) lines are drawn through the ordered (5×2) region on the extreme right of the image, and not through the irregular protrusions in the faulted region closest to the ordered (2×1) region. In the [001] direction the alignment of the protrusions in the two regions is clearly exactly as predicted by the model. In the [1$\bar{1}$0] direction, what is certain is that the lines of methoxy-related protrusions do not pass through the protrusions of the (2×1)-O islands that correspond to the positions of the Cu adatoms. A more precise statement of their location is more difficult. Some of the lines seem to lie very close to exactly midway between these Cu adatom (2×1)-O protrusions, and thus would appear to

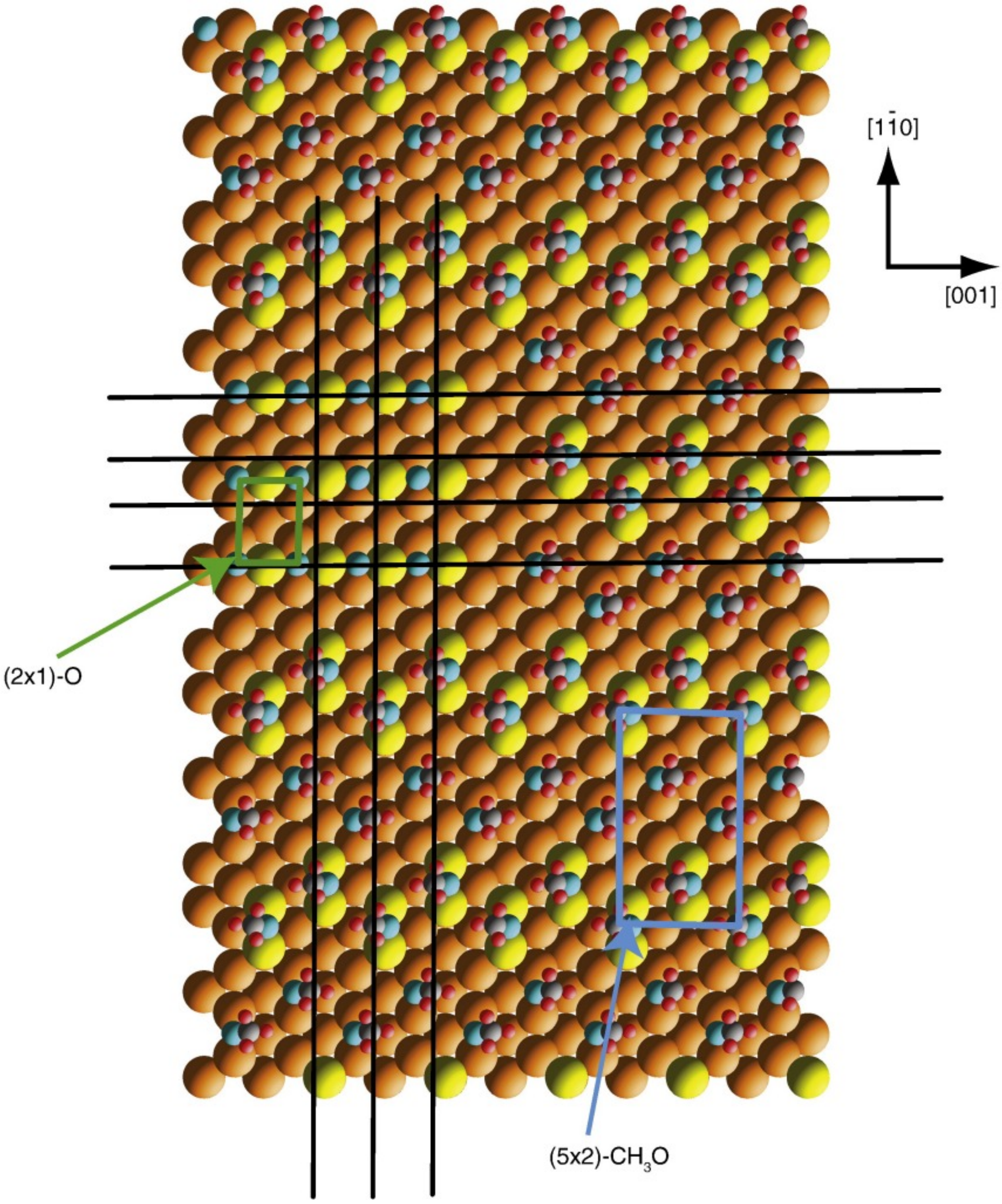

Figure 5.6: Schematic diagram showing a large-area plan view of the energetically preferred double-short-bridge site model of the (5×2)-methoxy structure (as in Figure 5.4(a)) coexisting with the (2×1)-O added-row structure. The blue and green rectangles show the unit meshes of these two phases. The superimposed black lines are centred on the methyl groups of the adsorbed methoxy species and show the relative registry to the Cu adatoms of the (2×1)-O phase.

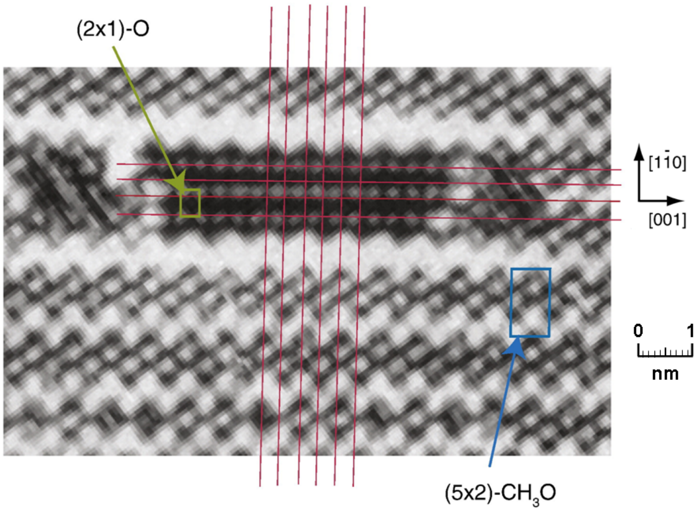

Figure 5.7: STM image showing coexisting (2×1)-O and (5×2)-methoxy regions on a Cu(110) surface (reprinted with permission from Figure 2c of ref [131]; copyright (1994) by the American Physical Society). The image was recorded at approximately room temperature, using a bias of 1.0 V and constant current of 1.0 nA, subsequent to dosing 10 L methanol on a surface pre-dosed with 5 L O. The superimposed red lines are centred on the protrusions on the methoxy phase and show the relative registry of these features to the protrusions of the (2×1)-O phase.

pass through the O atoms in the Cu-O-added rows. On the other hand, other lines appear to be closer to these (2×1) protrusions, thus corresponding to a location midway between the (imaged) Cu atoms and (non-imaged) O atoms, as predicted by the model of Figure 5.6. In truth, the resolution and signal-to-noise ratio of the experimental image is really not sufficient to distinguish these two alternative alignments in a completely reliable fashion. It is, perhaps, also important to recognise that there are limits to the precision with which such alignments of different features in STM images can be related to the true lateral positions of the underlying atoms and molecules, in part due to the intrinsically electronic (rather than atomic) nature of the technique (e.g. [150, 151]), in part due to experimental artifacts such as the influence of scan direction and instrumental time constants. Nevertheless, one may conclude that the structure proposed here of the (5×2)-methoxy phase is consistent with the appearance of the high-resolution STM images of this phase. It is also consistent with the relative registry of the methoxy and C-O-added rows in the [001] direction, but in the [1$\bar{1}$0] direction it is only possible to conclude that the model may be consistent with the experimental data.

5.1.6.2 Further PhD and XPD analysis

As a further test of this DFT model of the (5×2) phase, additional PhD simulations were performed for this structure by Dagmar Kreikemeyer Lorenzo [11], and these were compared with the experimental data. It was found that, with a little structural modification, a slightly better fit (R = 0.14) than that found for the two site model cited in section 5.1.2 could be found which, in contrast to this earlier two site model, *does not* contain any unreasonably short bondlengths.

Comparison of the optimised structural parameter values for the DFT and PhD optimisations reveals some minor differences. Most notably, the Cu-O bondlengths for the methoxy species in the adatom and substrate sites are both 1.98 Å in the DFT results, but have values of 1.98 ± 0.03 Å and 1.90 ± 0.03 Å, respectively in the PhD simulations. Less significantly, the optimum O-C tilt angles are 36-37° in the DFT calculations, while the PhD simulations also favour similar tilt angles (33 ± 14°), although in this case the precision is poor because of the very weak sensitivity of the PhD spectra to the location of the C atoms. Nevertheless, the main conclusion is that the proposed (5×2) structure does indeed provide significantly improved agreement with the PhD data relative to a model based on occupation of only short-bridge sites on an unreconstructed Cu(110) surface.

The originally suggested interpretation of the experimental XPD results for the Cu(110)/methoxy system [144, 145], in which XPD peaks were observed at both ∼40° in the [001] azimuth and ∼18° in the $[1\bar{1}0]$ azimuth, was that there were two different O-C bond orientations, and therefore two distinctly different adsorption sites. However, a recent re-evaluation of these results [11] has revealed that a simpler explanation, based on a single species tilted by ∼35° in the $[1\bar{1}0]$ azimuth, could also account for the observed results.

5.1.7 Discussion

While the lowest-energy structure identified in this study (see Figure 5.4a) for the ordered (5×2)-CH3O phase is energetically preferred over the previously identified low energy structure (see Figure 5.3) by 280 meV per methoxy species, it is not the lowest energy structure. On an unreconstructed surface a simple c(2×2) arrangement of methoxy species in short-bridge sites is lower in energy than this (5×2) phase by 150 meV per molecule, and one must conclude that the (5×2) structure is thus not the true equilibrium phase, but is a metastable structure, with transformation to the unreconstructed c(2×2) structure kinetically limited by the problem of redistributing the Cu adatoms released in the reaction that creates the methoxy adsorbates. In this regard it is notable that some published STM images [131, 132, 140] show coexistent (5×2) and c(2×2) regions, and also (n×2) regions with $n > 5$; in these latter regions, the images show c(2×2) ordering between the bright zig-zag rows that one may attribute to methoxy species in adatom short-bridge sites. The DFT calculations also show, however, that exclusive occupation of short-bridge sites on continuous $[1\bar{1}0]$ adatoms rows is also highly favourable; indeed, the energy of this structure is calculated to be slightly lower than that of the c(2×2) non-reconstructed structure (values of 30 meV and 10 meV per molecule are given by the 5-layer and 7-layer slab calculations, respectively (Table 5.2)) albeit at a lower coverage of methoxy species of 0.25 ML. One might then ask why this structure, that incorporates 0.5 ML of Cu adatoms, is not the one that is seen experimentally. One possible reason is the well-known anisotropy of surface diffusion on fcc (110) surfaces (e.g. Rh(110) [152], Ni(110) [153] and Cu(110) [154]). As may be seen from Figure 5.6, rearranging the Cu adatoms of the (2×1)-O phase into a (1×2) structure to produce alternate $[1\bar{1}0]$ rows requires half these atoms to diffuse in the 'difficult' [001] direction. By contrast, rearranging these atoms into zig-zag pairs along $[1\bar{1}0]$ only requires single jumps along the 'easy' direction. As such, the transition from (2×1)-O to (1×2)-CH_3O may well be even more strongly kinetically hindered than the transition to the (5×2)-CH_3O structure of Figure 5.4a.

5.2 Cytosine adsorption structure

5.2.1 Introduction

As part of the general trend in surface science to tackle problems of increasing complexity and potential utility, there have been an increasing number of investigations of the adsorption of biologically related molecules. While some limited characterization of the adsorption of large-scale biological molecules such as DNA and proteins is possible, notably using scanning probe microscopy, these adsorption systems are far too complex to understand at an atomic scale. For this reason most of the focus in surface science has been on the adsorption of smaller component species, such as simple amino acids and the nucleobases. While simple on the biological scale, even these component molecules provide a significant challenge for surface science and particularly for quantitative structural investigations. As a result there have been very few structural determinations of these molecular species at surfaces, but using PhD (see section 2.2), it has been possible to obtain quite detailed quantitative information on the adsorption geometry of the simplest amino acids, glycine (NH_2CH_2COOH) [155, 156] and alanine ($NH_2CH_3CHCOOH$) [117], and of the nucleobases, thymine ($C_5H_6N_2O_2$) [157] and, more recently, cytosine ($C_4H_5N_3O$ - see Figure 5.8), on Cu(110) [12].

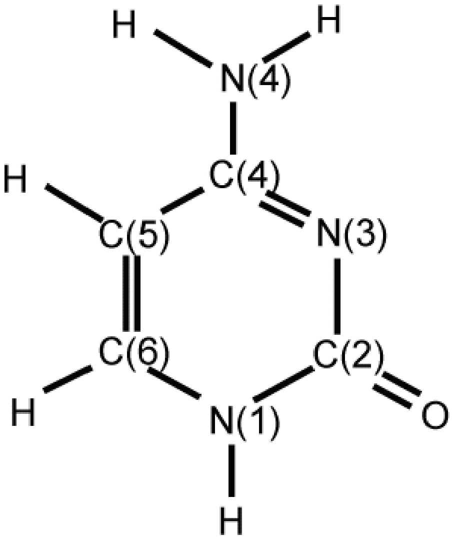

Figure 5.8: Molecular structure of cytosine showing the labelling convention for the different constituent atoms.

PhD is however a local structural probe only and, as such, it is incapable of providing information regarding the long-range ordering. DFT calculations do provide a means to explore this aspect of the structure though, and such calculations have provided possible structural models for the pseudo-(3×2) overlayer formed by alanine on Cu(110) [158]. Similarly useful information was also obtained for the (3×2) structure formed by glycine on the same surface using DFT [159], in this case determining that heterochiral domains of the molecule are significantly more stable than the alternative possibility, homochiral domains. In the remainder of this chapter the results of a DFT investigation are presented in which the ambitious task of exploring the role of intermolecular interaction in the significantly larger, (6×6), overlayer formed by cytosine on Cu(110) was undertaken. The calculations provide support for the local adsorption structure (see Figure 5.9), determined by PhD and assist the rejection of an alternative model found in the PhD study. Furthermore, based on a combination of the previous experimental and current DFT results it is considered how ordered structures containing two orthogonal glide lines may arise from this local geometry, and possible models are proposed for the (6×6) structure.

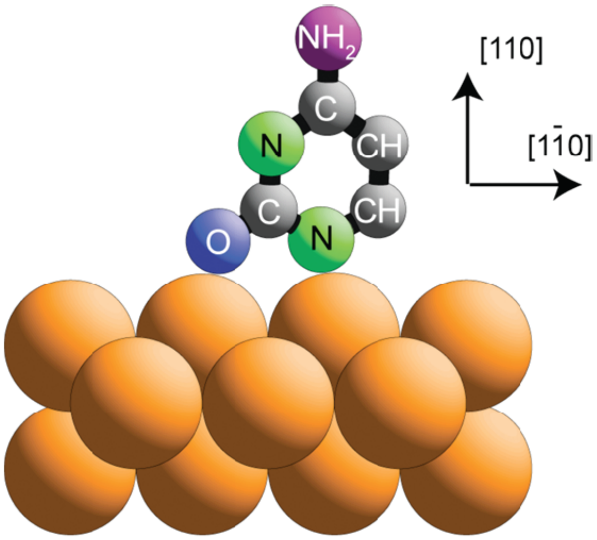

Figure 5.9: Schematic diagram of the local structure of adsorbed cytosine on Cu(110) as determined by PhD [12]. The H atoms are not shown since it is not possible to determine their location using PhD (due to their weak scattering properties).

5.2.2 Previous work

The Cu(110) surface has been the preferred substrate for many of the previous surface science studies of simple biomolecules, providing a valuable basis for comparisons, and there have been two early experimental investigations of cytosine on this surface that have provided partial structural information. Specifically, an investigation using SXPS of the O and N 1s photoemission peaks, and O and N K-edge NEXAFS [160] has provided information on the initial reaction of cytosine with Cu(110) and on the molecular orientation. For the surface species formed at low coverage ($\sim$ 0.2 ML) NEXAFS data indicate that the molecular plane is essentially perpendicular to the surface, and aligned in the [1$\bar{1}$0] azimuth parallel to the close-packed Cu atomic rows in the surface. The perpendicular orientation of the molecular plane was also inferred from infrared spectroscopy of this system [161]. The SXPS data were interpreted as indicating that chemisorption of cytosine on Cu(110) leads to deprotonation of the N(1) atom (see Figure 5.8) within the molecular ring, and it was proposed that the molecule bonds to the surface through this N atom. A second study [162] also concluded, in this case on the basis of HREELS, that the vibrational modes observed were consistent only with the molecular plane being perpendicular to the surface. This later investigation also identified two different long-range ordered phases, (6×6)pgg and (6×2)pgg, formed after annealing to ∼ 370 and 480 K respectively, by both LEED and STM. On the basis of this information, and particularly the presence of the two orthogonal glide symmetry lines seen in LEED that identified the space group as pgg, a structural model was proposed for the (6×2)pgg phase based on hydrogen bridge-bonded cytosine dimers, bonded to the surface through the O atoms (see Figure 5.10).

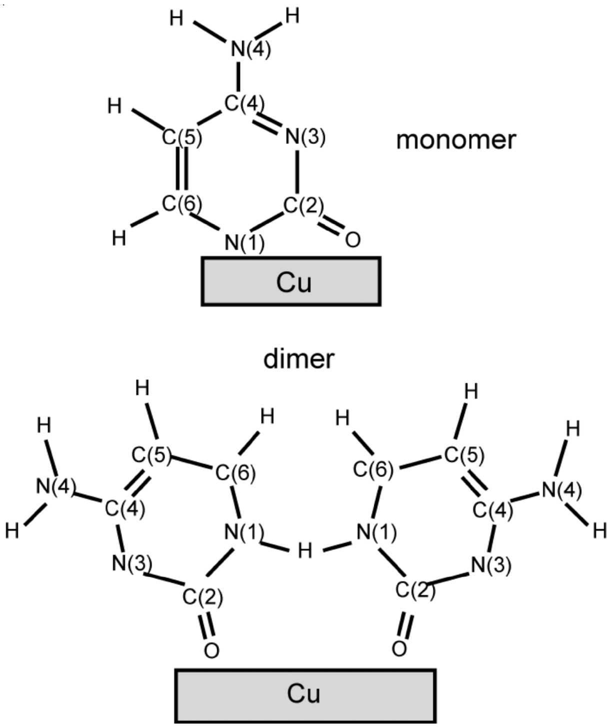

Figure 5.10: Two possible adsorption bonding configurations of cytosine-derived species on Cu(110). The deprotonated monomer is the structural model arising from the present study, and the hydrogen bridge-bonded dimer is the model proposed in reference [161]

More recently, another SXPS characterisation of the Cu(110)/cytosine system [12] revealed that heating the surface to 480 K leads to a significant change in the molecular structure, probably associated with deprotonation of the amino N(4) atom; as such, the conclusion was that it is likely that the previously identified (6×6)pgg and (6×2)pgg phases are associated with different molecular species on the surface. In this same study PhD data was collected with the aim of determining the detailed adsorption geometry for the lower-temperature preparation [12]. It was shown that in this case cytosine bonds to the Cu(110) surface through both the O atom and the N(1) atom (see Figure 5.10), and it was possible to obtain quantitative information on the local adsorption geometry including the associated adsorbate-substrate bondlengths.

5.2.3 Computational details

The RPBE exchange-correlation functional [73] was used throughout the investigation along with ultrasoft pseudopotentials (see section 3.2.4). The plane wave calculations used to investigate the cytosine adsorption and the effects of intermolecular interactions were based on 5-layer (3×1) and (4×2) supercells cells with the bottom two layers of Cu atoms fixed to the bulk positions and 3-layer (6×2) slabs with only the bottom layer similarly constrained. All other simulation parameters were optimised according to the considerations of chapter 3. While the primary interest of these calculations is in the relative energies of different structures, an absolute cytosine adsorption energy for each structure was evaluated by reference to the energy of a single N(1)-deprotonated species in isolation.

As indicated in section 5.2.1, the DFT calculations of the Cu(110)/cytosine system were undertaken not only to provide a valuable comparison to the experimentally determined structure, but also to allow some evaluation of the possible influence of intermolecular interactions which may play a role in this system. It should be acknowledged, however, that these DFT calculations take no account of any possible role of van der Waals interactions, but do include ‘chemical’ through-metal and through-space interactions including any possible influence of hydrogen bonding. In all of these calculations it was assumed that the adsorbed species has the N(1) atom deprotonated relative to the cytosine molecule, and that bonding to the surface is through the O atoms and this N(1) atom, as illustrated schematically for the monomer in Figure 5.10.

5.2.4 Isolated cytosine

Calculations were first performed for a single molecule in a (4×2) unit mesh, corresponding to a coverage of 0.125 ML; this large mesh was chosen to minimise the effects of intermolecular interactions. The structural parameter values of this optimised structure are listed in Table 5.3, along with the experimentally determined structure, as for an ‘isolated’ chemisorbed molecule. Tilting and twisting of the molecule are characterized by a set of Euler angles, (Φ,Θ,Ψ), as used in the PhD investigation of this system [12] and earlier PhD studies of other planar molecular adsorbates [157, 163, 164]. The Euler angles relate the Cartesian coordinate systems fixed relative to the surface (x_I,y_I,z_I), and relative to the molecule (x_M,y_M,z_M). Here the ‘main convention’ is used to define the order of application of the rotations. Φ defines an azimuthal rotation of the molecular coordinate system relative to the surface about the common z axes. Θ defines a rotation of the molecular axes about x_M. Ψ defines the subsequent rotation of the molecular frame about z_M. Notice that a particularly simple interpretation of these angles arises when $\Psi = 0°$; in this case Θ and Φ are the tilt and twist of the molecular plane relative to the idealised case of $\Phi = \Theta = \Psi = 0°$, the highly symmetric situation in which the molecule is fully upright with its molecular plane in the $[1\bar{1}0]$ azimuth, as implied by the NEXAFS results (see section 5.2.2).

The isolated DFT structure is essentially as found experimentally and illustrated in Figure 5.9, although there are small differences between experiment and theory in some parameters. Somewhat characteristically for chemisorption of larger molecules, the adsorbate-substrate bondlengths found in DFT are slightly longer than those found in experiment, although in view of the experimental error estimates, these differences are not formally significant. The adsorption energy of the deprotonated cytosine molecule, relative to the same species in isolation, was calculated to be 2.634 eV per molecule. While this absolute value is not testable experimentally, and is susceptible to systematic errors associated with the choice of DFT functional, the value relative to other structural models can be expected to be rather reliable.

In the structure shown in Figure 5.9 the bonding N and O atoms of the molecule, with an O-N distance shorter than the corresponding Cu-Cu distance of the substrate, are located approximately symmetrically between these two bonding Cu atoms. As alluded to in section 5.2.1, the PhD investigation of this system also identified another structure, with a similarly low R factor (using unreasonably small correlated vibrations for the N-Cu nearest-neighbor emitter-scatterer pair of atoms), in which the whole molecule was displaced along $[1\bar{1}0]$ (to the right relative to Figure 5.9) such that the O and N atoms were on the same, rather than opposite, sides of their bonding Cu atoms. One possible rationale for such an asymmetric configuration could be intermolecular interactions. However, as reported in section 5.2.5, the DFT calculations do not support this conclusion.

Table 5.3: Optimised values of the structural parameters obtained from the PhD analysis for chemisorbed cytosine on Cu(110) [12] and from some of the DFT calculations. z values denote separations perpendicular to the surface and d values are bondlengths. Δx and Δy values are the lateral offset parameters from a top site in the $[1\bar{1}0]$ and [001] azimuths, respectively while Δz_1 values are the outward relaxation of the outermost Cu layer atoms, the O and N suffices relating to the Cu atoms directly below the O and N(1) bonding atoms of the cytosine. The set of Euler angles, (Φ,Θ,Ψ) is defined in section 5.2.4. For the DFT results, no result is included for Ψ since its definition is ambiguous for a relaxed molecule and it is not informative for small values of Θ (i.e. $\Psi \approx -\Phi$).

parameter	PhD expt. [12]	DFT isolated	DFT oblique-2
$z_{\text{O-Cu}}$ (Å)	1.90 ± 0.03	1.94	1.93
$z_{\text{N-Cu}}$ (Å)	1.92 ± 0.03	1.98	1.99
Φ (°)	12(+7/-12)	1.4	6.6
Θ (°)	10(+10/-20)	0.0	4.0
Ψ (°)	0(+7/-12)		
Δx(O) (Å)	0.3(+0.2/-0.3)	0.23	0.16
Δy(O) (Å)	-0.3(+0.6/?0.2)	0.00	-0.14
Δx(N(1)) (Å)	-0.3(+0.2/-0.3)	-0.08	-0.15
Δy(N(1)) (Å)	0.2(+0.2/-0.7)	0.04	0.03
$d_{\text{O-Cu}}$ (Å)	1.94(+0.06/-0.04)	1.96	1.94
$d_{\text{N-Cu}}$ (Å)	1.94(+0.07/-0.3)	1.98	1.99
Δz_1 (Å)	-0.16(+0.06/-0.08)	-0.13	-0.20
$\Delta z_{1\text{O}}$ (Å)	0.12(±0.08)	0.03	0.01
$\Delta z_{1\text{N}}$ (Å)	0.15(±0.10)	0.01	0.06

It is therefore clear that this model can be rejected as an alternative solution.

Table 5.3 also reveals an interesting trend in the values of the relaxations, perpendicular to the surface, of the outermost Cu atom layer. In particular, the relaxation of the atoms in this layer that are not bonded to the molecule, Δz_1, show a significant inward shift, characteristic of the clean Cu(110) surface, but the Cu atoms directly below the O and N(1) bonding atoms of the cytosine adopt an outermost layer spacing that is much closer to the ideally terminated bulk. This same effect has also been seen in the results of the PhD experiments although the precision is poor.

5.2.5 Intermolecular interactions

To gain some insight into the influence of intermolecular interactions a further series of calculations were undertaken on structures with a coverage of 0.33 ML, the value believed to be relevant to the PhD experiments on the basis of the previous work of Frankel et al. [162]. Three such simple models were tested, namely: (1) a (3×1) structure, $\left(\begin{smallmatrix} 3 & 0 \\ 0 & 1 \end{smallmatrix}\right)$ in the matrix notation, (2) a $\left(\begin{smallmatrix} 3 & 0 \\ -1 & 1 \end{smallmatrix}\right)$ structure that is referred to as 'oblique-1', and (3) a $\left(\begin{smallmatrix} 3 & 0 \\ -2 & 1 \end{smallmatrix}\right)$ structure that is referred to as 'oblique-2'. The optimized structures for these three models are shown in Figure 5.11. All three structures have a 3× periodicity along $[1\bar{1}0]$, and a 1× periodicity along [001], but the unit meshes are skewed by different amounts, leading to different relative locations of the cytosine molecules in adjacent $[1\bar{1}0]$ rows. These calculations showed that the adsorption energy in the (3×1) structure was 97 meV lower than in the 'isolated' molecule ((4×2) model); by contrast, in the oblique-1 and oblique-2 models cytosine is more strongly bound than the 'isolated' molecule by 32 and 44 meV respectively. Clearly, the energetics favour adsorption of cytosine at a coverage of 0.33 ML in the staggered configurations associated with the oblique mesh models. Furthermore, optimisations starting from structures in which the molecules were shifted along the $[1\bar{1}0]$ direction by approximately 0.5 Å, such that the local structures were similar to the alternative low R factor PhD model mentioned in section 5.2.4, resulted in the same final structures. The structural parameter values found for the most favorable oblique-2 model are included in Table 5.3. In general these values are very similar to those found for the isolated model, but one key difference is a significant twist of the molecular plane relative to the $[1\bar{1}0]$ direction, similar to that favoured by the solution determined by PhD.

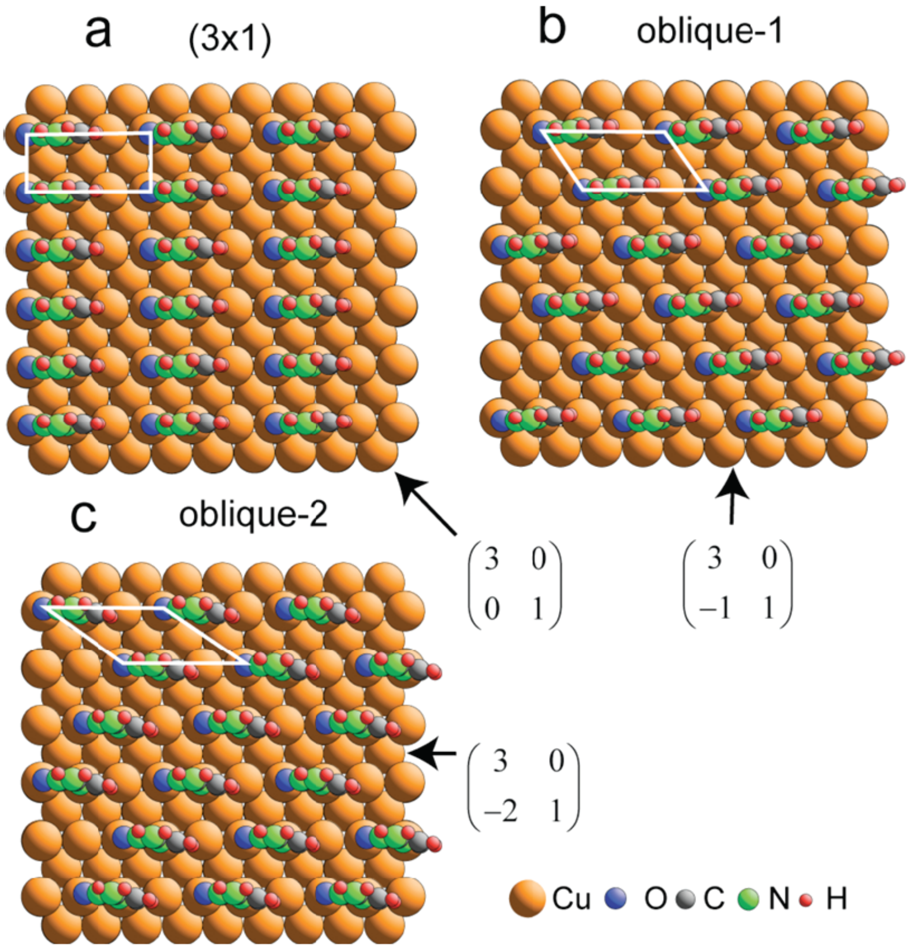

Figure 5.11: Three modified-(3×1) adsorption models for cytosine on Cu(110) tested in the DFT calculations. The adsorption geometries shown in each case are the results of the energy minimisation.

5.2.6 Long-Range ordering

So far only the local structure of cytosine on Cu(110) has been considered. From the point of view of comparing with the experimental structural information from PhD, this is appropriate. On the other hand, Frankel et al. [162] have clearly identified long-range ordered phases of cytosine on Cu(110), so it is certainly of interest to try to reconcile the local structure with possible models of the long-range ordering. A particularly significant aspect is that, based on LEED patterns, Frankel et al. have found that both the ordered structures seen (namely (6×6) and (6×2)) have the pgg space group. The presence of the two perpendicular glide symmetry lines places very significant constraints on the possible structural models. Of course, to construct meaningful structural models, it is also necessary to know the nature of the molecular species in the two ordered phases. As discussed in section 5.2.2, a comparison of the different annealing temperatures used by Frankel et al. to produce these phases (370 and 480 K respectively) with the N 1s SXPS data obtained for different heat treatments leads to the belief that the dominant surface species present on the surface in the PhD experiment (cytosine with only the N(1) atom deprotonated) is likely to be that associated with the (6×6) phase. By contrast, these same data led Jackson et al. [12] to suspect that the species leading to the (6×2) phase may also have the N(4) amino atom at least partially deprotonated. The fact that long-range ordering was not observed by LEED during the PhD experiment could, of course, mean that the local structure found was not reconcilable with this long-range ordering. However, a more reasonable assumption is that the (6×6) long-range ordered phase is composed of cytosine molecules in local geometries closely similar to that found in the experiment.

5.2.6.1 Symmetry considerations

A key feature of any structure with the pgg space group is that it is pseudo-centered, specifically, that the structural motif at the centre of the unit mesh is not identical to those at the corners of the mesh, but rather is the mirror image of these corner motifs. In the pgg structure, this central motif must be a mirror image of the motif at the corners for reflection in both of the two principal (orthogonal) [001] and [$1\bar{1}0$] azimuths of the surface. The low symmetry of the cytosine molecule is such that this motif cannot comprise a single molecule; instead, it must comprise an even number of molecules arranged such as to comprise pairs whose component parts are related by the two mirror planes. In the (6×2) phase, a coverage of 0.33 ML corresponds to 4 cytosine molecules per unit mesh, so to achieve a pgg group the structural motif must comprise two molecules. Thus, Frankel et al. [162] proposed that this phase comprises an ordered arrangement of cytosine dimers, as shown in Figure 5.10. Note, though, that this dimer itself contains two perpendicular mirror planes, one in the plane of the molecule, the other between the two constituent cytosine species. As a result, aligning the dimer in the [$1\bar{1}0$] direction and placing these dimers at the corners and center of a (6×2) mesh leads to a cmm (centered mirror-symmetric) rather than a pgg space group. Twisting the molecular plane out of the [$1\bar{1}0$] azimuth in opposite directions for the corner and centered species, however, generates the required pgg symmetry. This is the model proposed by Frankel et al., [162] that they also suggest can account for the high-resolution STM image of this phase. In the (6×6) phase the same cytosine coverage implies 12 molecules per unit mesh and thus a repeated structural motif of 6 molecules. With this level of complexity it is difficult to identify a single preferred structure on the basis of the space group symmetry and local geometry alone, but with the aid of the DFT calculations it is possible to significantly reduce the number of likely structures.

5.2.6.2 (6×6) cytosine structure

Unfortunately, calculations on a full (6×6) cytosine adsorption phase are beyond the scope of available computational resources. For example, even a 3-layer Cu slab with 12 cytosine molecules per (6×6) unit mesh leads to 252 atoms per supercell. Some insight into the problem can, however, be gained by using a (6×2) supercell with 3 Cu layers containing a more manageable number of 84 atoms. Note that these calculations are not intended to address the structure of the (6×2)pgg phase, which is believed to comprise a different molecular species, but rather to cast some light on possible preferred ordering within the (6×6)pgg phase. The geometry-optimized structures of three different (6×2) models with different cytosine packing arrangements are shown in Figure 5.12.

One initial question addressed was the relative orientation of adjacent molecules in the $[1\bar{1}0]$ rows. Looking at a single cytosine molecule bonded to the surface (as in Figure 5.9, but see also Figures 5.11 and 5.12) one sees that one end of the molecule has the O atom. If this end of the molecule is labelled as the 'head', then one can refer to two possible ways of ordering the molecules along the rows as either 'head-to-tail' or 'head-to-head', i.e., with the O atoms all at the same ends of the molecules or with the O atoms of adjacent pairs of molecules facing one another. In Figure 5.12, model (a) shows a 'head-to-head' arrangement, whereas models (b) and (c) show 'head-to-tail' alignment. Within this nomenclature, the dimer of Figure 5.10 is a special kind of 'head-to-head' arrangement, albeit with different orientation and substrate bonding of the constituent cytosine molecules. Notice that the head-to-head pair in model (a) of Figure 5.12 does not have the two mirror planes of the dimer of Figure 5.10, because of the small twist and amino tilt that characterizes the optimum cytosine adsorption geometry. The resulting structure thus produces pgg symmetry without any need to rotate the pair of molecules out of the $[1\bar{1}0]$ azimuth, in contrast to the model of Frankel et al. based on the cytosine dimer of Figure 5.10. The DFT calculations of

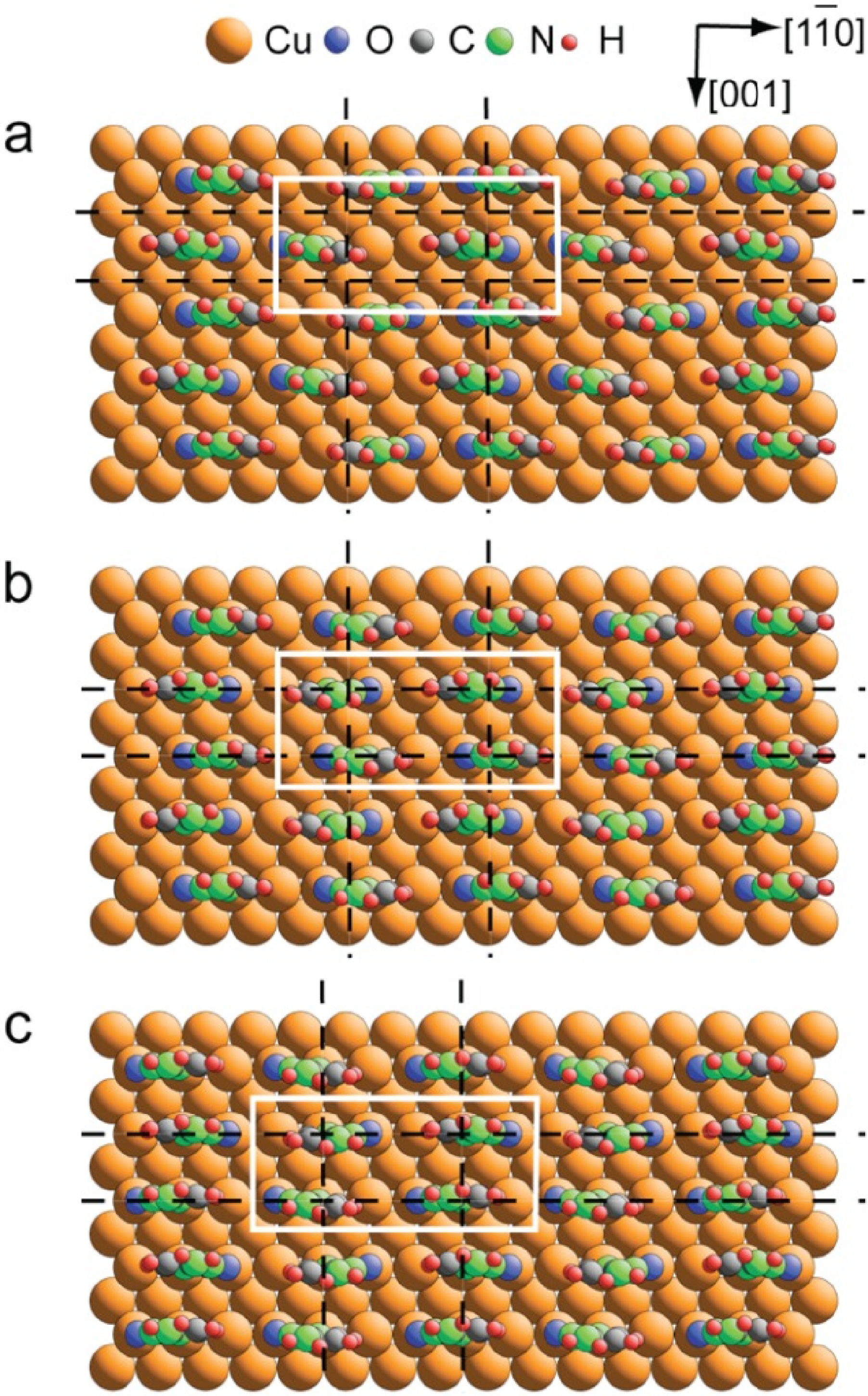

Figure 5.12: Three of the (6×2) adsorption models for cytosine on Cu(110) tested in the DFT calculations to explore the relative energies of different packing arrangements in a (6×6) structure.

these two different row ordering methods for the cytosine molecules (with the N(1) atoms atop Cu atoms spaced by 3× the Cu-Cu periodicity along the $[1\bar{1}0]$ rows in a (6×2) mesh) show that ‘head-to-tail’ is always energetically favored over the ‘head-to-head’ ordering; relative to the most favorable ‘head-to-tail’ structure tested, namely that shown in Figure 5.12b, this energy difference is 100 meV per molecule. Other results that emerged from comparison of the different adsorption energies in several different ‘head-to-tail’ (6×2) structures is that models in which the N(1) bonding atoms are aligned along [001] rows are less favorable (model 5.12c is 30 meV/molecule less favorable than model 5.12b) and models in which the O atoms are aligned along [001] rows also show $\sim$20 meV lower adsorption energies than similar structures in which the O atoms are laterally offset.

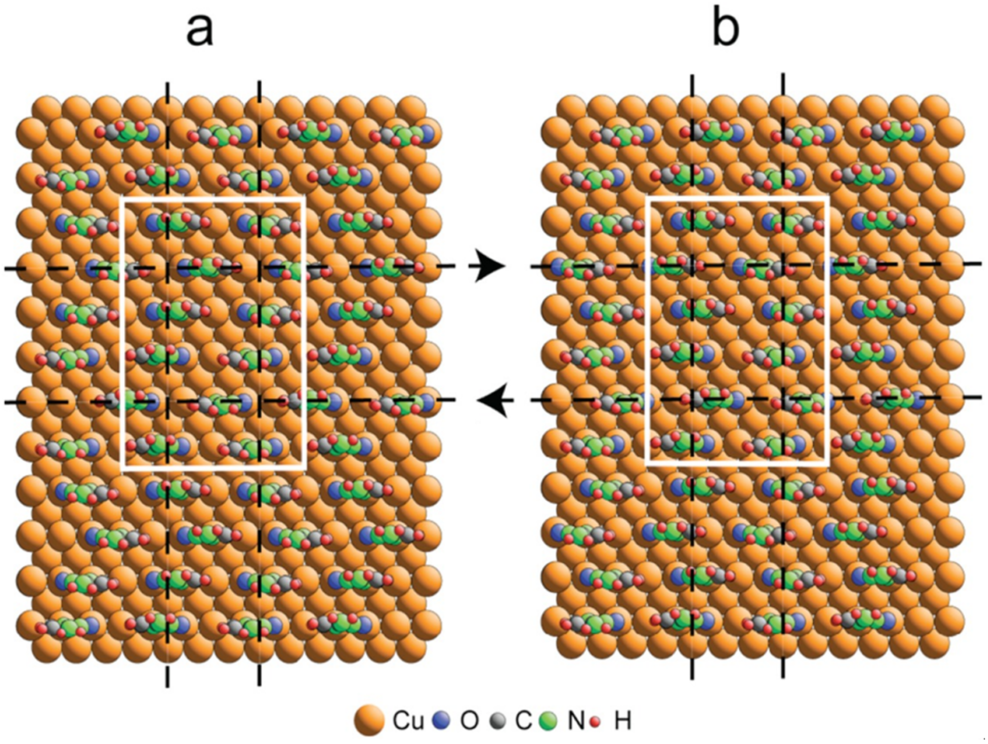

Figure 5.13: Two possible (6×6)pgg ordered structures of cytosine on Cu(110) based on the local adsorption site of the molecule found in this study that may be energetically favorable. The dashed black lines show the location of the glide lines; the white rectangle shows the unit mesh.

Figure 5.13 shows two possible (6×6)pgg structures based on the established local adsorption geometry of the cytosine. Notice that they differ only in the displacement along $[1\bar{1}0]$ of the two arrowed rows. In fact this pair of rows can have 6 different positions (corresponding to the 6 Cu atoms in this direction within the unit mesh) while retaining the pgg symmetry, leading to 6 possible structures. In addition, these rows can be moved with the two rows on either side of them to 6 different positions, so there are a total of 36 structures that can be constructed in this way that have the necessary pgg symmetry. The two structures in Figure 5.13, however, avoid the juxtapositions and the relative amino tilts angles of molecules in adjacent [$1\bar{1}0$] rows that are found to be energetically less favorable in the DFT calculations of the simpler (6×2) models. It can therefore be suggested that these two structures are likely to be the two most energetically favoured models. Comparison of these structures with the 'zigzag chain' features of the STM images of this phase presented by Frankel et al. would seem to favor the model of Figure 5.13a.

5.3 Conclusions

In this chapter the results of two DFT investigations of the adsorption structure of fundamental organic molecules on Cu(110) have been presented. Despite the interest in the methoxy species on this surface as one of the classic surface-science model systems for the study of heterogeneous catalysis, the recent PhD investigation was the first attempt to determine the local adsorption structure experimentally in a quantitative fashion, and the previously available fragmentary data that had been available led to models involving co-adsorption of low-symmetry adsorption sites. By contrast, the results from PhD suggested that methoxy occupies local short bridge sites only. The evidence from DFT presented here clearly supports this conclusion, showing a large energetic preference for adsorption at short bridge sites. However, the present results show that an important additional factor in understanding the structure of the methoxy species on Cu(110) is the role of Cu adatoms released from the surface in the reaction of methanol with preadsorbed atomic oxygen, leading to methoxy species occupying short-bridge sites on both the unreconstructed surface and on Cu adatom pairs. The resulting (5×2) model has been shown to be reconcilable with the previously-published experimental data.

The DFT results also provide strong theoretical support for the experimentally determined local adsorption geometry of chemisorbed cytosine on Cu(110) from PhD and help to reject the alternative model found in this recent study. In particular, the molecule bonds to the surface through the O atom and the adjacent deprotonated N atom that both occupy off-atop sites along the close-packed [$1\bar{1}0$]

direction. The molecular plane is essentially perpendicular to the surface and lies very close to the $[1\bar{1}0]$ azimuth. The associated Cu-N and Cu-O bondlengths are found to be 1.96 and 1.98 Å, respectively, in good agreement with PhD results and are all closely similar to that found for thymine on this surface [157]. The DFT calculations also support the presence of the reported slight twist and tilt of parts of the molecule relative to the $[1\bar{1}0]$ Cu atoms rows to which they are bonded, and this helps to provide a rationale for the previously reported tendency to form an ordered pgg phase. Using calculations of different arrangements of molecules in model (3×1)-type structures and (6×2) phases, it has been possible to propose models for the (6×6)pgg phase that are believed to be associated with this adsorbed species.

It is interesting to note the marked difference between adsorption of the methoxy and deprotonated cytosine species on the Cu(110) surface. In particular, while cytosine bonds directly to the clean surface, the clear implication that kinetic factors concerning adatom rearrangement play an important role in determining the nature of the methoxy adsorption structure raises an interesting question: do Cu adatoms play a significant role in the underlying methanol-oxygen reaction mechanism? Currently, calculations exploring this reaction mechanism at an atomic scale do not appear to have considered this possibly. Indeed, one might ask whether metal adatoms may also be relevant to other surface reactions.

Chapter 6

Surface stress changes in the Ir(001)-H system

6.1 Introduction

Reconstruction of solid surfaces, in which atoms in the outermost layer(s) undergo lateral movements, or even atomic density changes, relative to an ideal bulk termination, occurs in many systems. Even at the surfaces of metals, in which the bonding is predominantly non-directional, there are examples of both clean surface and adsorbate-induced reconstructions. Of course, the equilibrium structure of surfaces is determined by the minimisation of the surface free energy, but the role of one contribution to the energy, the relief of surface stress, has often been invoked in trying to identify the driving force for these reconstructions. Unfortunately, quantitative information about surface stress and surface stress changes is sparse (see section 2.1.4).

The Ir(001) surface is a particularly interesting system in that not only does the clean surface reconstruct to a (5×1)-hex structure, in which the outermost layer has a 20% increase in atomic density (with one extra atomic row in every five substrate spacings) to produce an approximately hexagonal close-packed surface [165–167] (see Figure 6.1), but adsorption of hydrogen on this surface leads to a new reconstruction, also having a (5×1) unit mesh. However, this hydrogen induced surface has an added-row (AR) structure [168] (see Figure 6.1) in which single [110] rows of Ir atoms with a periodicity of 5× the nearest neighbour distance, lie on an otherwise unreconstructed (001) surface layer. This hydrogen-induced transformation from the (5×1)-hex structure to the (5×1)-AR structure is one of the very few surface reconstructions for which there exists an

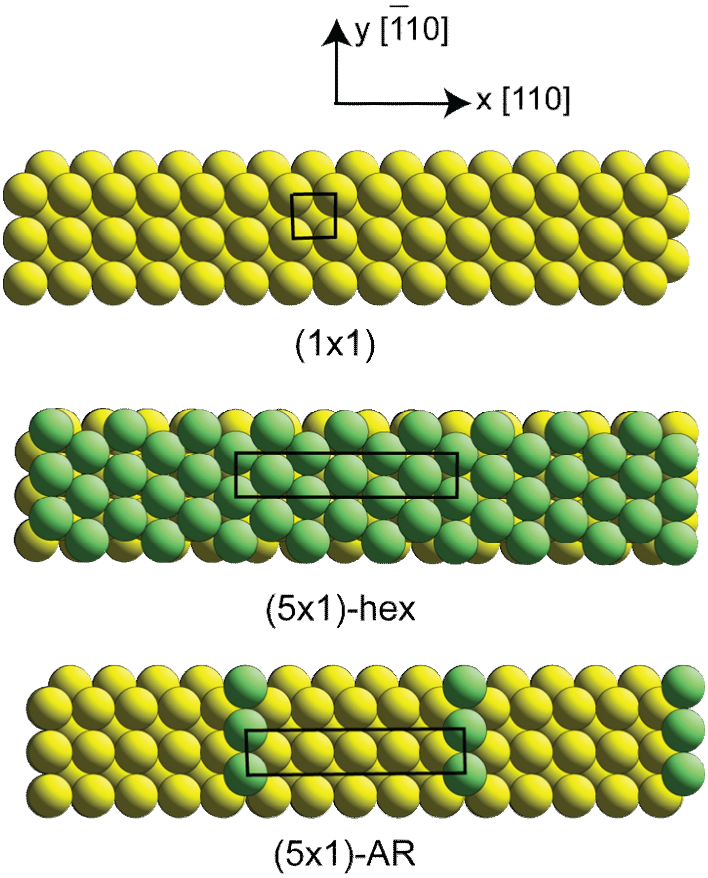

Figure 6.1: Schematic diagram of the Ir(001) clean surface models discussed in the text, showing the definition of azimuthal directions used in this chapter. The Ir atoms in the outermost layer in the hex reconstruction, and in the adatoms of the AR structure, are shown with a different colour for clarity.

experimental determination of the surface stress change, and indeed the measured (compressive) stress change is consistent with a probable lowering of the absolute value of the surface stress (which is believed to be invariably tensile for clean unreconstructed metal surfaces) [5]. The primary objective of the work reported here was to gain a description of these structures and the associated surface stress change using DFT calculations and particularly to provide a comparison with this experimental measurement. In addition, however, new DFT results are reported of the computed surface stress changes associated with the reconstruction of the ideal bulk-terminated Ir(001)(1$\times$1) surface to the Ir(001)(5$\times$1)-hex phase.

Equilibrium structures in which the outermost surface of a clean metal surface comprises a close-packed hexagonal layer are not only a feature of Ir(001), but also of Au(001), Au(111), Pt(001), and Pt(111). In all cases, the reconstruction has been attributed to relief of particularly high tensile stress in the ideal (1×1) bulk-terminated surface due to relativistic effects in these 5d metals [33, 169]. In the case of Ir(001), this interpretation was also arrived at from consideration of the measured surface phonon bands at the surface [170]. More recent DFT calculations of the surface stress change between the Ir(001)(1×1) and Ir(001)(5×1)-hex phases, however, have led to the conclusion that there is no significant change in the average surface stress and that surface stress relief is therefore not the key reason for the reconstruction [4, 171]. In fact the present calculations show that this transition is associated with an increase in the average tensile surface stress, although there is a reduction in the surface energy, consistent with the fact that the surface does reconstruct. For the hydrogen induced transformation to the Ir(001)(5×1)-AR structure, however, a significant reduction in the tensile surface stress is found, consistent with the experimental result.

6.2 Computational details

The DFT calculations reported in this chapter were conducted using the RPBE exchange-correlation functional [73] along with ultrasoft pseudopotentials (see section 3.2.4). Calculations were performed on 7-, 9- and 11-layer slabs, the outermost of these layers (on both sides) being either a (1×1) phase, a hexagonal layer, or a relaxed (1×1)-type layer plus one extra added row. In all cases, the middle three layers of these slabs were constrained to the calculated bulk fcc Ir structure with a lattice parameter of 3.906 Å. All other calculational parameters were converged according to considerations of chapter 3. Of note was the particularly dense Monkhorst-Pack k-point sampling mesh (see section 3.2.5) found to be necessary in order to converge the calculation of surface stress; the surface stress, calculated using the efficient method of Nielsen and Martin [172], is very sensitive to calculated Hellmann-Feynman forces (see equation 3.14), thus necessitating a high k-point density. Indeed, a 16×16 {4×16} k-point mesh was used for the (1×1) {5×1} surface cell calculations. With this k-point mesh it is estimated that errors in total stress values are less than 0.2 Nm^{-1} (see figure 6.2). However, errors in the relative stress of different reconstructions calculated within the same unit cell are expected to be rather smaller than this. Therefore, in order to minimise errors, all surface calculations, including those for the unreconstructed surface - Ir(001)(1×1), were conducted in the same (5×1) unit cell. In order to compare the relative energies of different surface structures (with and without adsorbed atomic hydrogen), surface energies of the double-sided slabs are calculated according to equation 3.37 with the H reservoir being gaseous H_2.

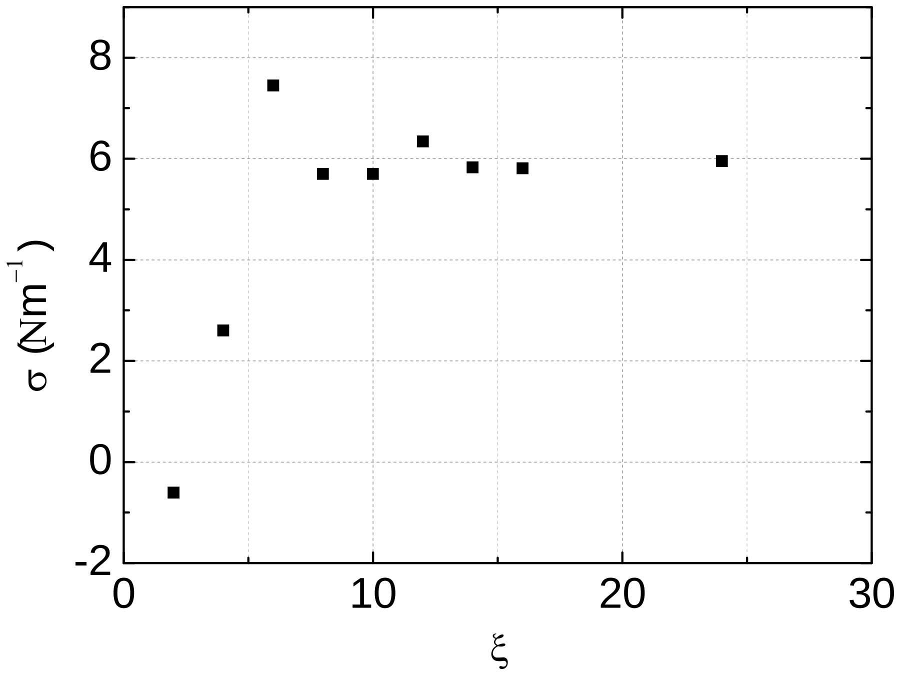

Figure 6.2: Convergence of surface stress with respect to k-point mesh for an unrelaxed Ir(001)(1×1) slab. ξ=q_1=q_2 is the number of k-points in each direction of a 2-D uniform Monkhorst-Pack k-point mesh (see equation 3.29) in the plane of the surface, i.e. q_3=1.

6.3 Results

6.3.1 Clean surface reconstructions

Table 6.1 summarises the main results of the calculations for the clean surface structures, namely the (1×1) bulk-termination, the (5×1)-hex structure, and a (5x1)-AR structure with no H adsorbates. The results are shown for three different slab thicknesses, and while the differences in surface energy for these different slab thicknesses are modest, the changes in calculated surface stress are

Table 6.1: Calculated surface energy and surface stress values for clean double sided slabs of varying thickness for three different surface phases. The surface energy is given in units of eV per (1×1) unit mesh. σ_x and σ_y are the surface stress components in the long [110] and short [$\bar{1}$10] directions (see Figure 6.1) of the (5×1) unit mesh, respectively. σ_{av} is the mean of the two stress components.

Model	Layers	γ (eV/(1×1))	σ_x (Nm^{-1})	σ_y (Nm^{-1})	σ_{av} (Nm^{-1})
Ir(001)(1×1)	7	1.369	3.38	3.34	3.36
Ir(001)(1×1)	9	1.359	3.45	3.43	3.44
Ir(001)(1×1)	11	1.364	3.51	3.52	3.51
Ir(001)(5×1)-hex	7	1.311	2.78	5.38	4.08
Ir(001)(5×1)-hex	9	1.308	3.23	5.70	4.47
Ir(001)(5×1)-hex	11	1.311	3.28	5.75	4.51
Ir(001)(5×1)-AR	7	1.398	2.22	3.46	2.84
Ir(001)(5×1)-AR	9	1.393	2.29	3.59	2.94
Ir(001)(5×1)-AR	11	1.392	2.31	3.58	2.94

more significant. In particular, there are quite significant differences (up to 16%) between the results for the 7-layer and 9-layer slabs, but the additional change in increasing the thickness to 11 layers is much smaller (<3%). This effect is much larger for the (5×1)-hex structure than for the other two structures. The clear need to take at least 9 layers (3 fixed at the centre, plus 3 relaxed on each face) to achieve reasonable convergence for this (5×1)-hex phase is consistent with previous findings of both LEED experiments [168] and DFT calculations [173, 174] that this reconstruction leads to structural changes in up to three subsurface layers. In checking the convergence of surface stress with slab thickness, it is noted that the calculated values are extremely sensitive to the lattice parameter used to define the lateral periodicity of the supercell. Calculations on a clean Ir100-(1×1) unit mesh of varying slab thickness showed that a lattice parameter increase of just 0.001 Å produces an artificial increase in apparent surface stress of 0.05 Nm^{-1} per additional pair of substrate layers. The reason is clear: if the lattice parameter is wrong, the bulk material is stressed, so adding layers increases the total stress in the slab, and this is interpreted in the calculations as being due entirely to stress at the two surfaces. The fact that the calculated surface stress values do converge with increasing thickness indicates that this has little or no influence on the present results, though it is also noted that any residual error due to this effect does not affect the calculation of relative stresses for slabs containing the same number of layers but different surface structures.

Table 6.1 shows that the surface energy of the (5×1)-hex structure is lower than that of the unreconstructed (1×1) surface, consistent with the experimental observation that this transformation occurs, although the energy difference is only 0.05 eV per (1×1) unit mesh. This value is similar to those reported in previous DFT studies using the LDA and PW91 functionals that gave values of 0.14 eV [171] and 0.05 eV [174] respectively. Table 6.1 also shows, however, that the average tensile surface stress actually increases in this transformation to the hex phase; this reinforces the more recently-held view that surface stress relaxation cannot be the driving force for the reconstruction [33, 171]. The only previous surface stress DFT calculation for this transformation reported that there was no significant change [171], but this calculation was performed using only a 5-layer slab, so the results presented here indicate that this was unlikely to be properly converged. In fact the current calculations show that the surface stress in the [110] (5×) direction of the surface unit mesh (σ_x) is reduced slightly, but that in the [$\bar{1}$10] (1×) direction (σ_y) is increased rather substantially.

While the calculations provide clear answers regarding the predicted changes in surface stress, interpreting these changes in terms of physical processes is potentially complex. For free-electron-like metals a particularly simple picture can be derived from a jellium model, in which the tensile surface stress of a clean unreconstructed surface is attributed to the electron charge spill-over into the vacuum and a resulting depletion of such charge in the surface layer; within a density-functional formalism this means attributing the effect to the change in the kinetic energy contribution [175, 176]. For d-band metals the situation is more complex, with the role of the localised d-electrons, in particular, making a picture based on interatomic bonds and bond coordination more relevant [169]. However, a recent computational study of the surface stress of a wide range of d-band metals indicates that for the late elements in the 5d series, and particularly for Ir, the charge spill-over is the dominant contribution [177]. The present results are therefore discussed within this simple picture, but it is noted that an alternative interpretation in terms of local bonding can also be shown to be qualitatively consistent with the results.

The small decrease in the stress associated with the transition from the (1×1) to (5×1)hex phase in the [110] direction can then be seen to be qualitatively consistent with the expectation that packing in an extra Ir atomic row and reducing the atom spacing in this direction should increase the electron charge density and reduce the tensile stress. By contrast, the much larger increase in the [$\bar{1}$10] direction, in which the atomic spacing is unchanged, is at first sight surprising. However, it is noted that the pseudohexagonal surface layer is heavily rumpled

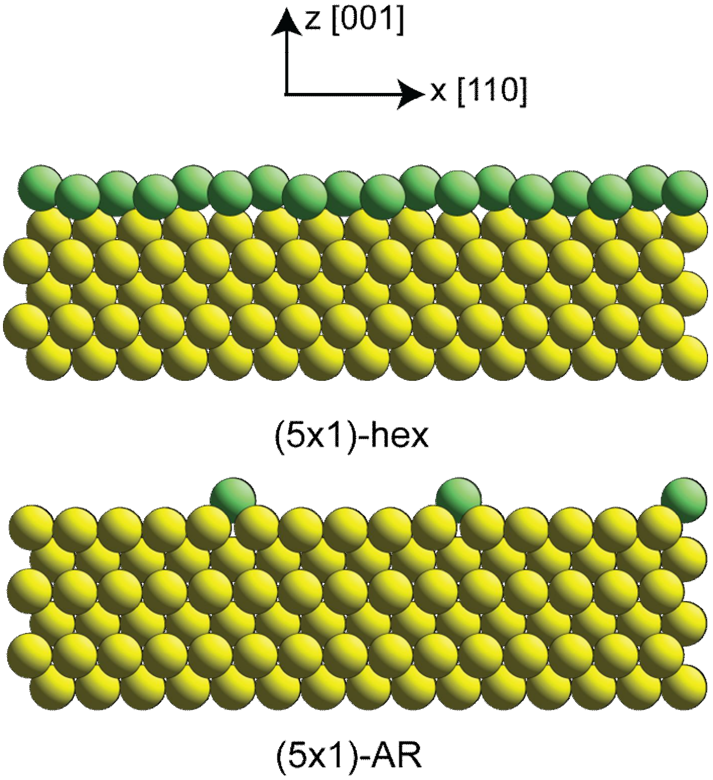

Figure 6.3: Schematic side views of the Ir(001)(5×1) clean surface models shown in Figure 6.1. The exact geometry is that corresponding to the minimum total energy in 11-layer DFT calculations, as described in the text.

(see Figure 6.3), causing the average spacing of this layer to the underlying unreconstructed layer to be significantly larger than in the (1×1) termination. This average outward shift places the surface layer in a region of depleted valence charge from the underlying surface, and this can be expected to increase the surface stress. In view of this, the rather small decrease in tensile stress in the [110] direction can be seen as due to a near-balance of two competing processes.

In order to provide further clarification of these underlying mechanisms, additional surface stress calculations were performed for a number of fixed model structures. In one of these the minimum-energy (5×1)-hex structure was changed only by increasing the layer spacing of the reconstructed surface layer relative to the underlying bulk. An increase in this spacing of only 0.1 Å led to new values for σ_x and σ_y of 5.18 and 7.43 Nm^{-1}, increases of 1.90 and 1.68 Nm^{-1}, respectively, providing clear confirmation of the influence of increasing the layer spacing. In a second model, the rumpling of the reconstructed hex layer was removed but the average interlayer spacing of the minimum-energy structure retained. This calculation yielded values for σ_x and σ_y of 0.54 and 5.42 Nm^{-1}. The value of σ_y in this unrumpled model structure is very similar to that of the equilibrium rumpled structure, indicating that in this direction the stress is predominantly determined by the average layer spacing. By contrast, the value of σ_x in this unrumpled model structure is much lower than in the rumpled structure; removing the rumpling increases the linear packing density along [110] and thus relieves the tensile stress in this direction more effectively. The results of further calculations using different layer spacings confirm this pattern of behaviour, while calculations for isolated surface layers (with the substrate removed) led to very large increases in tensile stress due to the further depletion of valence surface charge within the layer.

The results for the (5×1)-AR clean surface structure are also consistent with this simple picture. Note that the surface energy of this structure is higher than either the (1×1) or the (5×1)-hex phases, consistent with the fact that this structure does not occur in the absence of adsorbed hydrogen. In this model the outermost surface layer has a structure closely similar to that of the (1×1) termination, with an almost ideal bulk-termination, but for the addition of a single added row with a 5× periodicity (see Figure 6.3). A modest reduction in σ_x may be attributed to an increase in the average valence charge density within the outermost (1×1) layer due to electrons coming from the adatom row after Smoluchowski smoothing. The value of σ_y is very similar to that of the (1×1) phase, a result that may be attributed to a combination of the reduction in the tensile stress in the outermost complete layer as for σ_x, but a contribution of higher tensile stress from the atoms in the added row which have a greatly-depleted valence charge density.

6.3.2 H-induced reconstruction

In order to calculate the surface stress changes associated with the hydrogen-induced (5×1)-AR structure one needs to establish two things, namely the H coverage and the H adsorption site(s). Within the (5×1)-AR surface unit mesh there are a large number of possible individual sites, and as the H coverage is likely to be greater than 0.2 ML (i.e. greater than one H atom per unit mesh) there is an even larger number of possible combinations of different sites that might be occupied. Nevertheless, calculations for 12 different singly-occupied sites showed that 3-fold and 4-fold coordinated sites were unstable, the H atoms moving to atop or bridging sites. The properties of the 8 stable atop and bridging sites are shown in Table 6.2. Establishing the relative energies of multiple occupation of the many different combinations of sites (of up to 4 H atoms per unit mesh - a coverage of 0.8 ML), however, is a formidable computational task, but a recent publication [178] has reported the results of such an investigation using a novel approach to reduce the computational demands. Several of these results have also been reproduced more recently by Vukajlovic et al. [179]. The present results for the single sites are fully consistent with the results of these papers, as are the conclusions regarding the most favourable combinations of sites. Figure 6.4 shows the labelling convention used in this chapter for these bridge and top sites, while Table 6.2 summarises the results of calculations for 7-layer double-sided slabs. Shown in this table is not only the surface stress values and the surface energy per (1×1) unit mesh, but also the adsorption energy per H atom, E_a, as defined by equation 3.35.

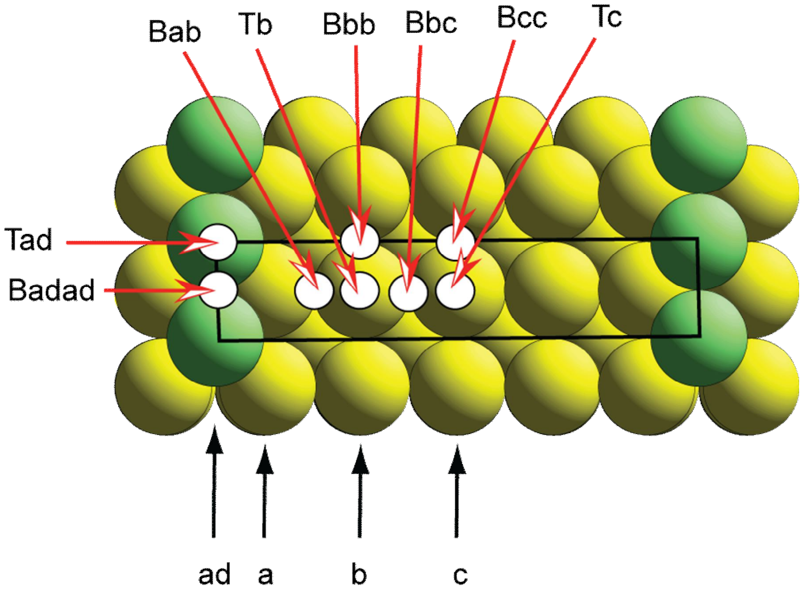

Figure 6.4: Schematic diagram of the (5×1)-AR surface structure with a number of sites for H adsorption labelled. Bridge sites are labelled ‘B’ followed by the labels of the rows occupied by the nearest neighbour Ir atoms (ad (adatom), a, b or c). Top sites are labelled ‘T’ followed by the label of the row occupied by the underlying single nearest-neighbour Ir atom.

In addition to calculations for H adsorption on the (5×1)-AR structure re-

Table 6.2: Adsorption energies, E_a, surface energies, γ, (as defined in section 6.2) and surface stress values calculated for various H adsorption structures on the Ir(001)(5×1)-AR surface. All results are for 7-layer slabs apart from the bracketed values in the last two rows which are for 11-layer slabs.

Model	coverage (ML)	E_a (meV)	γ (eV/(1×1))	σ_x (Nm^{-1})	σ_x (Nm^{-1})	σ_{av} (Nm^{-1})
Ir(001)(5×1)-hex						
1H	0.2	337	1.244	2.11	4.71	3.41
2H	0.4	318	1.184	2.41	4.22	3.31
3H	0.6	307	1.127	1.94	3.28	2.61
Ir(001)(5×1)-AR						
Tad	0.2	491	1.301	2.13	2.88	2.50
Tb	0.2	506	1.298	2.05	3.14	2.59
Tc	0.2	509	1.297	2.01	3.22	2.62
Badad	0.2	798	1.239	2.36	3.77	3.06
Bab	0.2	478	1.303	2.05	2.90	2.48
Bbc	0.2	657	1.267	2.16	2.95	2.56
Bbb	0.2	656	1.268	1.78	3.39	2.59
Bcc	0.2	680	1.263	1.69	3.45	2.57
Badad+Bcc	0.4	740	1.103	1.82	3.73	2.78
Badad+2×Bbb	0.6	708	0.974	1.51	3.82	2.67
Badad+Bbb+Bcc	0.6	717 [715]	0.968 [0.963]	1.39 [1.55]	3.77 [3.92]	2.58 [2.74]
Badad+2×Bbb+Bcc	0.8	707 [704]	0.833 [0.829]	0.80 [0.99]	3.70 [3.91]	2.25 [2.45]

ported in Table 6.2, a few results are included for adsorption on the (5×1)-hex phase, using the (sequentially-filled) preferred 3-fold coordinated adsorption sites, previously identified in DFT calculations by Lerch et al. [174], and in the earlier combined LEED/DFT study of Poon et al. [180]. The associated adsorption energies provide a further check on the present results, and are found to be closely similar to the earlier published values [174]. The current values are approximately 60 meV/atom smaller (before application of the small correction for the vibrational ground-state energy included in this earlier work), a difference that may be due to the different (PW91) functional used by Lerch et al.

Comparison of calculated H adsorption energies with those of the previous study in the (5×1)-AR surface [178] shows the same behaviour, with the ordering of the preferred single adsorption sites, namely Badad > Bcc > Bbc > Bbb > Tad > Tc > Tb > Bab being identical to that of this earlier study. Comparison of the surface energies given in Table 6.2 for H adsorption on the (5×1)-hex and (5×1)-AR structures shows that even for the lowest coverage of 0.2 ML (one H atom per (5×1) unit mesh), there is a small energetic advantage to reconstruction to the (5×1)-AR phase with the H atoms adsorbed in the Badad site bridging nearest-neighbour Ir atoms in the adatom rows. This energetic advantage for the phase transition increases with increasing coverage.

Table 6.2 also shows that the combination of H adsorption and the associated transformation from the clean surface (5×1)-hex phase to the hydrogen-covered surface is accompanied by a significant reduction in the tensile surface stress. In this case there is the possibility to compare this result with an experimental measurement which showed a total surface stress change of -1.7 nm^{-1} for this same transition [5]. Here it should be noted that, because the Ir(001) surface has 4-fold rotational symmetry, the anisotropy associated with a single rotational domain of any of the (5×1) surface phases cannot be measured. Instead, the surface comprises domains of (5×1) and (1×5) structures that are expected, for an ideally-oriented (001) surface, to be equally occupied. The experiment thus measures the average of the two orthogonal orientations, and must be compared with the computed values of σ_{av}. For the clean (5×1)-hex surface the value calculated for an 11-layer slab, 4.51 Nm^{-1}, is likely to be the most reliable. The appropriate value for the hydrogen-covered (5×1)-AR phase depends on the H coverage, but it has been reported that thermal desorption measurements indicate a coverage of 0.8 ML [181].

In the present calculations for the surface stress of the clean surface structures it was noted in section 6.3.1 that the need to include at least 9 layers in the computed slab was most acute for the (5×1)-hex surface, due to the significant subsurface relaxations in this phase. On this basis, 7-layer slab calculations may suffice for the (5×1)-AR-H phase, but to minimise any possible errors additional 11-layer slab calculations were performed for the energetically-favoured highest H-coverage structures. These are included in square brackets in Table 6.2. The surface stress value for the 11-layer slab at a H coverage of 0.8 ML given in Table 6.2 is 2.45 Nm^{-1}, corresponding to a reduction from the clean surface of 2.06 Nm^{-1}, quite close to the experimental value. In view of the uncertainty in the H coverage however, it is also noted that for a coverage of 0.6 ML the calculations predict a reduction in the tensile surface stress of 1.76 Nm^{-1}, even closer to the experimental value.

6.4 Conclusions

The results of the DFT calculations presented in this chapter for the Ir(001) surface provide some further insight into the role of surface stress in the clean and H-induced reconstructions. In the case of the clean surface (1×1) → (5×1)-hex transition, the results reinforce the more recently-held view that this transition does not reduce the surface tensile stress. Indeed, while the previous calculation indicated almost no change in the surface stress associated with this transformation [171], the new calculations presented here show that if the thickness of the slab used in the calculation is increased sufficiently to account fully for the subsurface relaxations of the (5×1)-hex phase, there is actually a significant increase (of $\sim$1.0 Nm^{-1}) in the tensile surface stress. Nevertheless, the surface energy is reduced, consistent with the fact that the (5×1)-hex phase is found to be the equilibrium structure. A previous experimental study of the H-induced transition to the (5×1)-AR phase, however, has shown that this transformation is accompanied by a reduction in the tensile surface stress of 1.7 Nm^{-1}, an effect reproduced in the present theoretical calculations that show a closely similar value for the reduction of 1.76-2.06 Nm^{-1}, depending on the H coverage in the range 0.6-0.8 ML.

Chapter 7

Methanethiolate adsorption on Cu(100) and Cu(111)

7.1 Introduction

Over the last couple of decades a significant amount of effort has been invested in understanding the interaction of n-alkanethiols ($CH_3(CH_2)_{n-1}SH$) with coinage metal surfaces (Cu, Ag, Au) [182–185]. This work has been motivated by the current and potential applications of the resulting self-assembled monolayers (SAMs) of deprotonated thiols ($CH_3(CH_2)_{n-1}S$ - thiolates) in electronic materials and chemical and biochemical sensors (e.g. [186–188]). Methanethiolate is the simplest such species, with $n = 1$, and can be readily produced on many surfaces either by deprotonation of methanethiol or by S-S bond scission of dimethyl disulphide ($(CH_3S)_2$ - DMDS).

On Cu(100) it has been found that, for various chain lengths, thiolates occupy four-fold hollow sites on the unreconstructed Cu surface [189–192] and, at a thiolate coverage of 0.25 ML, a p(2×2) structure is observed. Such a phase is not uncommon for small molecular adsorbates at low coverage on fcc(100) surfaces. Indeed, S is also adsorbed in a p(2×2) phase on Cu(100) at low coverage and similarly occupies four-fold hollow sites. Interestingly, however, the p(2×2) phases of CH_3S and S on Cu(100) are two of the few cases where experimental evidence exists for adsorbate-induced lateral strain without major reconstruction. For the Cu(100)(2×2)-S system, several independent investigations have indicated that the four surface Cu atoms surrounding the S atoms are displaced radially outwards from the S atom (see the p(2×2) structure of Figure 7.1) by approximately 0.03 Å [193–196], while there is evidence of a significantly larger radial strain, 0.12 Å, in the Cu(100)(2×2)-CH_3S system [197]. Such outward relaxations are typically expected to be a signature of adsorbate-induced compressive surface stress.

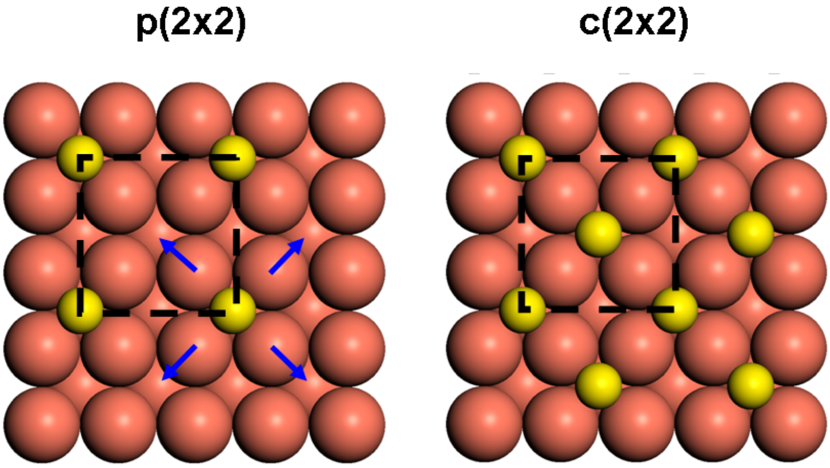

Figure 7.1: Schematic diagrams of p(2×2) and c(2×2) atomic adsorbate structures on the fcc(100) surface with adsorbates (yellow) occupying 4-fold coordinated hollow sites. Enclosed within the dashed lines are (2×2) unit cells while the blue arrows in the p(2×2) structure show the direction of surface Cu atom relaxation in the case that adsorption induces compressive surface stress. In the c(2×2) structure the surface layer Cu atoms are pinned by the adsorbates and are therefore unable to relax laterally.

For the methanethiolate/Cu(100) system, greater exposure results in a faulted c(2×2) phase, which has been attributed either to a rumpling of the surface [198] or a periodic adsorbate vacancy array [192]. A commonly observed high coverage adsorbate arrangement, particularly for atomic adsorbates, on the coinage metals is that of a c(2×2) structure (e.g. S on Ni(100) [199]), which corresponds to an adsorbate coverage of 0.5 ML. A possible reason why such a structure may not be realised for some adsorbate systems, however, is that, contrary to a p(2×2) or a faulted c(2×2) structure, the symmetry of a pure c(2×2) phase does not allow any lateral relaxation of the Cu-Cu spacing, thus denying an important stress relief mechanism (see Figure 7.1). In this regard, it is noteworthy that S also does not form a c(2×2) phase on Cu(100), instead realising a $(\sqrt{17} \times \sqrt{17})R14^\circ$ phase incorporating 0.47 ML of S [200]. Although no quantitative structure determination exists for this structure, one suggested model [199] comprises a rotated (100)-type c(2×2) reconstructed outer layer that has Cu-Cu distances 3 % larger than those of the underlying Cu(100) substrate. Of course, while Cu and Ni are both fcc solids with lattice parameters that differ by only 2 %, their electronic and chemical properties differ considerably. Nevertheless, the observed local surface strain in the Cu(100)(2×2)-S phase, and the fact that the high-coverage phase may involve a strained reconstructed layer, does suggest that adsorbate-induced compressive surface stress may be an important factor in the structure of this surface.

On the (111) surface of coinage metals, adsorption of alkane thiols induces a substantial surface reconstruction [201]. For methanethiol ($n = 1$) [202, 203] and octanethiol ($n = 8$) [204, 205] on Cu(111) this reconstruction is believed to take the form of a restructuring of the outermost Cu layer to a rotated pseudo square arrangement with the S headgroups occupying four-fold coordinated hollow sites, as found on the Cu(100) surface. In this case, however, the surface periodicity, determined by STM [202], suggests that the Cu-Cu separation of the surface layer, which is incorporated in a $\left(\begin{smallmatrix}4 & 3\\ 3 & -1\end{smallmatrix}\right)$ surface mesh (see Figure 7.2), is approximately 15% larger than that of the Cu(100) surface. Although no quantitative structure determination has been carried out for this system, this model has been supported by MEIS data which were found to be consistent with the surface containing just one reconstructed Cu layer incorporating 2/3 ML of Cu adatoms. Since a square mesh is incommensurate with the (111) surface, it is clear that there is considerable scope for the Cu-Cu spacing of the overlayer construction to find a value which provides effective stress relief in the surface layer. Therefore, the fact that there is a large increase in the Cu-Cu spacing relative to (100) surface, and that significant strain has been measured in the Cu(100)(2×2)-CH_3S system, raises an interesting question: Does methanethiolate adsorption on Cu(100), where the surface layer periodicity is fixed by the underlying bulk, indeed induce significant compressive surface stress? If so, does this impact detrimentally on the surface energy of a c(2×2) adsorbate structure, making one of the proposed faulted phases more favourable? Answering these questions is the focus of section 7.3. In addition, DFT calculations provide a means to find low-energy solutions for the quantitative structure of the high coverage Cu(111)-CH_3S system, and can thus provide evidence regarding the physical plausability of the proposed pseudo square reconstruction. The results of such calculations are presented in section 7.4 and are analysed in conjunction with new multiple scattering MEIS simulations performed by Daniel Sheppard at the University of Warwick.

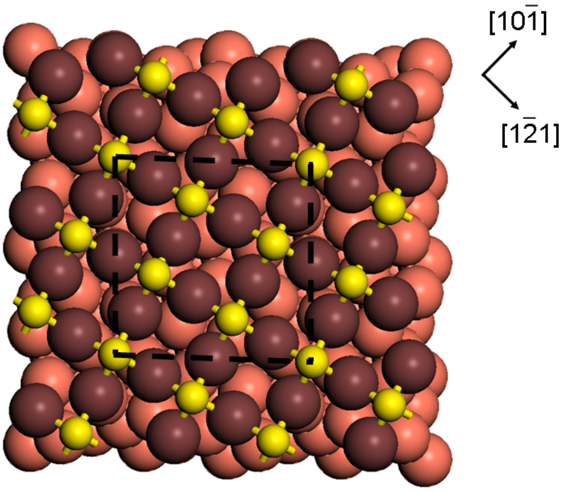

Figure 7.2: Schematic diagram of the pseudo square overlayer found to satisfy MEIS data for methanethiolate on Cu(111) [203]. Only the S atoms (yellow) of the thiolates are shown because the scattering cross section of the other constituent atoms is too small for them to be observed in the MEIS experiment. The lateral registry of the outermost Cu layer (shaded more darkly for clarity) with the underlying substrate is arbitrary.

7.2 Computational details

The DFT calculations presented in this chapter have been performed with the RPBE exchange-correlation functional [73] and ultrasoft pseudopotentials (see section 3.2.4). On Cu(100) 9-layer double-sided Cu slabs with the middle three layers fixed to the bulk lattice parameter have been used to simulate the (2×2) adsorbate structures while the c(6×2) models, required to simulate the proposed faulted c(2×2) models, have been constructed using a 5-layer double-sided Cu slab with only the centre layer constrained. A c(2×2) structure generated using both 5- and 9- layer slabs was found to give an adsorption energy 26 meV larger using the 5 layer slab as well as a slightly smaller value, by 0.1 Nm^{-1}, for the surface stress. For the Cu(111) surface, the (2×2) and (3×2) structural optimisations were conducted using 5-layer single-sided Cu slabs while adatom-reconstructed surfaces have been simulated using 3-layer slabs. In all 5-layer Cu(111) slab calculations the bottom 2 layers were constrained to bulk positions while the bottom layer only was constrained in the 3-layer slabs. All other calculation parameters were converged according to the considerations of chapter 3.

In order to compare the relative energies of surface structures involving different numbers of adsorbates and Cu adatoms, the surface energy, γ, is calculated using equation 3.37 where the adsorbate reservoir for the thiolates is chosen to be gas phase dimethyl disulfide ($(CH_3S)_2$ - DMDS), such that E_r is equal to half the energy of a DMDS molecule calculated in the gas phase. To allow additional comparison, the same energy is also substituted into the normal definition of adsorption energy, E_a (see equation 3.35), in place of E_{ads}, to give the energy released upon adsorption per thiolate (reaction energy),

$$E_a^* = \frac{E_{cr+ads} - (E_{cr} + N_{ads}E_r)}{N_{ads}}. \tag{7.1}$$

Similarly, owing to the fact that a surface is usually exposed to gaseous S_2 if one wishes to create S adsorption phases experimentally, the energy of S_2 has been calculated in the gas phase and used as the S reservoir for the calculation of γ and E_a^*. In most cases, and especially so for the c(6×2) missing row structure of methanethiolate on Cu(100), it was necessary to conduct multiple optimisations, incorporating a range of molecular twists and azimuthal orientations, to ensure that the lowest energy structure had been found. Simulated STM images of the surface structures were generated using the Tersoff-Hamann approximation (see section 3.3.5).

7.3 Adsorption on Cu(100)

7.3.1 Previous work

On the Cu(100) surface it is well known that thiolates form a p(2×2) phase at low coverage and, for the case of methanethiolate adsorption, a surface extended X-ray absorption fine structure (SEXAFS) study, conducted by Kariapper et al. [191], has determined that the S-C bond is orientated normal to the surface with a bond length of 1.83±0.05 Å. Furthermore, a MEIS experiment by Sheppard et al. [197] has determined an estimated shift in the radial lateral displacement of the Cu atoms from bulk continuation sites of 0.12±0.04 Å upon adsorption, with an accompanying outward relaxation of the surface layer of 0.08±0.04 Å. These conclusions provided support for an earlier theoretical study by Ferral et al. that also revealed this effect, reporting values of 0.04-0.09 Å and 0.05-0.08 Å for the outward radial and perpendicular relaxations, respectively [206]. At higher coverage, STM studies by Driver et al. [198] and Kondoh et al. [192] have shown that there is a propensity for thiolates to form a c(6×2) phase. It should be noted, however, that no LEED investigation of this surface has been possible since methanethiolate is extremely sensitive to electron beam decomposition [198].

7.3.2 (2×2) models

The aim of this investigation was to determine the structure of the high coverage c(6×2) phase and explore the role of surface stress in the methanethiolate/Cu(100) system. An important first step in doing this, however, is to understand the role of surface stress in the known p(2×2) structure. Included in Table 7.1 are the results of the energetically preferred optimisations of the various models explored. In all cases occupation of 4-fold hollow sites only has been assumed for the thiolate species. For methanethiolate adsorbed in both the p(2×2) and c(2×2) structural phases there are two local minimum energy geometries above the 4-fold hollows that have similar adsorption energy, namely an erect and tilted species. An interesting observation, however, is that the energetic hierarchy of the erect and tilted adsorption geometries differs at low and high coverage. At the lower coverage of 0.25 ML the S-C bond of the thiolate is erect (0.2° to the normal), in agreement with the previous SEXAFS study [191], but in the preferred geometry at 0.5 ML the S-C bond is tilted at an angle of 23.7° to the normal (see Figure 7.3). Both values are in good agreement with the DFT study of Ferral et al. [206] who found 0.0° and 24.8-26.8°, depending on the starting structure, for the tilt angles of the S-C bond in lowest energy p(2×2) and c(2×2) phases, respectively. A further comparison that can be made between the present study and previous structural investigations is the S-C bondlength in the p(2×2) phase, the value determined in the present DFT investigation of 1.853 Å (not included in the Table 7.1) being in excellent agreement with the SEXAFS result (1.83±0.05 Å [191]) and the value reported in the previous DFT study of this system (1.852 Å [206]).

The outward radial expansion of the Cu atoms bonded to methanethiolate in the p(2×2) phase (see Figure 7.1) relative to the clean surface can also be compared to experiment. The value of 2.0% calculated here, corresponding to a lateral shift of 0.04 Å away from bulk continuation sites, is qualitatively consistent with the MEIS results of Parkinson et al. [203], although the reported lateral atomic shift of 0.12±0.04 Å is somewhat larger than that found in the present study. Nevertheless, these values can be compared to the p(2x2) phase of S on Cu(100). In this case the radial expansion of the Cu atoms bonded to S is calculated to be 0.9%, corresponding to a smaller lateral shift of 0.02 Å. Once again, this smaller shift in the Cu(100)(2×2)-S system compared to that of

Table 7.1: Selected energetic, surface stress and structural parameters for various phases of methanethiolate adsorption on Cu(100). E_a, E_a^* and γ are the adsorption energy per adsorbate, reaction energy and surface energy as defined in section 7.2. σ_x and σ_y are the values of surface stress in the x and y direction, respectively, and the structural parameters from left to right are the S-Cu nearest neighbour distance, the S-Cu separation perpendicular to the surface, the angle of the S-C bond to the surface normal and the expansion, due to adsorption, of the Cu-Cu diagonal above which the methanethiolate resides. Two S adsorption phases on Cu(100) and the clean Cu(100) surface are included in the table also for comparison.

Adsorbate	Phase	Adsorbate coverage (ML)	E_a (eV)	E_a^* (eV)	γ (meVÅ^{-2})	σ_x (Nm^{-1})	σ_y (Nm^{-1})	S-Cu (Å)	[S-Cu]$_z$ (Å)	S-C tilt (°)	Radial expansion (%)
CH_3S	p(2×2) erect	0.25	2.324	0.977	46.8	0.71	0.72	2.347 / 2.352	1.428 / 1.430	0.2	2.0
CH_3S	p(2×2) tilted	0.25	2.294	0.947	47.9	0.67	0.81	2.313 / 2.446	1.476 / 1.486	18.0	1.7
CH_3S	c(2×2) erect	0.5	1.808	0.461	48.8	-4.06	-3.83	2.319 / 2.324	1.432	0.2	-
CH_3S	c(2×2) tilted	0.5	1.840	0.493	46.5	-3.02	-2.55	2.309 / 2.440	1.513	23.7	-
CH_3S	c(6×2) missing row	0.33	2.207	0.860	39.0	-0.14	-0.16	2.295-2.421	1.359-1.501	7.5 / 3.9	1.7-1.8
CH_3S	p(3×2)	0.33	2.130	0.783	40.2	0.17	0.14	2.300-2.424	1.411-1.539	14.6 / 12.6	1.1-1.6
S	p(2×2)	0.25	4.783	2.196	1.2	0.84	0.84	2.291	1.358	-	0.9
S	c(2×2)	0.5	4.220	1.633	-38.8	-2.00	-2.00	2.272	1.349	-	-
clean surface	(1×1)	-	-	-	83.4	1.21	1.21	-	-	-	-

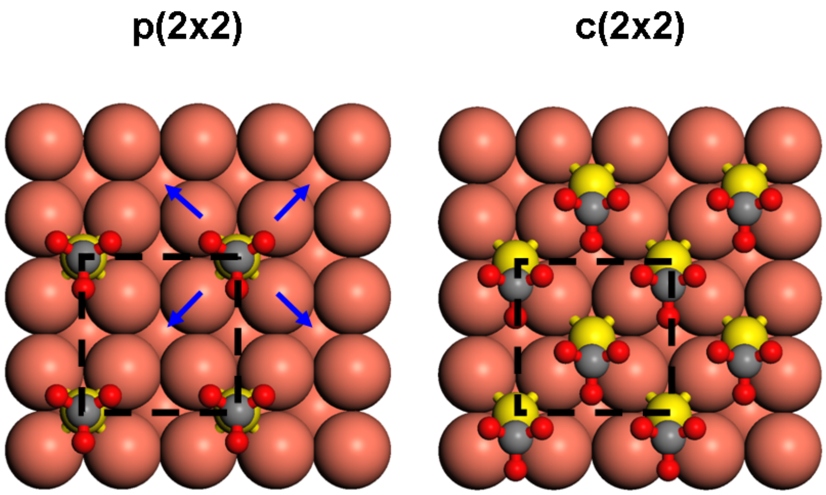

Figure 7.3: Schematic diagrams of lowest energy p(2×2) and c(2×2) adsorbate structures of methanethiolate on Cu(100). Enclosed within the dashed lines are (2×2) unit cells while the blue arrows in the p(2×2) structure show the direction of surface Cu atom relaxation. In the c(2×2) structure the surface layer Cu atoms are pinned by the adsorbates and are therefore unable to relax laterally.

Cu(100)(2×2)-CH_3S is consistent with experimental results, with reported values being around 0.03 Å [193–196]. A possible explanation for this difference between the magnitude of the radial expansion for these two systems is that atomic S is bound more strongly to the Cu(100) surface than CH_3S (E_a = 4.783 eV for S as opposed to E_a = 2.196 eV for CH_3S). This is a accompanied by a shorter equilibrium bondlength to the surface Cu atoms for S (2.29 Å as opposed to 2.35 Å for CH_3S) and may be expected to lead to a correspondingly smaller radial expansion of the underlying Cu. However, the calculation of surface stress presented here allows further insight. The tensile surface stress of the clean Cu(100) surface, a feature which is universally present at clean metal surfaces (see section 2.1.4), is reduced only slightly by adsorption of methanethiolate in the p(2×2) phase, from 1.2 Nm^{-1} to 0.7 Nm^{-1}. Furthermore, this surface stress differs by less than 0.1 Nm^{-1} for the species adsorbed in its erect and tilted form, the erect species being favoured by 30 meV per adsorbate. In contrast, the adsorbate-induced compressive surface stress is much greater in the c(2×2) phase, leading to a large overall *compressive* surface stress of 3.0 and 2.6 Nm^{-1} in the two principle directions for the tilted species. Significantly though, the surface stress is considerably larger, by approximately 1.1 Nm^{-1}, when the adsorbates are erect. This surface stress difference is reflected in the relative surface energy of the high coverage system with methanethiolate adsorbed in its erect and tilted forms, the tilted species being energetically preferred by 32 meV per thiolate in the higher coverage c(2×2) phase.

7.3.3 c(6×2) phase

7.3.3.1 Buckled c(6×2) model

As discussed in section 7.1, two plausible interpretations of the structure of the c(6×2) structure have been suggested, namely a periodic rumpling of a c(2×2) structure and a periodic adsorbate vacancy array, both of which have the potential to provide a surface stress relaxation mechanism not afforded by a c(2×2) structure.

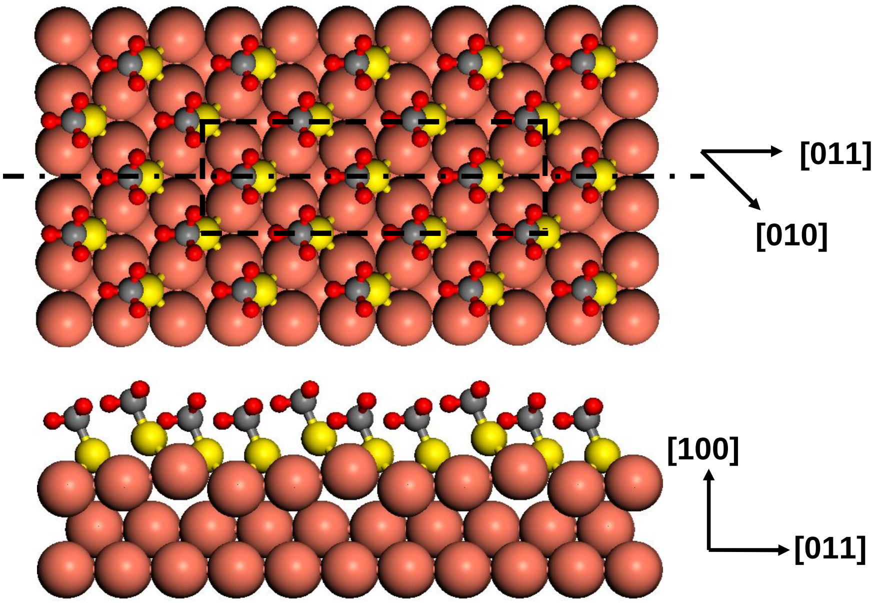

Figure 7.4: Top and side views of one of the starting models considered when searching for a stable rumpled c(2×2) structure for thiolate adsorption on Cu(100). A c(6×2) unit cell is enclosed by the dashed line while the mirror plane of the unit cell is indicated by the dot-dash line.

All attempts to find a stable buckled c(2×2) structure, one of the starting models for which is shown in figure 7.4, failed however; in all cases optimisation of starting structures of this type led to a c(2×2) structure, identical to one of those reported in Table 7.1. Thus it is concluded that the buckled c(2×2) structure can be discounted as a possible model for the experimentally observed c(6×2) phase.

7.3.3.2 Missing row model

Although it was shown in section 7.3.3.1 that a buckled c(2×2) model cannot account for the observed c(6×2) phase of methanethiolate adsorption on Cu(100), there is another plausible model for this phase, proposed by Kondoh et al. [192] and introduced in section 7.1, in which every third thiolate row of a c(2×2) structure is vacant. Shown in Figure 7.5 is the energetically preferred solution of this type, with a reaction energy, as defined in section 7.2, of 860 meV per thiolate. Indeed, this relatively large reaction energy corresponds to a lower surface energy for the system than both the p(2×2) and c(2×2) lowest energy models by 8 meVÅ^{-2}. Although all models were initialised without the imposition of surface symmetry, as shown in Figure 7.5, this particular optimised model *does* contain a mirror plane in the [011] direction. The vacant 4-fold hollows in this missing row structure clearly allow good relief of the surface stress, the two Cu-Cu diagonals under the adsorbed methanethiolate increasing by 1.7% and 1.8%. In contrast to the large compressive stress of the c(2×2) model, the resulting structure exhibits only a very small compressive surface stress of about 0.15 Nm^{-1} in the principle directions. Another interesting feature of this lowest energy model is that consecutive rows of thiolates are tilted in opposite directions, an effect which maximises the physical separation of the methyl head groups. Furthermore, the azimuthal orientation of the methyl head groups, which are rotated by 60° relative to those of the tilted species in the c(2×2) model (see Figure 7.3), also maximises this separation. Indeed, the smallest distance between atomic locations of atoms associated with different thiolates is 2.84 Å for the c(6×2) structure, significantly larger than that found for the c(2×2) structure, 2.17 Å.

A test of the validity of this model can be made by comparing its total energy with that of the lowest energy (3×2) structure with the same adsorbate coverage. As shown in Table 7.1, the surface energy is indeed lower for the c(6×2) structure, by 1.2 meVÅ^{-2}. A likely reason for this is that the surface layer Cu atoms, which in the c(2×2) reconstruction would be bonded to the 'missing' thiolates, can accommodate strain without azimuthally skewing the relative locations of Cu atoms in the two rows under these 'missing' adsorbates.

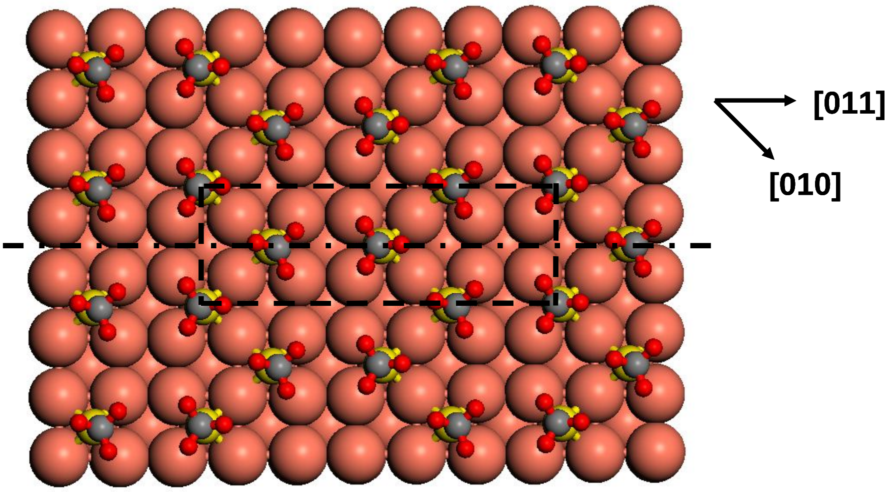

Figure 7.5: The preferred optimised missing row model for the c(6×2) phase of thiolate adsorption on Cu(100), structural parameters for which are presented in Table 7.1. A c(6×2) unit cell is enclosed by the dashed line while the mirror plane of the unit cell is indicated by the dot-dash line.

7.3.3.3 STM images

Since STM images of the thiolate covered surface are available in the open literature, a comparison can be made between these and theoretical STM images of the proposed c(6×2) missing row structure. Figure 7.6 shows three simulated STM images of the missing row structure (upper row of panels), generated using the Tersoff-Hamann approximation (see section 3.3.5), along with two published STM images of the c(6×2) phase (lower row of panels). The simulated images, which are recorded at distances from the outer Cu layer of the surface in the range 5-9 Å, vary substantially in appearance. In the right panel, which shows the image taken closest to the surface, features that have the distinctive triangular shape of the methyl headgroups are clearly displayed. As the distance from the surface increases, however, the bright STM features become circular (centre panel). At even greater distance from the surface, pairs of features begin to merge, creating the appearance of just two larger elliptical features per (6×2) unit cell.

Attempting to describe the real STM images in Figure 7.6 is a much more formidable task, in part due to limited spacial resolution, in part due to the inhomogeneity of the surface. The c(6×2) regions in both images do clearly contain a regular array of two bright features per (6×2) unit cell, which, in itself,

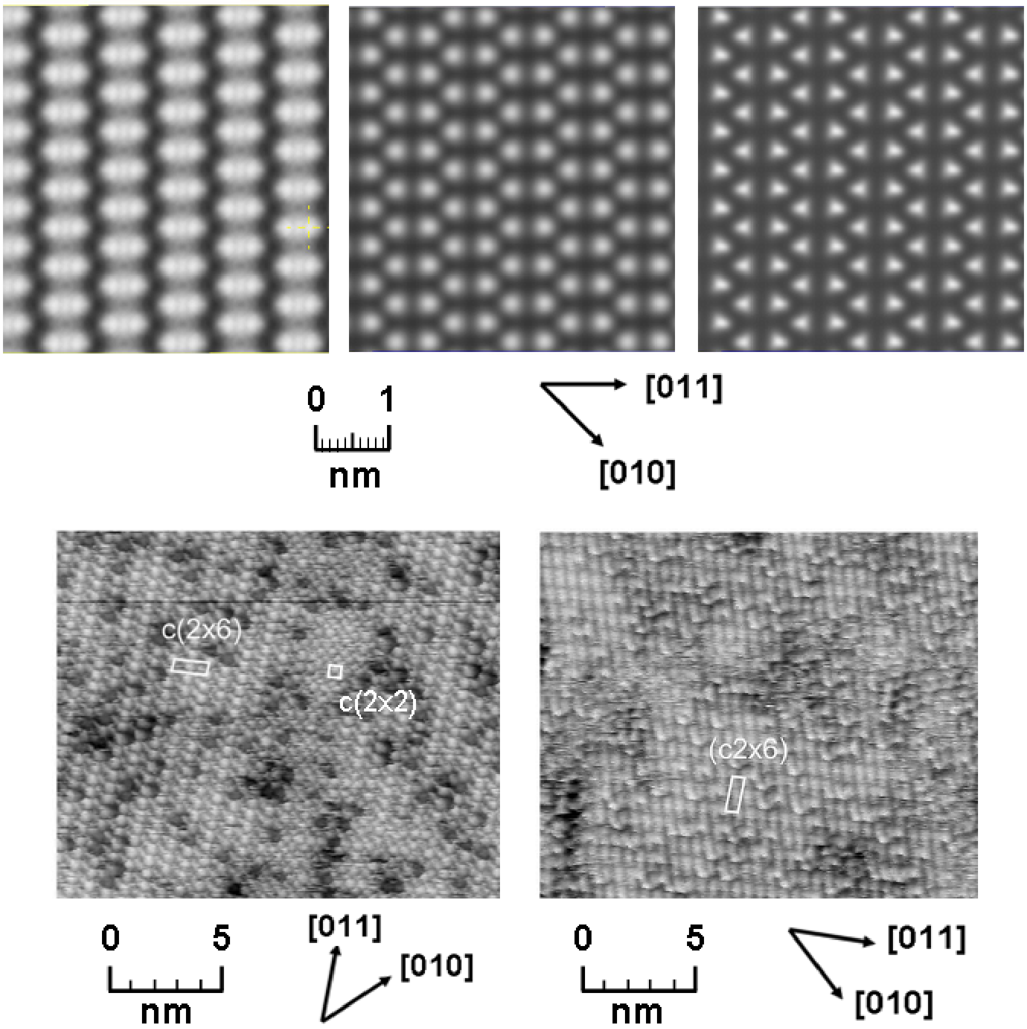

Figure 7.6: Displayed in the upper row of panels are three simulated images of the c(6×2) missing row structure, recorded at decreasing distance from the surface from left to right, at 9 Å, 7 Å and 5 Å. The bias is -0.33 V. The lower row of panels contains two experimental room temperature STM images, published by Driver et al. in reference [198]. Both images show regions of c(6×2) periodicity, one subsequent to adsorption of DMDS (left panel) using a bias voltage of -0.33 V and tunnel current of 1.1 nA, the other following adsorption of methanethiol (right panel) using a bias of -0.25 V and tunnel current of 1.4 nA. In each image a c(6×2) unit cell is enclosed by a solid white line. The lower left image also contains a region of c(2×2) periodicity running down the image, slightly right of centre. A unit cell of this phase is also highlighted in this image.

is consistent with the large-distance simulated image in the upper left panel of the figure. In the lower left panel of Figure 7.6 however, which contains an STM image of the surface recorded during exposure of a clean Cu(100) surface to DMDS, these strong features are approximately circular, in contrast to the elliptical features of the simulated image. In addition, these features are accompanied by the same number of less prominent, elongated features aligned approximately in the [010] direction. Conversely, in the image in the lower right panel of Figure 7.6, recorded following exposure of the clean surface to methanethiolate, the bright features themselves appear to be elongated in the direction of the diagonal of the (6×2) unit cell, and no weaker accompanying features are visible.

What is clear is that the same reconstruction can produce rather varied STM images depending on the conditions, both in the experimental and simulated cases. A further complication in making a direct comparison between the simulated and experimental images comes from the fact that the simulated images are for the optimised ground state structure, whereas the experimental ones consist of a time-averaged representation of the surface at approximately room temperature. In this regard, by observing the number of similar structures found in relatively close proximity to the lowest energy structure and by monitoring the slow convergence of the models, the DFT simulations performed in this work have shown that there is a rather flat energy minima in which the orientation of the thiolates lie. Hence, there will certainly have been significant movement of the methanethiolate species at the temperature at which the experimental images were recorded. Almost freely rotating methyl head groups are likely to lead to rounding and smearing of features in the experimental images, while a changing angle of the S-C bond relative to the Cu surface is likely to result in elongation and further smearing of these features.

An additional feature of sequential STM images of this reaction is the emergence of metastable regions of c(2×2) periodicity, an example of which can be seen in the centre of the lower left image of Figure 7.6, which are subsequently replaced by the c(6×2) phase. In fact, while the adsorption energy per adsorbate is greatest in the p(2×2) reconstruction, and is thus observed at low coverage, as shown in Table 7.1, the c(2×2) reconstruction incorporating the tilted methanethiolate species has a lower surface energy, albeit by just 0.03 eV$Å^{-2}$. In order to transform the surface from the p(2×2) to the c(6×2) reconstruction, it is necessary to relocate 1/3 of the adsorbed methanethiolate species and adsorb an additional 1/3. In contrast, creating the c(2×2) reconstruction from the p(2×2) reconstruction only requires the adsorption of additional methanethiolate species in the four-fold hollows not already occupied. It appears, therefore, that the energy barrier to restructure the surface is sufficient to prevent the immediate emergence of the c(6×2) phase. Interestingly, since the 0.33 ML c(6×2) phase contains a lower adsorbate coverage than the metastable 0.5 ML c(2×2) phase, the local coverage is *lowered* by the restructuring to the c(6×2) phase. This is rather unusual since one normally associates the saturated surface with the phase of highest coverage. In order for this restructuring to occur, c(2×2) regions must either engulf regions of the surface that still exhibit the lower coverage p(2×2) phase or desorption of thiolates must occur, probably as DMDS.

7.3.3.4 Adatom models

Although a c(6×2) model has been found that has significantly lower surface energy than other proposed models of the surface, the agreement between the simulated and experimental STM images is not perfect. While there are plausible reasons why this may be the case (discussed in section 7.3.3.3), it is certainly prudent to explore alternative models. One consideration in this regard is that, rather than adsorbing directly on the clean surface, it is not uncommon for adsorbing species to induce a more complex reconstruction of the surface, whereby the adsorbing species is incorporated within an overlayer structure that also includes substrate adatoms. Indeed, several examples of such reconstructions on Cu are discussed within this thesis (e.g. methoxy on Cu(110) - section 5.1 and methanethiolate on Cu(111) - section 7.4), including the $(\sqrt{17} \times \sqrt{17})$R14° reconstruction of atomic sulphur on Cu(100) alluded to in section 7.1. There is no prior evidence to suggest that the c(6×2) phase is not another example of this kind of reconstruction. Therefore, in an attempt to discover a model with a lower surface energy than that of the c(6×2) missing row model (39.0 eVÅ^{-2}), that may provide an improved fit to the STM images, additional optimisations have been carried out for structures containing Cu adatoms at various values of the coverage.

In the case of a c(6×2) phase, the adatom coverage can take values in increments of 1/6 ML so optimisations were carried out at adatom coverages of 1/6, 1/3, 1/2, 2/3 and 5/6 ML. Additionally the thiolate coverage has been varied between 1/3 ML and 1/2 ML. An attempt was made to start the optimisations in plausible geometries, with all bonding distances at reasonable values. In all cases, however, there was substantial optimisation from these guessed geometries, in general leaving the Cu adatoms close to bulk continuation sites of the substrate.

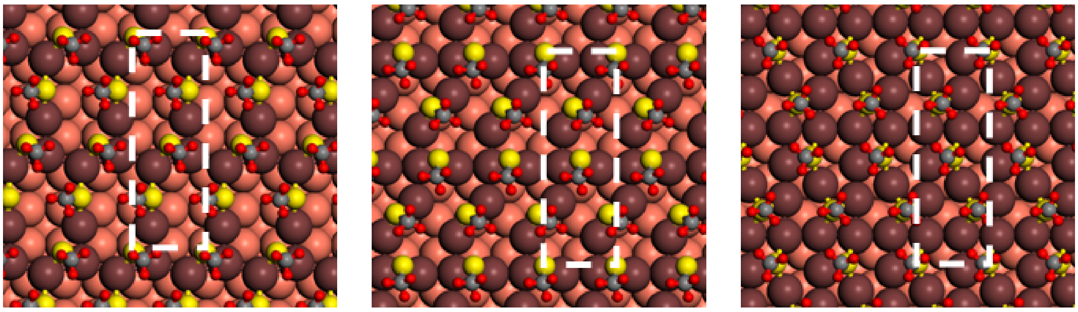

0.5 ML Cu
0.33 ML CH_3S

0.67 ML Cu
0.33 ML CH_3S

0.83 ML Cu
0.33 ML CH_3S

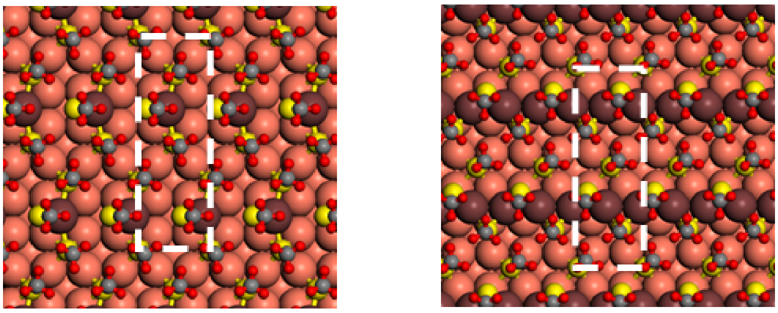

0.16 ML Cu
0.5 ML CH_3S

0.33 ML Cu
0.5 ML CH_3S

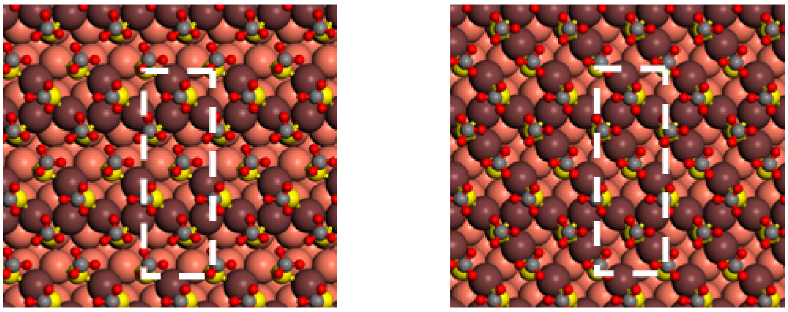

0.5 ML Cu
0.5 ML CH_3S

0.67 ML Cu
0.5 ML CH_3S

Figure 7.7: Cu adatom adsorption models for the c(6×2) reconstruction of methanethiolate adsorption on Cu(100). The Cu adatom and methanethiolate coverages are given below each model. In each image a c(6×2) unit cell is enclosed with the dashed line.

Table 7.2: Surface energies of the most energetically favourable Cu adatom model found for each value of the Cu adatom and thiolate coverage explored for the c(6×2) phase of methanethiolate adsorption on Cu(100).

Cu adatom coverage (ML)	Adsorbate coverage (ML)	γ (meVÅ^{-2})
0.5	0.33	59.9
0.67	0.33	51.3
0.83	0.33	52.7
0.17	0.5	58.2
0.33	0.5	49.0
0.5	0.5	63.2
0.67	0.5	59.5

The surface energies of the most energetically favourable resulting structure for each value of the adatom coverage is presented in Table 7.2. None of these structures have a lower surface energy than the c(6×2) missing row structure. In fact, even the most favourable adatom structure found has an associated surface energy that is 10.0 eVÅ^{-2} greater than this model. Therefore, it is unlikely that adsorption of methane thiolate in any Cu adatom structure will reduce the surface energy of Cu(100) by more than the c(6×2) missing row model.

7.4 Adsorption structure on Cu(111)

7.4.1 Previous work

For methanethiolate adsorption on Cu(111), early NEXAFS [207], SEXAFS [208] and NIXSW [209] results have been used to deduce that a major reconstruction of the surface occurs. By aligning an STM image with the sample orientation (determined by LEED), and with regions of clean surface, Driver et al. concluded that the stable surface comprises a 4.06Å×4.18Å pseudo square overlayer mesh with an included angle of 88.7° [202]. This corresponds to a formal relationsip with the substrate of $\left(\begin{smallmatrix} 4 & 3 \\ 3 & -1 \end{smallmatrix}\right)$.

The proposed one-layer overlayer reconstruction (see Figure 7.2), which incorporates a Cu adatom coverage of 2/3 ML and a thiolate coverage of 1/3 ML, has been shown to be consistent with the increased ion yield detected in a MEIS experiment conducted by Parkinson et al. [203], compared with that of the clean Cu(111) surface prior to depositing DMDS. However, the ion yield in such an experiment comprises a sum of scattering contributions from all surface atoms and the contribution of an individual atom to this yield is affected mainly by the degree of shadowing it experiences from atoms in the vicinity of the path between the atom and the incident ion beam. Since the majority of overlayer atoms comprising the pseudo square mesh are necessarily located far away from continuation sites of the surface (fcc three-fold hollow sites) and thus do not significantly shadow lower substrate atoms, the choice of lateral registry with the substrate was, as expected, found to make no significant difference to the overall yield, and was dependent only on the number of atoms/layers included in the overlayer structure. Therefore, the precise registry of the overlayer Cu atoms with the underlying substrate remained unknown.

More recently, two DFT studies of this system have been undertaken. Ferral et al. considered adsorption of methanethiolate on the clean unreconstructed surface only [206], the saturated phase for which is metastable and is only observed below 173 K [210]. It was concluded that on this surface there is little energetic preference for either hollow site or bridge site adsorption, the exact ordering depending on coverage. In the study of Grönbeck [211], however, it was found that an ordered overlayer reconstruction incorporating 2/3 ML Cu had a lower surface energy than both the most energetically favourable model on the unreconstructed surface, the $(\sqrt{3} \times \sqrt{3})$R30° reconstruction, and another Cu adatom model inspired by the thiolate - Au - thiolate complexes that are believed to exist on the surface following deposition of thiols on Au(111) [212].

7.4.2 Adsorption on clean Cu(111)

While the focus of this investigation was to explore the structure of the overlayer reconstruction formed by methanethiolate on Cu(111), in order to compare with previous DFT studies of this system and to consider the functional dependency of the results, initial calculations were performed for adsorption on the unreconstructed Cu(111) surface. Table 7.3 provides a comparison of the results of the present DFT calculations with those of previous DFT studies for adsorption for this system, both in the low coverage p(2×2) phase and higher coverage $(\sqrt{3} \times \sqrt{3})$R30° phase (see Figure 7.8). In both cases, the adsorption energy value found in the present study is significantly smaller than those of the other studies. These differences can be ascribed to the different choice of functional used; the RPBE functional typically underbinds relative to the PBE functional (see section 3.1.4). Nevertheless, the adsorption structures compare favourably with those found in previous DFT studies, all bond lengths at variance with one or both previous studies by less than 0.01 Å. Furthermore, the surface energy of

Table 7.3: Adsorption energy, surface energy change due to adsorption - $\Delta\gamma$, and selected structural parameters for methanethiolate adsorbed in the p(2×2) and $(\sqrt{3} \times \sqrt{3})$R30° phases on the unreconstructed Cu(111) surface.

Phase	p(2×2)		$(\sqrt{3} \times \sqrt{3})$R30°		
Study	present	Ferral et al. [206]	present	Ferral et al. [206]	Grönbeck [211]
Functional	RPBE	PBE	RPBE	PBE	PBE
E_a (eV)	1.932	2.838	1.833	2.433	not reported
$\Delta\gamma$ (meVÅ^{-2})	-25.3	not reported	-28.1	not reported	-44
S-Cu (Å)	2.297	2.298	2.301	2.298	2.27
[S-Cu]$_z$ (Å)	1.960	not reported	1.813	not reported	1.86
S-C (Å)	1.845	1.850	1.846	1.847	1.85
S-C tilt (°)	47.2	45.05	29.5	36.12	42

the $(\sqrt{3} \times \sqrt{3})$R30° reconstruction is 2.8 meVÅ^{-2} lower than that of the p(2×2) phase, in agreement with the experimental observation of the $(\sqrt{3} \times \sqrt{3})$R30° phase at saturation coverage at low temperature [210].

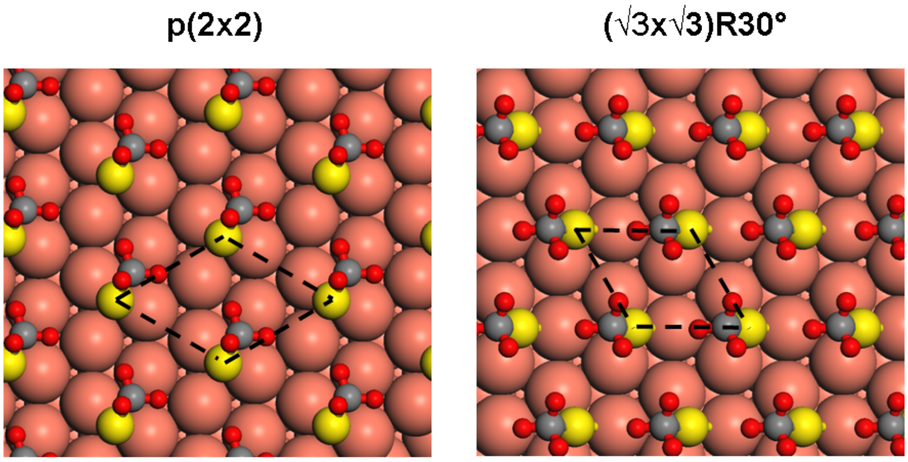
p(2x2)

(√3x√3)R30°

Figure 7.8: Schematic diagrams of lowest energy p(2×2) and $(\sqrt{3} \times \sqrt{3})$R30° adsorbate structures for methanethiolate adsorption on Cu(111). For each structure a primitive unit cell is enclosed within the dashed line.

7.4.3 Overlayer models

Although the $(\sqrt{3} \times \sqrt{3})$R30° phase shown in Figure 7.8 is stable on the clean surface at low temperature, this phase is, in fact, only metastable. As discussed in section 7.4.1, at temperatures greater than 173 K a reconstruction occurs to a larger mesh, believed to have a formal relationship with the substrate of $\begin{pmatrix} 4 & 3 \\ 3 & -1 \end{pmatrix}$ (see Figure 7.2). STM images of this phase (an example is shown in Figure 7.10) display five bright features per unit cell that are arranged in a pseudo square array, suggesting that the surface reconstruction includes five methanethiolate species per unit cell. Based upon these images, it has also been inferred [202] that the outer layer of the Cu surface has reconstructed likewise to form a pseudo square array, incorporating 10 Cu atoms per unit cell, such that all S head groups are four-fold coordinated to Cu adatoms in a pseudo c(2x2) overlayer mesh. This assumption has been supported by a MEIS investigation of this system as discussed in section 7.4.1. However, recent DFT calculations performed by Grönbeck [211] have shown that, while this phase is preferred energetically over the $(\sqrt{3} \times \sqrt{3})$R30° phase, the Cu adatoms of the reconstructed outer layer do not, in fact, form a simple pseudo square mesh as anticipated. Optimisation of such a structure resulted in these atoms being displaced far from their starting locations, rendering some of the thiolates undercoordinated to the surface relative to the four-fold coordination in the pseudo square model of Figure 7.2. Such a structure can no longer be guaranteed to provide a regular pseudo square array of features in an STM image, nor can it be guaranteed to provide the same ion yield as the previously proposed pseudo square mesh in a MEIS experiment. Thus it is no longer valid to assume that the $\left(\begin{smallmatrix} 4 & 3 \\ 3 & -1 \end{smallmatrix}\right)$ overlayer should contain 10 Cu atoms per unit cell.

7.4.3.1 Structural optimisations

In order to explore the possible structures that could comprise the overlayer reconstruction of methanethiolate on Cu(111), three independent optimisations were carried out initially, starting from a pseudo-square Cu adatom / methanethiolate overlayer (10 Cu + 5 CH_3S) with differing lateral registry to the underlying Cu(111) substrate. In all cases, the same optimised structure resulted, albeit with small alterations due to methyl group rotations and, in some cases, with 180° rotation of the overlayer relative to the substrate (thereby exchanging fcc and hcp sites). The total energy of each of these structures was within 11 meV of the most energetically favourable structure incorporating 10 Cu adatoms, model Ad10 in Figure 7.9. An additional optimisation was carried out starting from a modified version of Ad10 where the 5 thiolate species had been moved laterally by approximately 4 Å. Once again, starting from this incredibly unfavourable initial configuration, the structure returned to the same model, Ad10. It is quite likely, therefore, that the most favourable configuration for an overlayer containing 10 Cu adatoms and 5 thiolates has been found. This is the same qualitative struc-

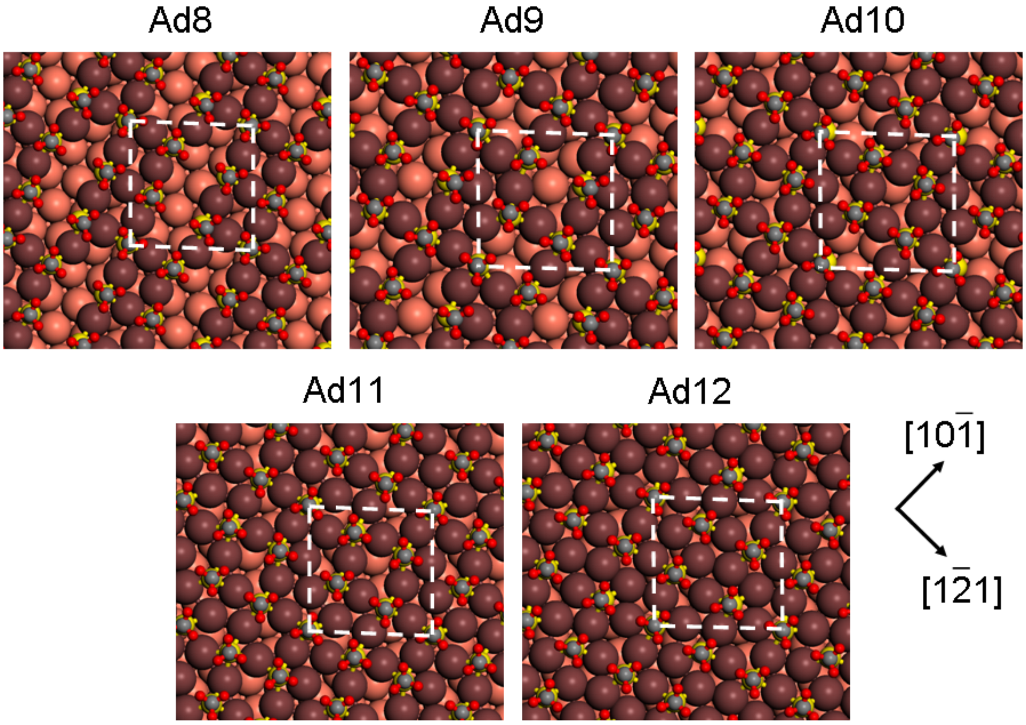

Figure 7.9: Schematic diagrams of the lowest surface energy Cu adatom overlayer adsorbate structures found for methanethiolate on Cu(111) incorporating 8 - 12 Cu adatoms. In each image a unit cell is enclosed within the dashed line.

ture as that found by Grönbeck [211]. In the present study the surface energy for this model is calculated to be 2.5 meVÅ^{-2} smaller than that found for the $(\sqrt{3} \times \sqrt{3})$R30° reconstruction on the clean surface. This is in perfect agreement with Grönbeck who published a corresponding value of 3 meVÅ^{-2}.

While the low surface energy calculated for model Ad10 does suggest that reconstruction to this overlayer structure is physically plausible, it does not rule out the existence of more favourable overlayer structures, incorporating a different number of Cu adatoms. In order to explore this possibility, many additional models have been optimised that incorporate between 8 and 12 Cu adatoms and 5 methanethiolate adsorbates. The surface energy change due to adsorption of DMDS of the most favourable structure for each value of the adatom coverage is included in Table 7.4, the corresponding structures for which are represented schematically in Figure 7.9. In most cases there is a strong preference for Cu adatom adsorption close to 3-fold hollow sites, but neither this tendency nor the differing number of Cu atoms included induces a significant disturbance to the relative locations of the thiolate species. This suggests that there may be a strong repulsive interaction between the methyl groups inhibiting them from residing closer together. In fact, all of the models shown in Figure 7.9 apart from Ad12 are energetically preferable to the $(\sqrt{3} \times \sqrt{3})$R30° reconstruction (see Table 7.4). Moreover, the energetic similarity of these models suggests that the surface is likely to be comprised of a combination of these, and other low energy structures, depending on the local availability of Cu adatoms. Additional optimised models incorporating between 5 and 7 Cu adatoms (not shown) were found to have a significantly larger associated surface energy however, suggesting that 8/15 ML Cu adatoms may be a lower bound for the Cu adatom coverage.

Since the low energy models shown in Figure 7.9 vary in the number of occupied three- and four- fold coordinated adsorption sites, the energetic similarity of the models also suggests that there is little energetic difference between three-fold and four-fold coordinated thiolate adsorption. However, in all cases the interatomic spacing between the overlayer Cu adatoms bonded to thiolates is significantly larger than on the unreconstructed Cu(111) surface. Indeed, thiolate adsorption on the unreconstructed Cu(111) surface in the $(\sqrt{3} \times \sqrt{3})$R30° phase induces an average increase of 2.2 % for the separation of Cu atoms bonded to the same thiolate, corresponding to a lateral atomic strain of 0.03 Å away from bulk continuation sites.

Table 7.4: Surface energy change due to adsorption, $\Delta\gamma$, and the difference in height of the C atoms above the surface, Δh_C, for the low energy structures shown in Figure 7.9 for the methanethiolate adsorption induced reconstruction on Cu(111).

Model	Cu adatom coverage ML	$\Delta\gamma$ (meV)	Δh_C (Å)
Ad8	0.53	-30.9	0.16
Ad9	0.6	-29.5	0.25
Ad10	0.67	-30.6	0.11
Ad11	0.73	-29.8	0.08
Ad12	0.8	-24.1	0.14

7.4.3.2 STM images

An interesting feature of the various overlayer models is the small variation, Δh_C in Table 7.4, of the height above the surface of the C atoms of the thiol groups. At most this variation is 0.25 Å, in model Ad9, but in most cases is significantly smaller. Features associated with the thiol groups in STM images can thus be expected to be of similar intensity. As is the case for methanethiol adsorption on Cu(100), discussed in Section 7.3, published images of the thiolate covered Cu(111) surface have been made available in the open literature. Therefore, a direct comparison can be made between these and simulated STM images of the most energetically favourable overlayer structures found in this investigation. The simulations have been performed for the two most favourable overlayer structures, Ad8 and Ad10. These simulated images are presented in Figure 7.10 alongside a real STM image published by Driver et al. [202].

The main aspect of the real image, the pseudo square arrangement of bright features, is well replicated in the simulated images of both models. However, while there are certainly differences in the intensity of the features in the experimental image, the periodic variations in intensity and shape of the features in the simulated images do not appear to be present in the real image. As reported in section 7.4.3.1, several models were optimised with 10 Cu adatoms included. Each of these returned the same qualitative optimised structure, but with differing methyl group rotations. Since all of these structures returned an energy within 11 meV of the most favourable structure, the DFT calculations suggest that there is only a small energetic cost of rotating at least some of the methyl head groups. Therefore, the STM images of Driver et al. are likely to consist of a time averaged representation of rapidly rotating methyl groups. This effect is not replicated in the simulated STM images of Figure 7.10. Therefore, some

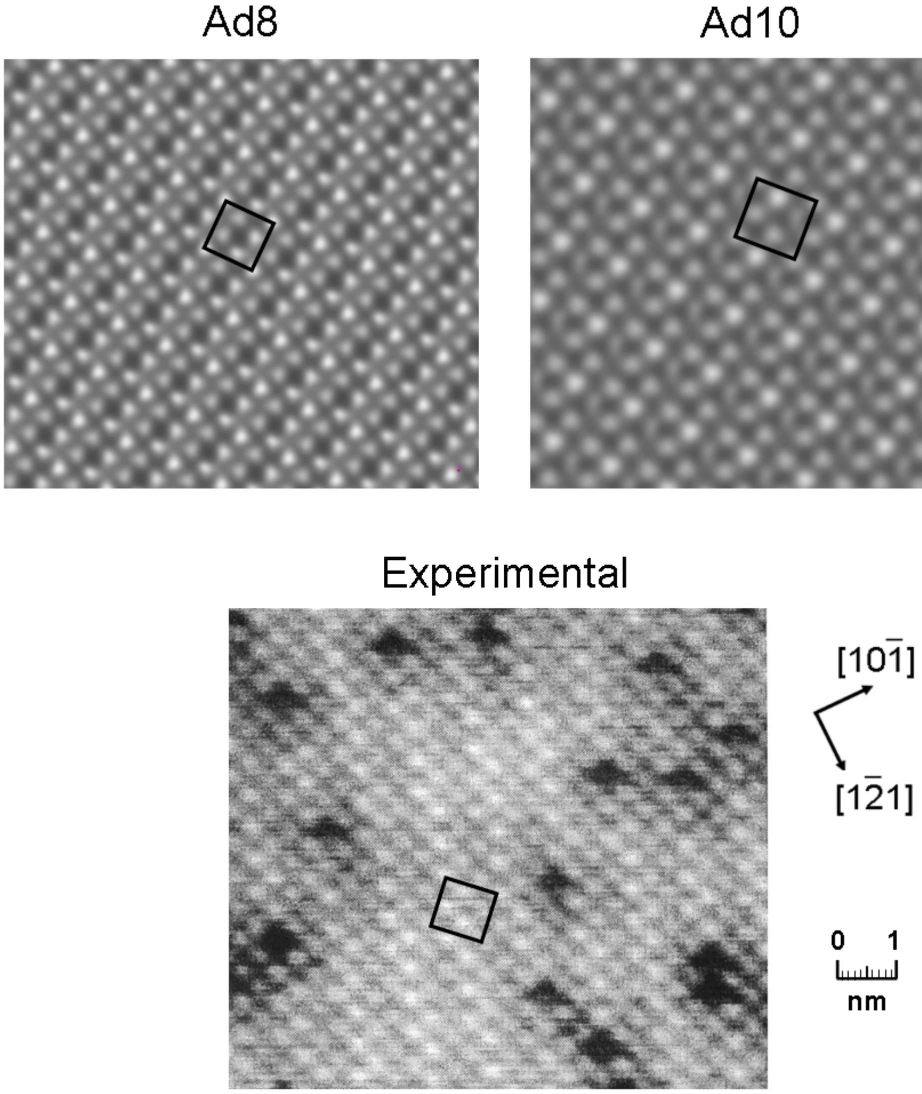

Figure 7.10: Simulated STM images of the two lowest surface energy overlayer models, Ad8 and Ad10, taken approximately 7.5 Å from the surface, and a real room temperature STM image, recorded by Driver et al. [202], of adsorbed methanethiolate on Cu(111). The experimental image was recorded using a bias of -0.27 V and tunnel curent of 1.2 nA. In each image a $\left(\begin{smallmatrix}4 & 3\\ 3 & -1\end{smallmatrix}\right)$ unit cell is enclosed by a solid black line.

smearing / rounding of the simulated STM features is to be expected and could be accountable for these variations in feature intensity.

The fact that there are multiple overlayer models with similar surface energy allows a further plausible interpretation of the image. If the surface is indeed comprised of a variety of overlayer models with a high phase boundary density, the apparent pseudo square periodic array of bright features may arise because of strong repulsive interactions between thiolates, similar to those believed to account for the thiolate tilting in the c(6×2) reconstruction of methanethiolate on Cu(100) (see section 7.3.3.2), keeping the thiolates rigidly spaced and not, as previously proposed, due to the entire structure being periodic. In this case, the Cu overlayer can be thought of as providing a sea of atoms above which the thiolates can find the best possible separation, the competing factors being energy reduction through increased density of thiolates and energy increase due to electrostatic repulsion between them.

7.4.3.3 MEIS reevaluation

Using scattering simulations, Parkinson et al. have determined that a pseudo square overlayer mesh such as that shown in Figure 7.2 is compatible with the MEIS data collected for methanethiolate adsorption on Cu(111) [203]. However, the DFT calculations presented here demonstrate that, in reality, a regular pseudo square Cu adatom arrangement is not plausible on energetic grounds. Rather, the Cu adatoms are strongly drawn towards hollow sites during geometry optimisation, most of these atoms ending up very close to these high symmetry sites in the final structures. The histogram in Figure 7.11 provides a visual comparison of the lateral atomic displacements from hollow/ bulk continuation sites of the Cu adatoms contained within the unit cell for the low energy structures shown in Figure 7.9. In all cases a significant proportion of the overlayer Cu atoms lie within 0.24 Å of hollow sites. Moreover, for models Ad10 and Ad11, over half of the overlayer Cu atoms reside within this distance. This can be expected to significantly increase shadowing of lower atomic layers, thus reducing the overall ion yield.

To determine the magnitude of this effect, additional multiple scattering simulations have been conducted by Daniel Sheppard at the University of Warwick for both incident beam direction in which data has been recorded (see Figure 7.11). All of the models shown in Figure 7.9 result in a smaller associated ion yield than that of the originally proposed pseudo square reconstruction shown in

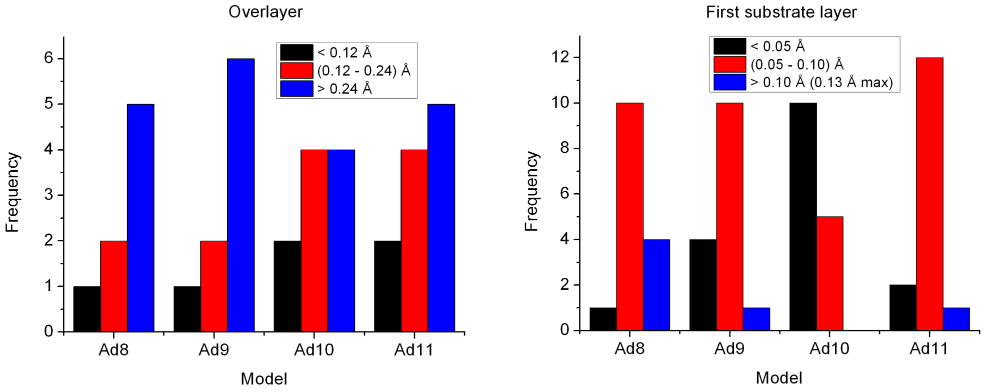

Figure 7.11: Histograms of the lateral shifts of Cu adatoms in the overlayer {first substrate} layer from 3-fold hollow {bulk continuation} sites for the low energy overlayer structures shown in Figure 7.9.

Figure 7.2. Nevertheless, there is still a significant increase in yield relative to that from the clean surface and the shadowing dip positions, which result from blocking of the outgoing beam, remain largely unchanged.

A demonstration of the sensitivity of the MEIS technique to atomic displacements of the overlayer atoms can be seen by noticing that models Ad8 and Ad11 have very similar MEIS yields, even though Ad11 contains 3 additional atoms in the overlayer. The reason for this can be seen clearly in Figure 7.11 which shows that Cu atoms are typically displaced further from hollow / bulk continuation sites, particularly those in the first substrate layer. Bearing in mind this sensitivity, several attempts have been made to determine the source of the discrepancy between the real and simulated MEIS yields. These include adding more unconstrained substrate layers in the DFT calculations and optimising the models using a very small maximum force tolerance (see equation 3.14) of 0.005 eVA^{-1}. However, neither of these attempts resulted in a significant change to the yield.

Another plausible reason for the difference in overall yield could be the choice of vibrational amplitude enhancement, which is typically in the range 30-40 % [213], of the overlayer Cu atoms. However, it was found that this enhancement would need to be greater than 100 % in order to account fully for the discrepency, a value which is thought to be unrealistic [213]. Since there are a number of structures with similar corresponding surface energies, one further possible reason for this discrepency is that the surface, as suggested in section 7.4.3.1, is likely to comprise many different structures and have a high phase boundary density.

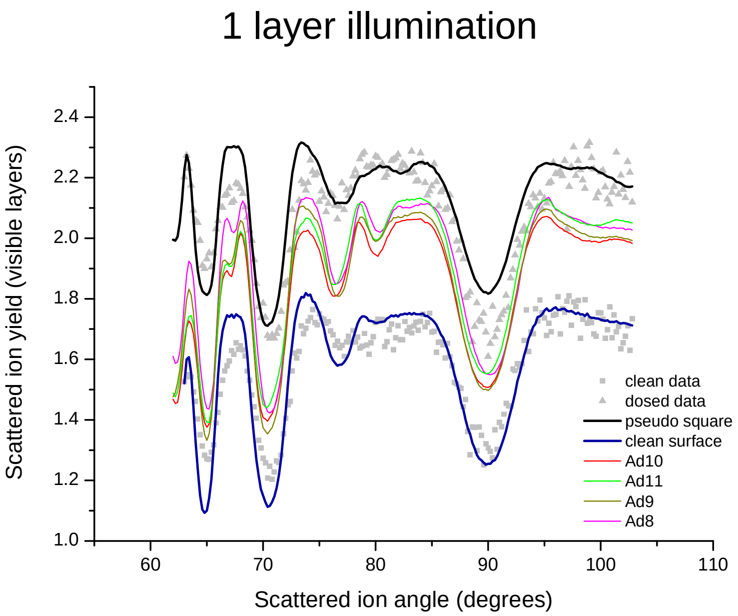
1 layer illumination

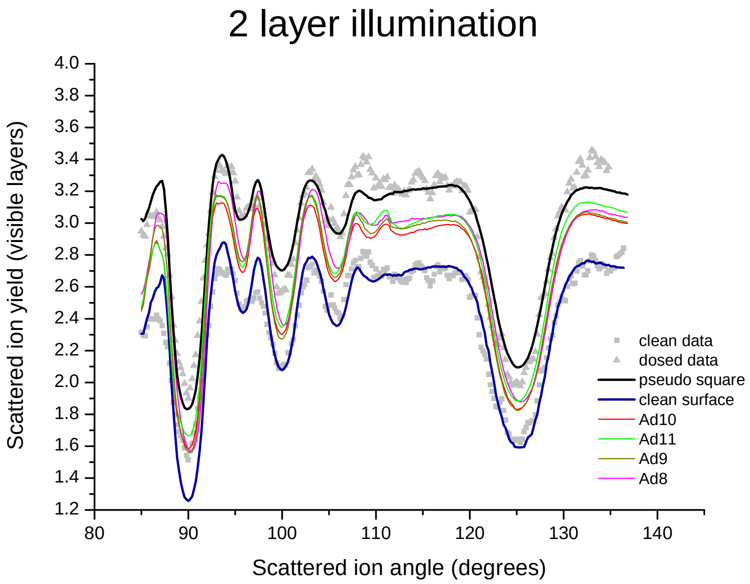
2 layer illumination

Figure 7.12: Comparison of experimental MEIS spectra with spectra obtained from multiple scattering simulations, performed by Daniel Sheppard, for the energetically favourable overlayer models of the structure of the methanethiolate/Cu(111) system. The 1 and 2 layer illuminations correspond to the two different incident ion beam directions for which data has been recorded. Note the y-axis has a different scale in the two plots.

This may mean that many more Cu adatoms lie further from hollow sites, leading to increased ion yield.

7.5 Conclusions

In this chapter the results from DFT calculations have been presented that have been used to explore the adsorption structure of methane thiolate on Cu(100) and Cu(111). On Cu(100), while the agreement between simulated and real STM images is not perfect, energetic considerations suggest that thiolates are incorporated in a c(6×2) reconstruction with an adsorbate coverage of 2/3 ML. In contrast, for methanethiolate adsorbed on Cu(111), several overlayer models have been found with lower surface energy than is possible for adsorption on the unreconstructed surface. One may expect several of these phases, and others, to be present on the surface, the local structure depending on the availability of Cu adatoms.

Surface stress plays a clear role in the Cu(100)/methanethiolate system. The c(2×2) reconstruction has a large associated compressive surface stress of -3 Nm^{-1}, a tilted species being realised that reduces the surface stress by 1 Nm^{-1}. In contrast, the compressive surface stress is much smaller for the c(6×2) missing row structure (0.15 Nm^{-1}), the missing rows allowing good relief of surface stress. A common theme throughout this study, however, is the large energetic penalty for adsorbates being close together. Indeed, this is apparent in the c(6×2) missing row model on Cu(100) (see Figure 7.5), thiolates in adjacent rows having opposite tilt angle, and also in the overlayer models for adsorption on Cu(111) where adsorbates maintain a pseudo square array even though the underlying Cu adatoms are far from the simple pseudo square arrangement predicted on the basis of STM and MEIS results.

The surface energy change upon adsorption also provides a comparison between the relative stability of adsorption of DMDS on the two adsorption systems studied in this chapter. On the Cu(100) surface, this energy change is -44.4 eVÅ^{-1} as opposed to -30.9 eVÅ^{-1} for adsorption on Cu(111). As discussed in section 2.1.1, it is common for the (100) of metal surfaces to be more reactive than the (111) surface of fcc metals. In this case, the particularly small surface energy change due to adsorption of -28.1 eVÅ^{-1} for the unreconstructed Cu(111) surface, compared to that for the unreconstructed Cu(100) surface, has proved to be a driving force for reconstruction to a more (100) type overlayer structure.

Chapter 8

Concluding remarks

Contained within this thesis are several demonstrations of the power of DFT, and its implementation in CASTEP, as a tool for studies of surface structure and surface stress. It is interesting to compare the variety of adsorbate systems explored within this thesis. It was long thought that metal surfaces maintained a rigid chequerboard during heterogeneous catalytic reactions. This is qualitatively the case for the adsorption and decomposition of furan discussed in chapter 4.1 and also for cytosine adsorption on Cu(110) in section 5.2 and methanethiolate adsorption on Cu(100) in section 7.3. However, it is now accepted that this simple picture is not always correct. Indeed, there are multiple examples contained within this thesis where metal adatoms are involved in the surface structure and thus play a major role in related surface reactions. While the steady-state reaction rate of formaldehyde synthesis from methanol is very slow on the clean Cu(110) surface, it is much faster in the presence of oxygen. In this case, methanol interacts with areas of O(2×1) reconstruction to induce a substantial reconstruction of the surface, with 4 methoxy species and 4 Cu adatoms being incorporated within the (5×2) unit mesh. In the case of methanethiol adsorption on Cu(111), a complex overlayer reconstruction exists which is likely to comprise domains of varying structure, depending on the local availability of Cu adatoms. Moreover, the Ir(100) surface reconstructs in the absence of external species, and can be further reconstructed by exposure to H.

The success of the joint experimental / theoretical investigations reported within this thesis has been impressive. For both cytosine adsorption on Cu(110) and methoxy adsorption on Cu(110), the combined results from PhD and DFT were necessary to derive full solutions for the long range ordered structures, the resulting bondlengths found by the two approaches agreeing within 0.1 Å. Similarly, it was this combined analysis that allowed an informed prediction to be made for the structure of the C_3H_3 species thought to result from furan decomposition on Pd(111). The complementary MEIS and DFT results presented in chapter 7 have allowed a good understanding of the surface strain and stress induced by methanethiol adsorption on Cu(100) and also of the possible reconstruction models for methanethiol adsorption on Cu(111). Furthermore, excellent agreement has been found between surface stress change measurements for H adsorption on Ir(001) and those obtained using DFT calculations.

In several studies contained within this thesis, and others completed during my PhD, multiple common functionals have been used in order to provide a comparison between results obtained by them and the accuracy of these results with respect to those obtained using experimental techniques. A common theme throughout many of these studies has been an underestimation of bond strength and bond length when using the RPBE functional, in spite of the fact that this functional has been claimed to provide accurate results for adsorption of small molecules on metals [73]. A further accompanying drawback of the RPBE functional, which is particularly apparent in systems where adsorbate-substrate bonding is weak, is that the functional also underbinds, thus having a detrimental effect on the calculation of adsorption and surface energies. While calculations performed using the LDA functional typically result in overbinding, thus suffering from the opposite problem, it does appear that the PW91 and PBE functionals are more appropriate for structural studies involving small organic molecules on metal surfaces. It should be noted, however, that van der Waals interactions are not explicitly included in GGA functionals and inclusion of this interaction within the RPBE functional may improve the bonding characteristics to metal surfaces.

The emergence of DFT as a framework for conducting computationally feasible first-principles simulations has revolutionised the way in which not only surface science but condensed matter studies in many fields are conducted. Most experimentally measurable properties of condensed matter can now be calculated with good accuracy using DFT, but there is still much work to do to improve the theory. For example, most studies still consider the ground state of a system only and temperature dependent DFT theory is still lagging behind. The search for a universally applicable exchange-correlation functional is also unresolved. Indeed, there is a plethora of available functionals contained within the literature, all of which claim to be useful in one or several classes of calculations. Unfortunately, this makes it difficult in many cases to compare directly between results reported in different studies. Furthermore, much work is still to be done to find a computationally efficient way to describe van der Waals interactions. Some advancements have recently been made in this area however, the emergence of DFT-D corrections being a good example.

Bibliography

[1] D. P. Woodruff, *J. Phys. Condens. Matter*, 2010, **22**, 084016.

[2] J. C. Vickerman and I. S. Gilmore, *Surface Analysis - The Principle Techniques*, Wiley, 2011.

[3] D. P. Woodruff and D. L. Delchar, *Modern Techniques of Surface Science (2nd Edition)*, Cambridge University Press, 1994.

[4] H. Ibach, *Surf. Sci. Rep.*, 1999, **35**, 71.

[5] D. Sander, Z. Tian, and J. Kirschner, *J. Phys. Condens. Matter*, 2009, **21**, 134015.

[6] D. Sander, H. L. Meyerheim, Z. Tian, L. Niebergall, N. N. Negulyaev, K. Mohseni, V. S. Stepanyuk, R. Felici, and J. Kirschner, *Phys. Rev. B*, 2010, **81**, 153403.

[7] D. Sander, *Curr. Opin. Solid State Mater. Sci.*, 2003, **7**, 51.

[8] M. K. Bradley, J. Robinson, and D. P. Woodruff, *Surf. Sci.*, 2010, **604**, 920.

[9] M. K. Bradley, D. A. Duncan, J. Robinson, and D. P. Woodruff, *Phys. Chem. Chem. Phys.*, 2011, **13**, 7975.

[10] M. K. Bradley, D. Kreikemeyer-Lorenzo, W. Unterberger, D. A. Duncan, T. J. Lerotholi, J. Robinson, and D. P. Woodruff, *Phys. Rev. Lett.*, 2010, **105**, 086101.

[11] D. Kreikemeyer-Lorenzo, M. K. Bradley, W. Unterberger, D. A. Duncan, T. J. Lerotholi, J. Robinson, and D. P. Woodruff, *Surf. Sci.*, 2011, **605**, 193.

[12] D. C. Jackson, D. A. Duncan, W. Unterberger, T. J. Lerotholi, D. Kreikemeyer-Lorenzo, M. K. Bradley, and D. P. Woodruff, *J. Phys. Chem. C*, 2010, **114**, 15454.

[13] M. K. Bradley, J. Robinson, and D. P. Woodruff, *Phys. Rev. B*, 2011, **84**, 075438.

[14] J. W. Gibbs, *The scientific papers of J. Willard Gibbs: volume 1*, London: Longmans-Green, 1906.

[15] J. M. Zhang, F. Ma, and K. W. Xu, *Appl. Surf. Sci.*, 2004, **229**, 34.

[16] B. C. Allen and W. D. Kingery, *Trans. Metal. Soc. AIME*, 1959, **215**, 30.

[17] B. C. Allen, *Trans. Metal. Soc. AIME*, 1963, **227**, 1175.

[18] D. Germer and H. Mayer, *Z. Phys.*, 1968, **210**, 391.

[19] H. Udin, A. J. Shaler, and J. Wulff, *Trans. AIME*, 1949, **185**, 186.

[20] J. W. Obreimoff, *Proc. R. Soc. London*, 1930, **127**, 290.

[21] R. Smoluchowski, *Phys. Rev.*, 1941, **60**, 661.

[22] J. N. Andersen, H. B. Nielsen, L. Petersen, and D. L. Adams, *J. Phys. C: Solid State Phys.*, 1984, **17**, 173.

[23] J. Friedel, *Phil. Mag.*, 1952, **43**, 153.

[24] J. E. Inglesfield, *Prog. Surf. Sci.*, 1985, **20**, 105.

[25] G. P. Srivastava, *Theoretical modelling of semiconductor surfaces: Microscopic studies of electrons and phonons*, World scientific publishing, 1999.

[26] L. Fishwick, M. Walker, M. K. Bradley, D. P. Woodruff, and C. F. McConville, *Phys. Rev. B*, 2012, **85**, 045322.

[27] C. Elschenbroich and A. Salzer, *Organometallics: A Concise Introduction (2nd Edition)*, Wiley-VCH, 2006.

[28] R. Shuttleworth, *Proc. Phys. Soc.*, 1950, **63**, 444.

[29] K. Kádas, Z. Nabi, S. K. Kwon, L. Vitos, R. Ahuja, B. Johansson, and J. Kollár, *Surf. Sci.*, 2005, **600**, 395.

[30] Z. Y. Yang, Z. Q. Wang, and Y. P. Zhao, *Int. J. Nonlinear Sci. Numer. Simul.*, 2008, **9**, 323.

[31] H. Ibach, *Physics of surfaces and interfaces*, Springer, 2006.

[32] Z. Tian, D. Sander, N. Negulyaev, V. S. Stepanyuk, and J. Kirschner, *Phys. Rev. B*, 2010, **81**, 113407.

[33] H. Ibach, *Surf. Sci.*, 1997, **29**, 193.

[34] R. J. Needs and M. Mansfield, *J. Phys. Condens. Matter*, 1989, **1**, 7555.

[35] P. J. Feibelman, *Phys. Rev. B*, 1997, **56**, 2175.

[36] W. Haiss, *Rep. Prog. Phys.*, 2001, **64**, 591.

[37] K. Takayanagi, Y. Tanishiro, M. Takahashi, and S. Takahashi, *J. Vac. Sci. Technol. A*, 1985, **3**, 1502.

[38] S. Hagstrom, H. B. Lyon, and G. Samorjai, *Phys. Rev. B*, 1965, **15**, 491.

[39] D. G. Fedak and N. A. Gjonstein, *Phys. Rev. Lett.*, 1966, **16**, 171.

[40] K. Heinz, G. Schmidt, L. Hammer, and K. Müller, *Phys. Rev. B*, 1985, **32**, 6214.

[41] E. Vlieg and I. K. Robinson, *Surf. Sci.*, 1990, **233**, 248.

[42] P. R. Watson, M. A. V. Hove, and K. Hermann, Nist surface structure database ver. 5.0, 2003.

[43] D. Woodruff and A. Bradshaw, *Rep. Prog. Phys.*, 1994, **57**, 1029.

[44] D. P. Woodruff, *Surf. Sci. Rep.*, 2007, **62**, 1.

[45] J. Stöhr, *NEXAFS spectroscopy*, Springer, 1992.

[46] G. R. Bell - private communication.

[47] M. Born and J. R. Oppenheimer, *Annalen der Physik*, 1927, **389**, 457.

[48] W. Kohn and L. J. Sham, *Phys. Rev.*, 1965, **140**, A1133.

[49] P. Hohenberg and W. Kohn, *Phys. Rev.*, 1964, **136**, B864.

[50] S. Redner, *Phys. Today*, 2005, **58**, 49.

[51] D. S. Sholl and J. A. Steckel, *Density functional theory: A practical introduction*, Wiley, 2009.

[52] M. C. Payne, M. P. Teter, D. C. Allan, T. A. Arias, and J. D. Joannopoulos, *Rev. Mod. Phys.*, 1992, **64**, 1045.

[53] N. Marzari, D. Vanderbilt, and M. C. Payne, *Phys. Rev. Lett.*, 1997, **79**, 1337.

[54] G. Kresse and J. Furthmüller, *Phys. Rev. B*, 1996, **54**, 11169.

[55] P. Pulay, *Chem. Phys. Lett.*, 1980, **73**, 393.

[56] C. G. Broyden, *Math. Comp.*, 1965, **19**, 577.

[57] M. Methfessel and A. T. Paxton, *Phys. Rev. B*, 1989, **40**, 3616.

[58] H. Hellmann, *Einführung in die Quantenchemie*, Leipzig: Franz Deuticke, 1937.

[59] R. P. Feynman, *Phys. Rev.*, 1939, **56**, 340.

[60] R. G. Parr and W. Yang, *Density-Functional Theory of Atoms and Molecules*, Oxford University Press, 1994.

[61] M. Gell-Mann and K. A. Brueckner, *Phys. Rev.*, 1957, **106**, 364.

[62] W. J. Carr, *Phys. Rev.*, 1961, **122**, 1427.

[63] D. M. Ceperley and B. J. Alder, *Phys. Rev. Lett.*, 1980, **45**, 566.

[64] S. H. Vosko, L. Wilk, and M. Nusair, *Can. J. Phys.*, 1980, **58**, 1200.

[65] J. P. Perdew and A. Zunger, *Phys. Rev. B*, 5048, **23**, 5048.

[66] S. J. Clark In *CASTEP Workshop, University of York*, 2007.

[67] R. O. Jones and O. Gunnarsson, *Rev. Mod. Phys.*, 1989, **61**, 689.

[68] J. P. Perdew and Y. Wang, *Phys. Rev. B*, 1992, **45**, 13244.

[69] J. Perdew, K. Burke, and M. Ernzerhof, *Phys. Rev. Lett.*, 1996, **77**, 3865.

[70] T. Reuters, *Web of Knowledge online journal database*, accessed 08/11/2011.

[71] E. H. Lieb and S. Oxford, *Int. J. Quantum Chem.*, 1981, **19**, 427.

[72] Y. Zhang and W. Yang, *Phys. Rev. Lett.*, 1998, **80**, 890.

[73] B. Hammer, L. B. Hansen, and J. K. Norskov, *Phys. Rev. B*, 1999, **59**, 7413.

[74] V. I. Anisimov, F. Aryasetiawan, and A. I. Lichtenstein, *J. Phys. Condens. Matter*, 1997, **9**, 767.

[75] S. Grimme, *J. Comput. Chem.*, 2006, **27**, 1787.

[76] A. Stroppa and G. Kresse, *New J. Phys.*, 2008, **10**, 063020.

[77] I. S. Balbaa, P. A. Hardy, A. Sanmartin, P. G. Coulter, and F. D. Manchester, *J. Phys. F: Metal Physics today*, 1987, **17**, 2041.

[78] *CRC Handbook of Chemistry and Physics (86th edition)*, Taylor and Francis, 2005.

[79] J. J. Mortensen, K. Kaasbjerg, S. L. Frederiksen, J. K. Nørskov, J. P. Sethna, and K. W. Jacobsen, *Phys. Rev. Lett.*, 2005, **95**, 216401.

[80] S. J. Clark, M. D. Segall, C. J. Pickard, P. J. Hasnip, M. J. Probert, K. Refson, and M. C. Payne, *Zeitschrift fur Kristallographie*, 2005, **220**, 567.

[81] Accelrys Inc., San Diego, USA, http://accelrys.com/products/materials-studio/.

[82] A. Kokalj, *Comp. Mater. Sci.*, 2003, **28**, 155.

[83] H. J. Monkhorst and J. D. Pack, *Phys. Rev. B*, 1976, **13**, 5188.

[84] R. Fletcher, *Practical methods of optimization (2nd edition)*, New York: John Wiley & Sons, 1987.

[85] P. Pulay, *Mol. Phys.*, 1969, **17**, 197.

[86] D. Vanderbilt, *Phys. Rev. Lett.*, 1987, **59**, 1456.

[87] J. F. Nye, *Physical Properties of Crystals: Their Representation by Tensoras and Matrices*, London: Oxford University Press, 1957.

[88] S. Gao, C. J. Pickard, A. Perlov, and V. Milman, *J. Phys. Condens. Matter*, 2009, **21**, 104203.

[89] Z. H. Zeng, X. F. Ma, W. C. Ding, and W. X. Li, *Sci. China Chem.*, 2010, **53**, 402.

[90] J. Tersoff and D. R. Hamann, *Phys. Rev. B*, 1985, **31**, 805.

[91] E. Furimsky, *Catal. Rev.*, 1983, **25**, 421.

[92] B. A. Sexton, *Surf. Sci.*, 1985, **163**, 99.

[93] J. L. Solomon, R. J. Madix, and J. Stöhr, *J. Chem. Phys.*, 1991, **94**, 4012.

[94] R. M. Ormerod, C. J. Baddeley, C. Hardacre, and R. M. Lambert, *Surf. Sci.*, 1996, **360**, 1.

[95] T. E. Caldwell, I. M. Abdelrehim, and D. P. Land, *J. Am. Chem. Soc.*, 1996, **118**, 907.

[96] T. E. Caldwell and D. P. Land, *Polyhedron*, 1997, **16**, 3197.

[97] T. E. Caldwell and D. P. Land, *J. Phys. Chem. B*, 1999, **103**, 7869.

[98] D. N. Futaba and S. Chiang, *J. Vac. Sci. Technol. A*, 1997, **15**, 1295.

[99] A. Loui and S. Chiang, *Appl. Surf. Sci.*, 2004, **237**, 559.

[100] M. J. Knight, F. Allegretti, E. A. Kröger, M. Polcik, C. L. A. Lamont, and D. P. Woodruff, *Surf. Sci.*, 2008, **602**, 2524.

[101] A. Loui *An Experimental and Theoretical Study of Furan Decomposition on Pd(111) Using Scanning Tunneling Microscopy and Density Functional Theory* PhD thesis, University of California at Davis, 2005.

[102] M. J. Knight, F. Allegretti, E. A. Kröger, M. Polcik, C. L. A. Lamont, and D. P. Woodruff, *Surf. Sci.*, 2008, **602**, 2743.

[103] M. R. Churchill, L. A. Buttrey, J. B. Keister, J. W. Ziller, T. S. Janik, and W. S. Striejewske, *Organometallics*, 1990, **9**, 766.

[104] H. Ohtani, M. A. V. Hove, and G. A. Somorjai, *Surf. Sci.*, 1987, **187**, 372.

[105] B. Bak, D. Christensen, W. B. Dixon, L. Hansen-Nygaard, J. R. Andersen, and M. Schottlnder, *J. Mol. Spect.*, 1962, **9**, 124.

[106] P. B. Liescheski and D. W. H. Rankin, *J. Mol. Structure*, 1989, **196**, 1.

[107] J. S. Kwiatkowski, J. Leszczynski, and I. Teca, *J. Mol. Structure*, 1997, **436-437**, 451.

[108] J. L. Gland, B. A. Sexton, and G. B. Fisher, *Surf. Sci.*, 1980, **95**, 587.

[109] H. A. Yoon, N. Materer, M. Salmeron, M. A. van Hove, and G. A. Somorjai, *Surf. Sci.*, 1997, **376**, 254.

[110] P. Sony, P. Puschnig, D. Nabok, and C. Ambrosch-Draxl, *Phys. Rev. Lett.*, 2007, **99**, 176401.

[111] N. Atodiresei, V. Caciuc, P. Lazic, and S. Blügel, *Phys. Rev. Lett.*, 2009, **102**, 136809.

[112] H. Orita and N. Itoh, *Surf. Sci.*, 2004, **550**, 177.

[113] F. Zaera, E. B. Kollin, and J. L. Gland, *Langmuir*, 1987, **3**, 555.

[114] A. Imanishi, S. Yagi, T. Yokoyama, Y. Kitajima, and T. Ohta, *J. Elect. Spectrosc.*, 1996, **80**, 151.

[115] S. Terada, T. Yokoyama, M. Sakano, A. Imanishi, Y. Kitajima, M. Kiguchi, Y. Okamoto, and T. Ohta, *Surf. sci.*, 1998, **414**, 107.

[116] A. Imanishi, T. Yokoyama, Y. Kitajima, and T. Ohta, *Bull. Chem. Soc. Japan*, 1998, **71**, 831.

[117] D. I. Sayago, M. Polcik, G. Nisbet, C. L. A. Lamont, and D. P. Woodruff, *Surf. Sci.*, 2005, **590**, 76.

[118] D. P. Woodruff - private communication.

[119] J. E. Demuth and D. E. Eastman, *Phys. Rev. Lett.*, 1974, **32**, 1123.

[120] G. D. Waddill and L. L. Kesmodel, *Phys. Rev. B*, 1985, **31**, 4940.

[121] N. Lorente, *Appl. Phys. A- Mater. Sci. Process*, 2004, **78**, 799.

[122] I. E. Wachs and R. J. Madix, *J. Catal.*, 1978, **53**, 208.

[123] M. Bowker and R. J. Madix, *Surf. Sci.*, 1980, **95**, 190.

[124] A. F. Carley, P. R. Davies, and G. G. Mariotti, *S. Read. Surf. Sci.*, 1996, **364**, L525.

[125] L. Zhou, S. Günther, and R. Imbihl, *J. Catal.*, 2005, **230**, 166.

[126] L. Zhou, S. Günther, and R. Imbihl, *J. Catal.*, 2005, **232**, 295.

[127] S. Günther, L. Zhou, M. Hävecker, A. Knop-Gericke, E. Kleinenov, R. Schlögl, and R. Imbihl, *J. Chem. Phys.*, 2006, **125**, 114709.

[128] B. A. Sexton, A. E. Hughes, and N. R. Avery, *Surf. Sci.*, 1986, **155**, 366.

[129] A. F. Carley, A. W. Owens, M. K. Rajumon, M. W. Roberts, and S. D. Jackson, *Catal. Lett.*, 1996, **37**, 79.

[130] P. Singnurkar, I. Bako, H. P. Koch, E. Demirci, A. Winkler, and R. Schennach, *J. Phys. Chem. C*, 2008, **112**, 14034.

[131] F. M. Leibsle, S. M. Francis, R. Davis, N. Xiang, S. Haq, and M. Bowker, *Phys. Rev. Lett.*, 1994, **72**, 2569.

[132] F. M. Leibsle, S. M. Francis, S. Haq, and M. Bowker, *Surf. Sci.*, 1994, **318**, 46.

[133] S. Poulston, A. H. Jones, R. A. Bennett, and M. Bowker, *J. Phys. Condens. Matter*, 1996, **8**, L765.

[134] F. Leibsle, *J. Phys. Condens. Matter*, 1997, **9**, 8787.

[135] S. Poulston, A. H. Jones, R. A. Bennett, and M. Bowker, *J. Phys. Condens. Matter*, 1996, **9**, 8791.

[136] M. Bowker, *Top. Catal.*, 1996, **3**, 461.

[137] A. H. Jones, S. Poulston, R. A. Bennett, and M. Bowker, *Surf. Sci.*, 1997, **380**, 31.

[138] S. L. Silva, R. M. Lemor, and F. M. Leibsle, *Surf. Sci.*, 1999, **421**, 135.

[139] S. L. Silva, R. M. Lemor, and F. M. Leibsle, *Surf. Sci.*, 1999, **421**, 146.

[140] M. Bowker, *Chem. Soc. Rev.*, 2007, **36**, 1656.

[141] S. Sakong and A. Gross, *J. Catal.*, 2005, **231**, 420.

[142] S. Sakong and A. Gross, *J. Phys. Chem. A*, 2007, **111**, 8814.

[143] D. Mei, L. Xu, and G. Henkelman, *J. Phys. Chem. C*, 2009, **113**, 4522.

[144] K. C. Prince, E. Holub-Krappe, K. Horn, and D. P. Woodruff, *Phys. Rev. B*, 1985, **32**, 4249.

[145] E. Holub-Krappe, K. C. Prince, K. Horn, and D. P. Woodruff, *Surf. Sci.*, 1986, **173**, 176.

[146] W. Moritz and D. Wolf, *Surf. Sci.*, 1985, **163**, L655.

[147] Z. P. Hu, B. C. Pan, W. C. Fan, and A. Ignatiev, *Phys. Rev. B*, 1990, **41**, 9692.

[148] B. W. Holland and D. P. Woodruff, *Surf. Sci.*, 1973, **36**, 488.

[149] M. Bowker - private communication.

[150] D. P. Woodruff, *Curr. Opin. Solid State Mater. Sci.*, 2003, **7**, 75.

[151] R. Terborg, J. T. Hoeft, M. Polcik, R. Lindsay, O. Schaff, A. M. Bradshaw, R. Toomes, N. A. Booth, D. P. Woodruff, E. Rotenberg, and J. Denlinger, *Phys. Rev. B*, 1999, **60**, 10715.

[152] G. Ayrault and G. Ehrlich, *J. Chem. Phys.*, 1972, **57**, 1788.

[153] H. P. Bonzel and E. E. Latta, *Surf. Sci.*, 1978, **76**, 275.

[154] J. Cousty, R. Peix, and B. Perraillon, *Surf. Sci.*, 1981, **107**, 586.

[155] N. A. Booth, D. P. Woodruff, O. Schaff, T. Giessel, R. Lindsay, P. Baumgartel, and A. M. Bradshaw, *Surf. Sci.*, 1998, **397**, 258.

[156] J.-H. Kang, R. L. Toomes, M. Polcik, M. Kittel, J. T. Hoeft, V. Efstathiou, D. P. Woodruff, and A. M. Bradshaw, *J. Chem. Phys.*, 2003, **118**, 6059.

[157] F. Allegretti, M. Polcik, and D. P. Woodruff, *Surf. Sci.*, 2007, **601**, 3611.

[158] G. Jones, L. B. Jones, F. Thibault-Starzyk, E. A. Seddon, R. Raval, S. J. Jenkins, and G. Held, *Surf. Sci.*, 2006, **600**, 1924.

[159] R. B. Rankin and D. S. Sholl, *Surf. Sci.*, 2003, **548**, 301.

[160] M. Furukawa, H. Fujisawa, S. Katano, H. Ogasawara, Y. Kim, T. Komeda, A. Nilsson, and M. Kawai, *Surf. Sci.*, 2003, **532-535**, 261.

[161] T. Yamada, K. Shirasaka, A. Takano, and M. Kawai, *Surf. Sci.*, 2004, **561**, 233.

[162] D. J. Frankel, Q. Chen, and N. V. J. Richardson, *Chem. Phys.*, 2006, **124**, 204704.

[163] T. Giessel, O. Schaff, R. Lindsay, R. Terborg, P. Baumgärtel, J. T. Hoeft, M. Polcik, A. M. Bradshaw, A. Koebbel, D. R. Lloyd, and D. P. Woodruff, *J. Chem. Phys.*, 1999, **110**, 9666.

[164] R. Terborg, M. Polcik, J. T. Hoeft, M. Kittel, M. Pascal, J. H. Kang, C. Lamont, A. M. Bradshaw, and D. P. Woodruff, *Surf. Sci.*, 2000, **457**, 1.

[165] M. A. V. Hove, R. J. Koestener, P. C. Stair, J. P. Bibérian, L. L. Kesmodel, I. Bartos, and G. A. Somorjai, *Surf. Sci.*, 1981, **103**, 218.

[166] L. Lang, K. Müller, K. Heinz, M. A. V. Hove, R. J. Koestner, and G. A. Somorjai, *Surf. Sci.*, 1983, **127**, 347.

[167] A. Schmidt, W. Meier, L. Hammer, and K. Heinz, *J. Phys. Condens. Matter*, 2002, **14**, 12353.

[168] L. Hammer, W. Meier, A. Klein, P. Landfried, A. Schmidt, and K. Heinz, *Phys. Rev. Lett.*, 2003, **91**, 156101.

[169] V. Fiorentini, M. Methfessel, and M. Scheffler, *Phys. Rev. Lett.*, 1993, **71**, 1051.

[170] J. G. Chen, S. Lehwald, G. Kisters, E. Preuss, and H. Ibach, *J. Electron Spectrosc. Relat. Phenom.*, 1990, **54-55**, 405.

[171] A. Filippetti and V. Fiorentini, *Surf. Sci.*, 1997, **377**, 112.

[172] O. H. Nielsen and R. M. Martin, *Phys. Rev. Lett.*, 1983, **50**, 697.

[173] D. Spišák and J. Hafner, *Surf. Sci.*, 2003, **546**, 27.

[174] D. Lerch, S. Müller, L. Hammer, and K. Heinz, *Phys. Rev B*, 2006, **74**, 075426.

[175] R. J. Needs and M. J. Godfrey, *Phys. Rev. B*, 1990, **42**, 10933.

[176] M. Mansfield and R. J. Needs, *Phys. Rev. B*, 1991, **43**, 8829.

[177] M. Blanco-Rey and S. J. Jenkins, *J. Phys. Condens. Matter*, 2010, **22**, 135007.

[178] D. Lerch, O. Wieckhorst, L. Hammer, K. Heinz, and S. Müller, *Phys. Rev. B*, 2008, **78**, 121405.

[179] F. R. Vukajlovic, Z. S. Popovic, A. Baldereschi, and Ž. V. Šljivancanin, *Phys. Rev. B*, 2010, **81**, 085425.

[180] H. C. Poon, D. K. Saldin, D. Lerch, W. Meier, A. Schmidt, A. Klein, S. Müller, L. Hammer, and K. Heinz, *Phys. Rev. B*, 2006, **74**, 125413.

[181] A. Klein PhD thesis, University Erlangen-Nürnberg, 2007, as reported in reference 169.

[182] L. H. Dubois and R. G. Nuzzo, *Annu. Rev. Phys. Chem.*, 1992, **43**, 437.

[183] F. Schreiber, *Prog. Surf. Sci.*, 2000, **65**, 151.

[184] A. Ulman, *Chem. Rev.*, 1996, **96**, 1533.

[185] C. Vericat, M. E. Vela, and R. C. Salvarezza, *Phys. Chem. Chem. Phys.*, 2005, **7**, 3258.

[186] T. Otsubo, Y. Aso, and K. Takimiya, *J. Mater. Chem.*, 2002, **12**, 2565.

[187] L. M. Demers, D. S. Ginger, S.-J. Park, Z. Li, S.-W. Chung, and C. A. Mirkin, *Science*, 2002, **296**, 1836.

[188] R. A. van Delden, M. K. J. ter Wiel, M. M. Pollard, J. Vicario, N. Koumura, and B. L. Feringa, *Nature*, 2005, **437**, 1337.

[189] A. Imanishi, S. Takenaka, T. Yokoyama, Y. Kitajima, and T. Ohta, *J. Phys. IV France*, 1997, **7**, C2–701.

[190] T. Tsuduki, A. Imanishi, K. Isawa, S. Terada, F. Matsui, M. Kiguchi, T. Yokoyama, and T. Ohta, *J. Synchratron Rad.*, 1999, **6**, 787.

[191] M. S. Kariapper, C. J. Fisher, D. P. Woodruff, B. C. C. Cowie, and R. G. Jones, *J. Phys.: Condens. Matter*, 2000, **105**, 2153.

[192] H. Kondoh, N. Saito, F. Matsui, T. Yokoyama, T. Ohta, and H. Kuroda, *J. Phys. Chem. B*, 2001, **105**, 12870.

[193] H. C. Zeng, R. A. McFarlane, and K. A. R. Mitchell, *Can. J. Phys.*, 1990, **68**, 353.

[194] E. Vlieg, I. K. Robinson, and R. McGrath, *Phys. Rev. B*, 1990, **41**, 7896.

[195] Q. T. Jiang, P. Fenter, and T. Gustafsson, *Phys. Rev. B*, 1990, **42**, 9291.

[196] A. E. S. von Wittenau, Z. Hussain, L. Q. Wang, Z. H. Huang, Z. G. Li, and D. A. Shirley, *Phys. Rev. B*, 1992, **45**, 13614.

[197] D. C. Sheppard, M. Walker, C. F. McConville, D. P. Woodruff, T. C. Q. Noakes, and P. Bailey, *Surf. Sci.*, 2010, **604**, 1727.

[198] S. M. Driver and D. P. Woodruff, *Surf. Sci.*, 2001, **488**, 207.

[199] D. P. Woodruff, *J. Phys.: Condens. Matter*, 1994, **6**, 6067.

[200] J. L. Domange and J. Oudar, *Surf. Sci.*, 1968, **11**, 124.

[201] D. P. Woodruff, *Phys. Chem. Chem. Phys.*, 2008, **10**, 7211.

[202] S. M. Driver and D. P. Woodruff, *Surf. Sci.*, 2000, **457**, 11.

[203] G. S. Parkinson, M. A. Muñoz-Márquez, P. D. Quinn, M. J. Gladys, D. P. Woodruff, P. Bailey, and T. C. Q. Noakes, *Surf. Sci.*, 2005, **598**, 209.

[204] H. Rieley, G. K. Kendall, A. Chan, R. G. Jones, J. Lüdecke, D. P. Woodruff, and B. C. C. Cowie, *Surf. Sci.*, 1997, **392**, 143.

[205] S. M. Driver and D. P. Woodruff, *Langmuir*, 2000, **16**, 6693.

[206] A. Ferral, E. M. Patrito, and P. Parede-Olivera, *J. Phys. Chem. B*, 2006, **110**, 17050.

[207] N. P. Prince, D. L. Seymour, D. P. Woodruff, R. G. Jones, and W. Walter, *Surf. Sci.*, 1989, **215**, 566.

[208] N. P. Prince, M. J. Ashwin, D. P. Woodruff, N. K. Singh, W. Walter, and R. G. Jones, *Faraday Discuss. Chem. Soc.*, 1990, **89**, 301.

[209] G. J. Jackson, D. P. Woodruff, R. G. Jones, N. K. Singh, A. S. Y. Chan, B. C. C. Cowie, and V. Formoso, *Phys. Rev. Lett.*, 2000, **84**, 119.

[210] R. L. Toomes, M. Polcik, M. Kittel, J. T. Hoeft, D. I. Sayago, M. Pascal, C. L. A. Lamont, J. Robinson, and D. P. Woodruff, *Surf. Sci.*, 2002, **513**, 437.

[211] H. Grönbeck, *J. Phys. Chem. C*, 2010, **114**, 15973.

[212] P. Maksymovych, D. C. Sorescu, and J. T. Yates, *Phys. ReV. Lett.*, 2006, **97**, 146103.

[213] D. C. Sheppard - private communication.